"All truths are easy to understand once they are discovered; the point is to discover them"

–Galileo Galilei

University of Alberta

Flatness-Based End-Control of a Gas Exchange Solenoid Actuator for IC Engines

by

Soon K. Chung

A thesis submitted to the Faculty of Graduate Studies and Research in partial fulfillment of the requirements for the degree of Master of Science.

Department of Mechanical Engineering

Edmonton, Alberta

Fall 2005

Library and Archives Canada

Published Heritage Branch

395 Wellington Street
Ottawa ON K1A 0N4
Canada

Bibliothèque et Archives Canada

Direction du Patrimoine de l'édition

395, rue Wellington
Ottawa ON K1A 0N4
Canada

0-494-09145-2

Your file *Votre référence*
ISBN:
Our file *Notre reference*
ISBN:

NOTICE:
The author has granted a non-exclusive license allowing Library and Archives Canada to reproduce, publish, archive, preserve, conserve, communicate to the public by telecommunication or on the Internet, loan, distribute and sell theses worldwide, for commercial or non-commercial purposes, in microform, paper, electronic and/or any other formats.

The author retains copyright ownership and moral rights in this thesis. Neither the thesis nor substantial extracts from it may be printed or otherwise reproduced without the author's permission.

AVIS:
L'auteur a accordé une licence non exclusive permettant à la Bibliothèque et Archives Canada de reproduire, publier, archiver, sauvegarder, conserver, transmettre au public par télécommunication ou par l'Internet, prêter, distribuer et vendre des thèses partout dans le monde, à des fins commerciales ou autres, sur support microforme, papier, électronique et/ou autres formats.

L'auteur conserve la propriété du droit d'auteur et des droits moraux qui protège cette thèse. Ni la thèse ni des extraits substantiels de celle-ci ne doivent être imprimés ou autrement reproduits sans son autorisation.

In compliance with the Canadian Privacy Act some supporting forms may have been removed from this thesis.

While these forms may be included in the document page count, their removal does not represent any loss of content from the thesis.

Conformément à la loi canadienne sur la protection de la vie privée, quelques formulaires secondaires ont été enlevés de cette thèse.

Bien que ces formulaires aient inclus dans la pagination, il n'y aura aucun contenu manquant.

Canada

Abstract

The control of solenoid valve actuators used for gas exchange in internal combustion engines is considered in this dissertation. Although solenoid valves offer performance benefits over traditional camshaft-based valve systems, an important requirement during operation is to maintain low impact velocity of the armature and valve. The actuator's flat property is exploited in the control design that meets a number of end motion specifications. A flat output, which represents the design parameter, is parameterized with B-spline basis functions using nonlinear programming. A number of motion requirements, nonlinear magnetic effects and voltage constraints are incorporated into the nonlinear feasibility problem to ensure an appropriate position-velocity-acceleration profile results. The resulting flat output provides an open-loop control which is augmented with feedback so that linear stable tracking error dynamics is achieved. The proposed control scheme is demonstrated in simulation and on an experimental tesbed.

ACKNOWLEDGEMENTS

This is an opportunity to express my gratitude to all those individuals or companies whose support and guidance have made this work possible.

First and for most, I owe special thanks to my supervisor, Dr. Bob Koch, for his expertise and assistance throughout the course of this work. It has been a pleasure working with someone who has not only been helpful but exudes patience, confidence and trust in me for completing this work. I am indebted for his financial support that has made this undertaking of a Master's of Science degree possible.

I would like to express my gratitude to Dr. Alan Lynch for his guidance, insights and contribution of time.

Many thanks to all the Mechanical Engineering machinist/technicians, Bernie Faulkner, Ian Buttar, Dave Pape, Rick Bubenko, Albert Yeun and Terry Nord for their expert skills and advice.

Thanks to my colleagues in Room 2-14, Room 4-28 and Room 6-28 for making the environment and experience enjoyable.

The donation of solenoid actuators and testbed equipment by Daimler-Chrysler AG is gratefully acknowledged. Also, I would like to thank Auto21 for their financial support.

And finally, a very special thank you to my family and Caroline Chan for their unselfish support in me to pursue this degree.

TABLE OF CONTENTS

1 Introduction **1**

1.1 Motivation for the Research 2

1.2 Problem Statement 6

1.3 Thesis Organization 6

1.4 Thesis Contributions 7

2 Review On Electromagnetic Actuator Control **9**

2.1 Variable Valve Timing 10

2.2 Working Principle of an Electromagnetic Valve Actuator 12

2.3 Overview of Linear Electromagnetic Actuator Control 16

2.4 Summary 26

3 Modeling and Nonlinear Control **28**

3.1 Mechanical System Model 28

3.2 Electromagnetic Force Model 30

3.3 Electrical Coil Dynamics Model 34

3.4 EMV System Nonlinear Model 36

3.5 Flatness-Based Control 36

3.5.1 The Lambert W Function 40

3.5.2 Feedback End-Control 41

3.6 System Identification of Mass-Spring Properties 43

3.7 Open-Loop Trajectory Design 46
3.7.1 Nonlinear Constrained Problem 46
3.7.2 Parametrization of the Flat Output Trajectory 49
3.8 Summary 55

4 Experimental Setup **56**
4.1 EMV Actuator 56
4.2 Computer Hardware and Software 59
4.2.1 dSPACE DS1103 Controller Board 59
4.3 Testbed Setup and Equipment 61
4.3.1 Power Supplies 62
4.3.2 Circuit Protection 64
4.3.3 Current and Voltage Sensing 65
4.3.4 Armature Displacement Sensor 68
4.3.5 Power Electronics 69
4.4 Summary 71

5 Results and Discussion **73**
5.1 Simulink Model of an EMV Actuator 73
5.2 Simulation Results 76
5.2.1 Simulation Case 1 76
5.2.2 Simulation - Sensitivity to Initial Position and Velocity Conditions 81
5.3 Experimental Implementation 86
5.3.1 Flatness-Based Voltage End-Control 86
5.3.2 Proportional-Integral Current End-Control 88
5.4 Experimental Results 90
5.5 Summary 98

6 Conclusions and Further Research **99**

6.1 Further Research 101

Bibliography **102**

A Filter Algorithms for Real-Time Applications **113**

A.1 Constant Gain Extended Kalman Filter 113

A.2 Exponentially Weighted Moving Average Filter 116

B Experimental Equipment Schematics **118**

B.1 Overcurrent Protection Circuit 119

B.2 Opto-Isolator 120

B.3 Power Electronics Current-Voltage Sensing 121

B.4 LEM LA55-P Current Transducer Specifications 122

C Software Structure **123**

C.1 Program Development Structure Objectives 123

C.2 Program Structure 124

C.3 Modules Description 125

C.3.1 Tasks 125

C.3.2 RPM Generator 125

C.3.3 Start Oscillation 125

C.3.4 Control 125

C.3.5 Flatness-Based Voltage End-Control 127

C.3.6 Open-loop Trajectory Control 127

C.3.7 Filter 127

C.3.8 Data Exchange 127

C.3.9 Task Control 128

C.3.10 Hardware Interface 128

C.3.11 User Interface 128
C.3.12 Sequence Control 128
C.3.13 Data Interface 128

List of Tables

1.1 Benefits of variable valve timing 4

2.1 Valve timing events [Kreuter et al., 1992] 11

2.2 Control strategies for gas exchange solenoid actuators 26

4.1 Relevant experimental equipment specifications 72

List of Figures

2.1 Valve timing events for a four-stroke engine cycle 10

2.2 Schematic of a Telefunken Microelectronic (TEMIC) linear solenoid actuator 13

2.3 Typical operation of a two spring solenoid actuator valve 15

3.1 Schematic of a two spring solenoid actuator valve 29

3.2 Experimental force versus position for varying current 32

3.3 Comparison of (3.6) with experimental force 33

3.4 Equivalent circuit diagram of the electrical coil subsystem 35

3.5 Correspondence between flat output space and state space 38

3.6 Two real branches of the Lambert W function 41

3.7 Scheme of the flatness-based end-control loop for the actuator 42

3.8 Plant model parametrization 45

3.9 Error between measured and fitted armature positions 45

3.10 Quartic B-splines over $[t_0,\ t_f]$ 51

3.11 Reference armature position (y_d) 52

3.12 Reference armature velocity $(\dot{y}_d)$ 52

3.13 Reference armature acceleration $(\ddot{y}_d)$ 53

3.14 Reference armature jerk $(y_d^{(3)})$ 53

3.15 Reference coil current (i_c) 54

3.16 Reference coil voltage (U_c) 54

4.1 Experimental testbed setup 57
4.2 TEMIC actuator and valve sectional view [Chladny, 2003] 58
4.3 ControlDesk data collection template 60
4.4 ControlDesk parameter instruments template 60
4.5 dSPACE DS1103 controller board and PowerPC 604e microprocessor 61
4.6 Testbed setup 62
4.7 Sorenson DCS60-18E and Hewlett Packard 6236B power supplies . . 63
4.8 Overcurrent protection circuit 64
4.9 16 channel opto-isolator 65
4.10 LEM LA55-P hall-effect current sensor 66
4.11 Schematic of hall-effect current sensor 67
4.12 Eddy current type lift sensor 68
4.13 Power electronics 70
4.14 Power electronics output modes 70
4.15 Experimental testbed setup schematic 71

5.1 Scheme of flatness-based voltage end-control with estimation of state variables 74
5.2 Simulink power electronics model [Ryan Chladny - personal communication] 75
5.3 Actual and simulated power electronics output voltages 76
5.4 Desired and simulated armature position 78
5.5 Desired and simulated armature velocity 78
5.6 Desired and simulated armature acceleration 79
5.7 Desired and simulated coil current 79
5.8 Simulated eddy currents 80
5.9 Simulated coil voltage input 80

5.10 Desired and simulated armature position (Case 2 and 3) 83
5.11 Desired and simulated armature velocity (Case 2 and 3) 83
5.12 Desired and simulated armature acceleration (Case 2 and 3) 84
5.13 Desired and simulated coil current (Case 2 and 3) 84
5.14 Simulated eddy currents (Case 2 and 3) 85
5.15 Simulated coil voltage input (Case 2 and 3) 85
5.16 Control algorithm for flatness-based voltage end-control 86
5.17 Approach control and flatness-based end-control parameter inputs in ControlDesk 87
5.18 Scheme of proportion-integral current end-control for real-time implementation 89
5.19 Approach control and proportional-integral end-control parameter inputs in ControlDesk 90
5.20 Desired, simulated and experimental results for armature position . . 92
5.21 Desired, simulated and experimental results for armature velocity . . 93
5.22 Desired, simulated and experimental results for armature acceleration 93
5.23 Simulated and experimental results for current 94
5.24 Simulated and experimental results for coil voltage 94
5.25 50 cycles of experimental armature position data for flatness-based voltage end-control 95
5.26 Distribution of armature impact velocity for 50 cycles using flatness-based voltage end-control 96
5.27 Distribution of armature impact velocity for 50 cycles using proportional-integral current end-control 97

A.1 Block diagram of Kalman filter algorithm 115

B.1 Overcurrent protection circuit schematics 119

B.2 Opto-isolator circuit schematics 120
B.3 Onboard power electronics current-voltage sensing 121

C.1 Multi-platform program structure (dotted line → debugging file I/O platform and solid line → real-time platform) 124
C.2 Control state machine 126

NOMENCLATURE

Acronyms

BDC	Bottom Dead Center
EMV	Electromagnetic Valve
EMF	Electro-magnetomotive Force
EGR	Exhaust Gas Recirculation
EVC	Exhaust Valve Closing
EVO	Exhaust Valve Opening
FE	Finite Element
FEA	Finite Element Analysis
HCCI	Homogeneous Charge Compression Ignition
IC	Internal Combustion
ILC	Iterative Learning Controller
ISA	Industry Standard Architecture
IVC	Intake Valve Closing

IVO	Intake Valve Opening
LED	Light Emitting Diode
LQ	Linear Quadratic
LQR	Linear Quadratic Regulator
PC	Personal Computer
PCI	Peripheral Component Interconnect
PWM	Pulse Width Modulated
QP	Quadratic Program
RTI	Real-Time Implementation
SQP	Sequential Quadratic Programming
TDC	Top Dead Center
TEMIC	Telefunken Microelectronic
TTL	Transistor-to-Transistor Logic
VVA	Variable Valve Actuation
VVT	Variable Valve Timing

Nomenclature

β, γ ..... Extremum Seeking Nonlinear Controller Tuning Parameters [mm]

μ_0 ..... Permeability Constant $4\pi \cdot 10^{-7}$ [H/m]

$\rho(x, i_c)$ ..... Force Function Parameter [Nm/HA^2]

λ ..... Flux Linkage [Wb-Turns]

λ_s ..... Saturated Flux Linkage [Wb-Turns]

a, c ..... Exponential Trajectory Function Coefficients [mm]

b ..... Exponential Trajectory Function Coefficient [1/s]

A ..... Core Area [m^2]

B ..... Damping Coefficient [Ns/m]

C_1 ..... Constant Coefficient [mm/A]

C_2 ..... Constant Coefficient [mm]

C_3 ..... Constant Coefficient [1/A]

$F(x, i_c)$ ..... Electromagnetic Force [N]

g ..... Gap distance [mm]

H_0 ..... Constant [1/m]

i_c ..... Coil Current [A]

i_e ..... Eddy Current [A]

k_0 ..... Linear Error Dynamics Controller Gain [$1/s^3$]

k_1 ..... Linear Error Dynamics Controller Gain [$1/s^2$]

k_2 ..... Linear Error Dynamics Controller Gain [1/s]

K_1 ..... Extremum Seeking Nonlinear Controller Gain [Vs/1000]

K_2 ..... Extremum Seeking Nonlinear Controller Gain [V·mm]

K_s ..... Armature-Valve Spring Constant [N/mm]

L_0 ..... Coil Inductance Constant [H]

L_e ..... Parasitic Inductance [H]

m ..... Moving Mass [kg]

N ..... Number of Coil Turns

R_c ..... Coil Resistance [Ω]

R_e ..... Parasitic Resistance [Ω]

S_{des} ..... Desired Sound Intensity [db]

$S_{meas}[k]$ ..... k^{th} Iteration Measured Sound Intensity [db]

t_0 ..... Initial End-Control Time [s]

t_f ..... Final End-Control Time [s]

T_c ..... Coil Temperature [$^\circ C$]

U_c ..... Coil Voltage [V]

$U_{c,fb}$ ..... Desired Control Voltage Input [V]

$W_c(x, i_c)$ ..... Co-energy Function [J]

x ..... Actual Position [mm]

$\dot{x}$ ..... Actual Velocity [m/s]

$\ddot{x}$ ..... Actual Acceleration [m/s^2]

y ..... Flat Output [mm]

y_d ..... Desired Position [mm]

$\dot{y}_d$ ..... Desired Velocity [m/s]

$\dot{y}_d$ ..... Desired Acceleration [m/s^2]

$y^{(3)}$ ..... Desired Jerk [m/s^3]

y_s ..... Closer Coil Position [m]

CHAPTER 1

INTRODUCTION

Exhaust and intake valve timing in an automobile engine can affect engine efficiency and exhaust emissions. While many manufacturers search for novel methods to reduce pollution and improve fuel consumption in internal combustion (IC) engines; one of the most currently touted methods is variable valve timing (VVT) [Haskara et al., 2004]. That is, the ability to alter the closing and opening of exhaust/intake valves accordingly to different engine load conditions. At the present, no manufacturer has been able to produce a fully flexible valvetrain that is sufficiently robust and reliable for commercial use. VVT systems that are available in current production vehicles provide limited valve actuation flexibility which relies on the camshaft to switch or phase the cam lobe [Schechter and Levin, 1996]. Those that can offer continuous control over valve events are being tested in laboratory settings and have shown significant improvements in engine performance to warrant further research. Some of these experimental systems, for example, are driven by electromagnets, hydraulics, pneumatics and mechanical components. The development of VVT systems is beyond its infancy and certainly their applications are not restricted to spark ignition engines. Other promising engine optimization strategies such as homogeneous charge compression ignition (HCCI) and flexible exhaust gas recirculation (EGR) schemes can benefit from the facilitation of VVT.

A potential valve timing technology that could conceivably replace camshaft driven exhaust and intake valves is through the use of electronically controlled solenoid actuators. These simple and cost-effective actuators are suitably designed to withstand rugged environments while generating high forces over a short stroke. However, further justification for mass production requires balancing trade-offs between energy consumption, reliability, complexity, efficiency and other related electronic component costs. In spite of rapid advancements in power-electronics, sensors/controls and microprocessors to alleviate some of these trade-offs, a challenging problem that still requires resolution is the control of low impact velocity for electromagnetic valve (EMV) actuators. This conundrum is largely due to the actuator's nonlinear magnetic behavior, and its sensitivity to disturbances and parameter uncertainties. Unless robust control methods for maintaining low impact velocities are developed, the commercial success of EMV systems in production vehicles seems unlikely in the foreseeable future [Tai and Tsao, 2003].

This chapter briefly describes the motivation for conducting EMV actuator control research, the problem statement, the organization of this dissertation, and the contributions made in this work.

1.1 Motivation for the Research

Conventional internal combustion engines usually do not operate at maximum efficiency. The engine load is controlled by a throttle, and generally, these engines have fixed valve events that are optimized during the engine development stage to meet certain driving applications. When designing camshaft lobe profiles, the procedure requires a compromise between high torque performance and maximum fuel efficiency. VVT, on the other hand, offers greater flexibility in that engine operating conditions can be tailored more precisely to maximize output and drivability [Ma, 1988]. The

concept of continuous VVT, as mentioned previously, is feasible through EMV actuation. Even though an EMV valvetrain inconjunction with associated electronic control units may increase engine parasitic load by one percent over a conventional cam valvetrain [Chladny et al., 2005], the improvements offered in engine performance outweighs the slight increase in power consumption. Table 1.1 provides a list of desirable engine improvements that are realizable by a camless valvetrain.

Table 1.1: Benefits of variable valve timing

	Desired Engine Attributes	Timing Variations	Description	Benefits
Intake Valve	Reduce throttling loss (A)	Late or Early closing	Volume of air in the cylinder at the beginning of compression is reduced thereby minimizing pumping losses.	Fuel consumption saving: 15-20%.[1, 2]
	Faster burn rate (B)	Late Opening	Increase inlet air velocity for low engine speed.	Better mixing and leaner air/fuel ratio. Improved fuel efficiency by 5%.[3] Reduced CO emission.
	Increased (C) torque	Late Closing	Maximize inertia ram-charging of intake gas.	Increase engine torque at high speed.[1]
	Variable compression ratio(D)	Late or Early Closing	Reduce in-cylinder air compression.	Prevent Knock. Improve cycle efficiency.[2]
Exhaust Valve	Optimized expansion ratio (E)	Late Opening	Optimize exhaust timing at low speeds for cylinder blow-down.	Increase torque. Improve fuel efficiency.[2]
	Internal exhaust gas recirculation(F)	Late or Early closing	Varying the timing of closure controls the amount of residual gas in the cylinder	90% NO_x reduction with 29% residual fraction.[3]
Intake and Exhaust Valves	Improved idle stability	Variable intake opening Variable exhaust closing	Idle stability is adversely affected by residual gas in the cylinder.	Minimal residual gas contributes to better idle stability.
	Variable engine displacement		Deactivating some of the engine cylinders forces the remaining cylinders to operate at a higher load to maintain a given output. This leads to improvements in fuel economy and hydrocarbon emissions.	Improved fuel efficiency: 25% low speed and 40% at idle.[3] Reduction in emissions: 40% in HC and 47% in CO at idle.[2]

continued on next page

Table 1.1: *continued*

	Desired Engine Attributes	Timing Variations	Description	Benefits
Intake and Exhaust Valves	Reduce cranking torque		Cranking the engine with some deactivated cylinders will substantially reduce power requirements for an electric starter	Possible combination of a starter and an alternator into one reversible electrical machine.
	Selective valve deactivation per cylinder		Operation with two valve can favor a tumble-like motion while one-valve operation favors a swirl. When a misfire occurs, exhaust valve opening can be prevented to retain unburned mixture and subsequently intake valve opening is prevented and the mixture is ignited in the next cycle then normal operation resumes.	Variable air-motion pattern. Misfire damage control (prevents premature catalyst burnout).

[1] [Chladny et al., 2005]
[2] [Schechter and Levin, 1996]
[3] [Dresner and Barkan, 1989]

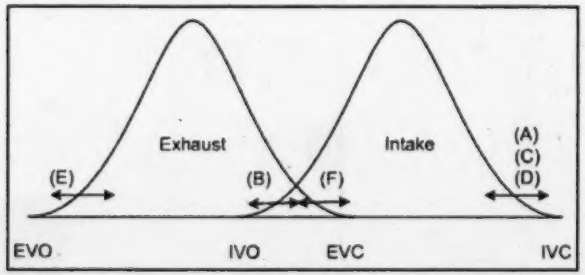

1.2 Problem Statement

The primary objective in this research is to develop an end-control scheme for an EMV actuator that would maintain low armature impact velocities of less than 0.1 m/s with a supply voltage of 42 V. In addition to obtaining acceptable acoustic noise levels, transitional armature travel times from open/closed to closed/open should be approximately 4 ms in order to meet maximum engine speeds of 5000 - 6000 RPM. This work will demonstrate the performance of the end-control scheme using simulation and on an experimental testbed. Experimental results obtained are compared to a standard control scheme.

1.3 Thesis Organization

The organization of this dissertation is outlined as follows. Chapter 2 provides a brief overview of VVT concepts and explains the working principle of an EMV actuator designed for engine use. Various modeling and control techniques developed by researchers are presented here with a common goal of achieving soft armature or valve landing. The understandings gained from their work are applied towards this dissertation in the development of a nonlinear model that predicts accurate dynamic performance.

Chapter 3 details mathematical representations for the actuator that takes nonlinear physical phenomenons such as eddy current effects and magnetic saturation into account. A flatness-based voltage end-control scheme is derived to track a reference trajectory that ensures low impact velocity. This trajectory is parameterized by B-spline basis functions using nonlinear programming [Löewis and Rudolph, 2003] while subjected to a number of constraints.

A brief discussion on the EMV experimental testbed setup is presented in Chapter 4. In Chapter 5, a lumped parameter model is used to evaluate the performance of

the controller in simulation. Experimental test results for flatness-based end-control are discussed and compared to results obtained from a standard control algorithm.

Finally in Chapter 6, the results from this work are summarized and directions for future research are discussed.

1.4 Thesis Contributions

The contributions of this thesis are summarized as follows:

- A nonlinear model of the EMV actuator has been developed to improve simulation accuracy. The electrical and mechanical model dynamics address complications introduced by eddy current effects and magnetic saturation. System identification and least-squares curve fitting methods are used to parameterize actuator model parameters with static experimental force and finite element analysis (FEA) flux-current-position data.

- The end-control solution presented here uses flatness-based methodologies to achieve low impact armature velocity of less than 0.1 m/s with a supply voltage of 42 V. It is termed flatness-based voltage end-control and it is designed to track the armature to a reference trajectory for the final portion of motion. To derive the reference profile, nonlinear constrained programming is utilized to parameterize optimal B-spline basis coefficients.

- The development of the simulation model augments power electronics and filter algorithm models (Kalman and Exponential moving average) to improve dynamic performance approximations. Case scenarios for different armature position and velocity conditions to initiate the end controller are investigated in simulation.

- An experimental testbed has been assembled for control design implementation

and model verification. All real-time tasks and control algorithms are programmed in C language. Test results for flatness-based voltage end-control are obtained and analyzed.

- A standard proportional-integral current end-control is developed and implemented in real-time. The results are used as a benchmark for comparing flatness-based voltage end-control.

Chapter 2

Literature Review on the Control of Electromagnetic Actuators

Variable valve actuation (VVA) is an existing method that offers enhanced potential for improving the automotive internal combustion engine. Originally, this concept of independent valve control was patented in 1899 with the rationale of increasing engine torque over a wide range of speed and load conditions [Payne, 1899]. As legislation on fuel economy and emissions become increasingly stringent, the emphasis on torque improvements gradually shifted towards more cleaner burning and efficient engines. Many modern automobile engines operate with devices that either perform a camshaft phase shift varying only valve timing [Dresner and Barkan, 1989, Grohn and Wolf, 1989, Maekawa et al., 1989, Moriya et al., 1996] or a switch to another cam lobe [Brüstle and Schwarzental, 2001, Fukuo et al., 1997] to offer engine performance improvements at certain engine operating points. These "camshaft add-on" devices are reliable, however, their ability to provide valve timing variations are fractional when compared to a system that possess full VVA capabilities [Schechter and Levin, 1996]. Valve actuation by electromagnets can provide control flexibility over an engine valve phase, either independently or simultaneously with other valves. Having such flexibility in valve variation is advantageous in achieving substantial improvements

in emissions, maximum power and fuel economy [Heffel, 2003]. Yet, implementation of such a system towards production vehicles still remains elusive due to the control complexity, economic viability and reliability of these actuators.

2.1 Variable Valve Timing

An important determinant for influencing engine performance is to vary the timing on closing and opening of both intake and exhaust valves [Gray, 1988]. Figure 2.1 shows typical valve events for a four-stroke engine cycle.

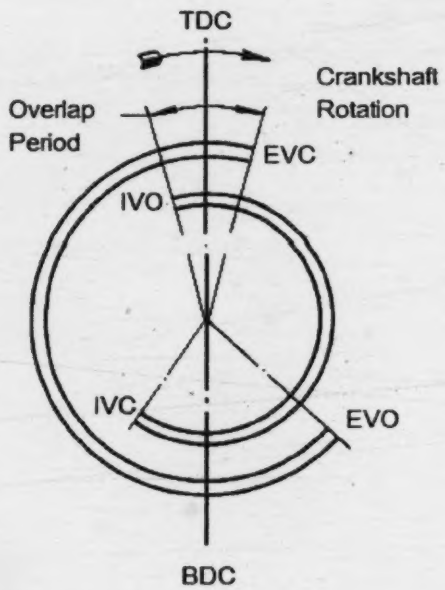

Figure 2.1: Valve timing events for a four-stroke engine cycle

where TDC is top dead center, IVO is intake valve opening, EVO is exhaust valve opening, BDC is bottom dead centre, IVC is intake valve closing and EVC is exhaust valve closing.

In a conventional engine, these valve events (i.e. EVO, EVC, IVO and IVC) are fixed in relation to crank angle. Even though this is a reliable method for supplying the engine with intake charges and exhaust gas removal, engine performance is usually a compromise between fuel economy and maximum power to suit specific driving applications [Ahmad and Theobold, 1989]. On the other hand, implementing a VVT mechanism can minimize this compromise and simultaneously satisfy different engine performance requirements. The flexibility of a VVT system offers variation in valve time, valve event variation, and even cylinder and valve deactivation [Giglio et al., 2002]. Examples of valve timings required to achieve typical engine performance objectives are shown below.

Table 2.1: Valve timing events [Kreuter et al., 1992]

Engine Performance Objectives	**Required Valve Timing Characteristics**
Greater torque at low speed Improved fuel economy	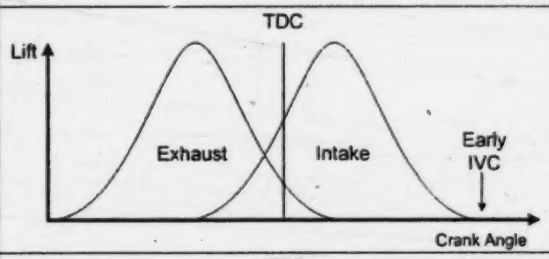
Maximum Power at high speeds	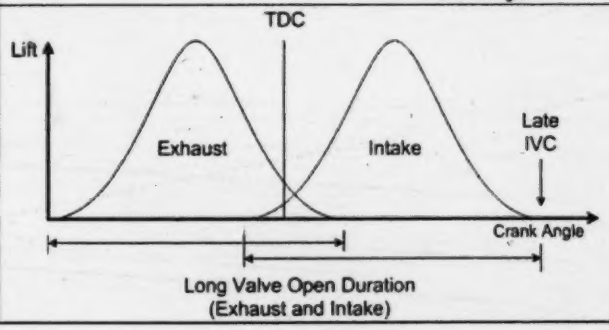

continued on next page

Table 2.1: *continued*

Engine Performance Objectives	**Required Valve Timing Characteristics**
Better idle stability	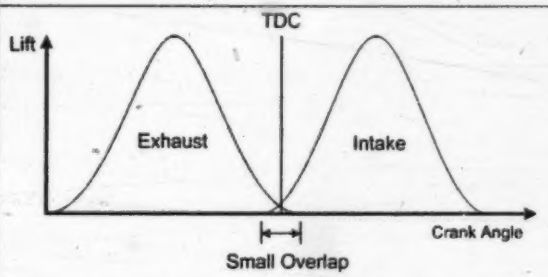

To date, the proposed systems that can provide camless continuous valve variations include electrohydraulic [Schechter and Levin, 1996] and electromagnetic actuation [Butzmann et al., 2000, Flierl and Klüting, 2000, Koch et al., 2004, Kreuter et al., 1992, Peterson and Stefanopoulou, 2004]. These actuators permit vast possibilities in valve actuation that enables implementation of other combustion types that do not obey the traditional Diesel or Otto cycles [Kontarakis et al., 2000]. In this thesis, contributions on camless system control will be made for EMV actuators.

2.2 Working Principle of an Electromagnetic Valve Actuator

One of the first designs for the EMV actuator was proposed and patented by FEV Motorentechnik [Pischinger and Kreuter, 1984]. These compact linear actuators are suitable for engine valve applications that require fast response times and high forces over a short stroke. Since they are cost effective and simple to manufacture, corporations such as Aura [Gottschalk, 1993], BMW [Flierl and Klüting, 2000], GM [Theobold et al., 1994], DaimlerChrysler AG [Gramann et al., 2000], Renault [Birch, 2000] and Siemens [Butzmann et al., 2000, Schechter and Levin, 1996] have based their proto-

type developments on the FEV Motorentechnik actuator design. Figure 2.2 shows the schematic of a Telefunken Microelectronic (TEMIC) GmBH [Gramann et al., 2000] linear actuator from DaimlerChrysler AG.

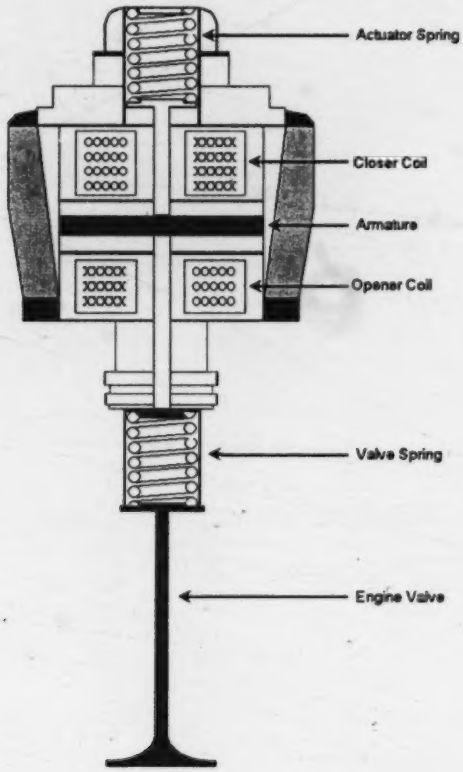

Figure 2.2: Schematic of a Telefunken Microelectronic (TEMIC) linear solenoid actuator

A typical setup for this type of EMV (as in Figure 2.2) consist of two magnets (closer and opener), two springs (an actuator and a valve spring) and a moving armature that is connected to an engine valve. Normally, most modern engines incorporate a hydraulic lash adjuster to ensure proper valve sealing under all thermal operating conditions [Wang et al., 2000]. This lash adjuster, although not shown in Figure 2.2,

would also need to be included in EMV applications. The magnets are coils wound on ferromagnetic material that are regulated by using power electronics and control signals - often pulse-width modulated (PWM) voltages. In general, these actuators operate at the natural oscillation frequency of the mass-spring system and have a neutral position in the middle. That is, when both coils are not activated, the armature is positioned in the center. Operating the armature's movement is simply triggered by applying voltage to the coils independently. Current flowing in the coil creates a magnetic force on the armature to overcome compressive spring and friction forces.

Both springs are adjusted such that they are always in compression for any armature position between the two electromagnets. Preloading these springs are ideal for achieving rapid flight time and minimizing electrical energy input [Chladny, 2003]. During normal operation, the spring forces are utilized to accelerate the moving masses while electromagnetic forces are utilized to attract and dwell the armature. Figure 2.3 illustrate a typical operational mode of the EMV actuator.

To move the valve from neutral to closed position, a routine is initialized to impart sufficient armature momentum for the closer coil magnetic forces to attract the armature. Once contact is established and quasi-static conditions are reached, a holding current is applied to the upper coil so that sufficient magnetic force is generated to overcome spring forces while holding the armature and valve in the fully closed position. When the valve is commanded to open, the upper coil current is rapidly discharged, allowing magnetic force to decay and the actuator spring to push the armature down. The lower coil is then activated to capture the approaching armature. It will hold the armature open until it is time for the valve to close again. Hence, by timing the coils' energizing/deenergizing state, variable valve operation that is independent of crank-shaft position can be achieved.

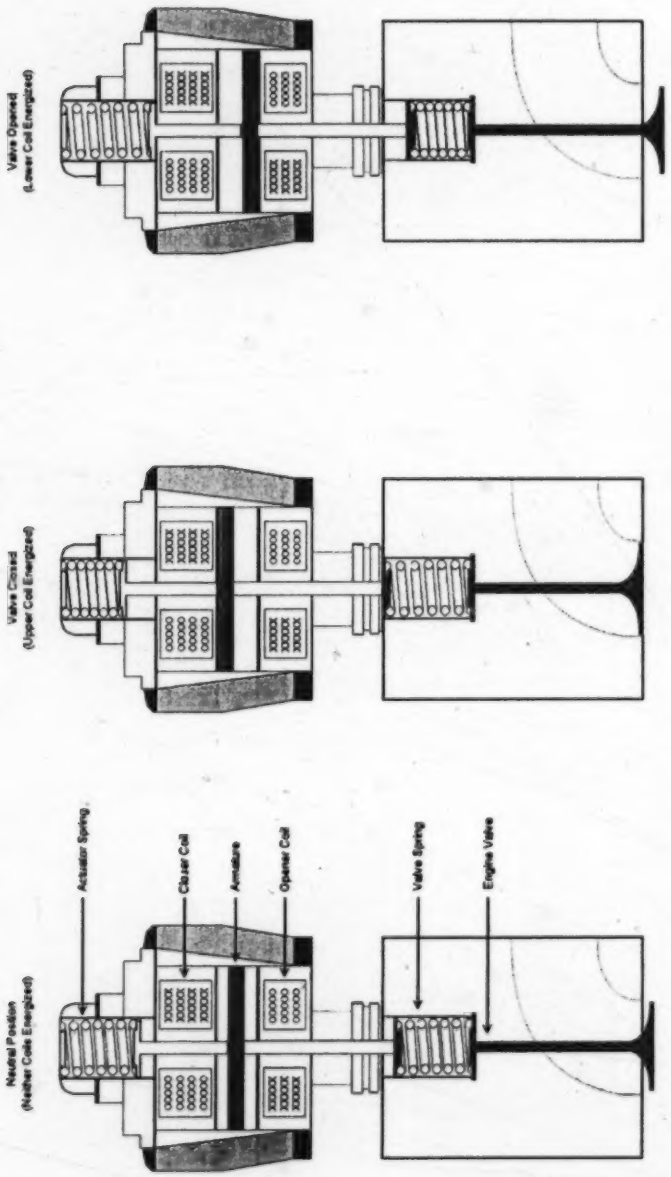

Figure 2.3: Typical operation of a two spring solenoid actuator valve

2.3 Overview of Linear Electromagnetic Actuator Control

Aside from engine variable valve technology, linear electromagnetic actuators are used extensively in other industrial applications which include anti-lock braking systems [Smith et al., 1994], door locks [Geringer et al., 1991], hydraulic/fuel injectors [Kajima and Kawamura, 1995, Venkataramu et al., 1988] and micromirror actuators [Nonaka and Baillieul, 2001]. The simple and rugged construction of these actuators makes them suitable in harsh environments yet cost-effective. However, such devices are only efficient in generating high specific force over a relatively short stroke distance [Harmer et al., 2002]. Therefore, it is essential to consider dynamic performance during the design stage of control schemes. Various approaches have been proposed for modeling linear solenoids that include lumped-parameter methods [Fulks, 1989, Kajima, 1995], models that account for eddy current and saturation effect using equivalent circuit analogy [Hughes et al., 1998, Piron et al., 1999] and simplified numerical representation [Lequesne, 1990]. For some of these applications, the demand for low impact or noise during normal operation is inconsequential. An example would be the use of a plunger-type solenoid where emphasis is placed on position control of the plunger to influence fluid flow [Lim et al., 1994, Venkataramu et al., 1988]. In low cost applications such as door locks, fast acting on/off actuators are implemented to satisfy the intended task.

Engine valve seating control differs from many industrial related actuator control requirements and continues to pose significant challenges [Sellnau and Rask, 2003, Warnecke et al., 1999]. There are two important criterions that must be met when solenoids are used to actuate gas exchange valves. First, the valve closing and opening times should take approximately 4 ms in order to meet engine speeds of 5000-6000 RPM [Peterson and Stefanopoulou, 2004]. Second, impact velocities of less than 0.1 m/s are necessary to keep engine acoustical noise to acceptable levels, and to en-

sure valve seatings and wear requirements are met [Wang et al., 2002]. The difficulty in achieving low impact velocity can be attributed to the unstable nature of the EMV at near seating positions. A mathematical analysis conducted by [Chung, 2002] for the TEMIC actuator reveals this instability region to occur when air gap distances between the armature and coil are less than 2.33 mm. Thus, stabilizing the system and reducing its sensitivity to disturbances requires closed-loop control. Despite a number of solutions based on closed-loop control schemes have been proposed, the problems of impact are not completely remedied. Existing control work often apply linear position and velocity feedback schemes to linearly approximated systems in an effort to limit armature impact velocities [Konrad, 1998]. While linear approximation techniques are sufficiently fast for use in control evaluations, such models have limitations in predicting accurate dynamic performance particularly when path effects such as eddy current, flux leakage and magnetic saturation are neglected [Chladny, 2003]. Modeling an EMV for impact problems is challenging due to the coupling of a nonlinear magnetic system with a mechanical system that involves a time-varying air gap. Finite element (FE) methods which require large computational resources are capable of accurately modeling the dynamic response. However, these FE models are impractical for studies especially when fast solution convergence is necessary [Chladny et al., 2005].

Control system development for EMV actuators has been explored by various researchers. In [Butzmann et al., 2000], a sensorless control approach is presented to achieve soft landing with velocities in the range of 0.1 m/s. This method eliminates the need for position and velocity sensors in order to avoid sensor-related inaccuracies and to save cost. Instead, a fundamental relation is derived to retrieve armature motion information from electrical coil signals. The description between electrical and mechanical properties is given as follows

$$\frac{di_c}{dt} = \frac{1}{1 + H_0\, x}\left[\frac{U_c\, x}{\mu_0 N^2 A} - \frac{i_c\, \dot{x}}{x}\right] \tag{2.1}$$

where μ_0 is the permeability constant, H_0 is a constant (1/m), A is the core area, i_c is the coil current, N is the number of coil turns, x is the air gap between armature and coil, $\dot{x}$ is the armature velocity, and U_c is the coil voltage.

When coil voltage is zero at small air gaps, Equation (2.1) simplifies to

$$\frac{di_c/dt}{i_c} = -\frac{\dot{x}}{x} \tag{2.2}$$

which defines the underlying ratio for sensorless control strategy. Therefore, as the armature approaches near landing position, coil voltage is momentarily switched off to allow observation of $\frac{di_c/dt}{i_c}$. This quotient provides information on armature velocity in relation to air gap distance for comparison to a desired constant that ensures low landing velocity. Coil currents are triggered accordingly to the comparison differential such that the predefined constant is maintained.

[Butzmann et al., 2000] were able to show their sensorless approach inconjunction with adaptive quotient control is effective under laboratory settings in spite of model invalidity at small air gap distances. Both low impact velocity and transient time conditions were met even when supply voltages were subjected to variations within 30 V and 55 V. In a test run for over 5000 cycles, an average landing velocity below 0.1 m/s is achieved with 90% of all events landing below 0.2 m/s. On a combustion engine, their system showed typical landing velocities of approximately 0.2 m/s for the inlet valve and 0.3 m/s for the exhaust valve. However, this work indicates potential problems that relates to the system's sensitivity against large disturbances [Peterson et al., 2002]. Further development of this sensorless control strategy are shown in [Gunselmann and Melbert, 2003] to yield improved robustness and energy consumption. By introducing a take-off and approach control scheme, low landing ve-

locity and electrical energy requirements are achieved for many expected disturbances of the real engine operation. The take-off control is applied during the armature's release phase while the approach control delivers the armature to state conditions that are optimal for the final landing control portion. Nevertheless, the lack of a position sensor could still potentially jeopardize robustness when unknown gas forces are applied to the valve.

Unlike the simple model in [Butzmann et al., 2000], [Wang et al., 2000] proposed a dynamic model that extends its validity for saturation effects. In their model, flux linkage, λ, and magnetic force, $F(x, i_c)$, are identified to include a linear and saturation region. Each respective regions are fitted with distinct theoretical relations that are valid for various air gap distances, x, and coil current, i_c. The relationship for flux linkage is derived as follows

$$\lambda(x,\ i_c) = \left[\frac{k_1}{k_2 + x} - k_3\right] i_c, \qquad \text{when} \quad \lambda(x,\ i_c) \leq \lambda_s \tag{2.3}$$

$$[\lambda(x,\ i_c) - \lambda_0(x)]^2 = \frac{k_4\,[i_c - i_0(x)]}{[k_5 + x]^2}, \qquad \text{when} \quad \lambda(x,\ i_c) \geq \lambda_s \tag{2.4}$$

where k_1, k_2, k_3, k_4, k_5 and λ_s are constants with $\lambda_0\ (x)$ and $i_0\ (x)$ chosen such that continuity of $\lambda\ (x, i_c)$ is preserved. While magnetic force takes the form

$$F_{linear}(x,\ i_c) = \frac{k_1 i_c^2}{2\,[k_2 + x]^2} \tag{2.5}$$

$$F_{sat}(x,\ i_c) = [F_{linear}(x,\ i_c) - F_{max}(x)]\ e^{-k_i(x)[i_c - i_s]} + F_{max}(x) \tag{2.6}$$

where i_s defines the onset current saturation that is approximated as a linear function of position, $i_s = k_6 + k_7\ x$. All model parameters are identified with steady-state and dynamic experiment measurements of electromagnetic force and valve lift positions. Maximum force, $F_{max}(x)$, is developed at excitation levels above i_s and $k_i(x)$ is a

smoothing function that ensures a continuous force curve by satisfying the following relation

$$\left.\frac{\partial F_{sat}(x,\ i_c)}{\partial i_c}\right|_{(x,i_s)} = \left.\frac{\partial F_{linear}(x,\ i_c)}{\partial i_c}\right|_{(x,i_s)} \tag{2.7}$$

A comparison between the complete state-space model and experimental results demonstrate close agreement.

Despite an improved model, [Wang et al., 2002] choose to exclude saturation in their control design. Using only linear region models, experimental results for closed-loop control are published with an average contact velocity of 0.16 m/s and transition times of 3.42 ms. These results presented are near desired operation requirements, however, high voltage levels (> 100 V) are observed during the initial stages of control execution. In fact, different control schemes are implemented at two distinct stages with the objective of improving performance and anticipating fast transients. At far from landing regions, voltage inputs are controlled primarily based on errors in current. When the armature approaches landing regions, the control switches over to a soft landing mode that enables position feedback control. Another critical element that should be noted in [Wang et al., 2002] feedback controller is the inclusion of a nonlinear observer that functions as a filter for position sensor noise and an estimator for armature velocity and circuit current.

In [Stubbs, 2000], the lumped parameter model is extended to include variations of coil resistance to temperature. Coil dynamics is defined to have the following form

$$U_c = i_c\ R_c(T_c) + \frac{d\lambda(x, i_c)}{dt} \tag{2.8}$$

where $R_c(T_c) = k_1 T_c + k_2$ while k_1 and k_2 are estimated using least-square linear regression on steady-state experimental data between coil resistance, R_c, and coil temperature, T_c. A repetitive learning control algorithm along with continuous real-

time feedback is then presented to control the valve along a desired trajectory. This trajectory is formulated by

$$y_d(t) = a_1 + \sum_{i=2}^{6} a_i \, t^{(i-1)} \tag{2.9}$$

to ensure sufficient smoothness up to the third order. All coefficients are parameterized such that the set of bounded constraints

$$y_d(t_1) = x(t_1), \qquad y_d(t_2) = x(t_2), \qquad y_d(t_3) = x(t_3)$$
$$y_d(t_f) = 4.0 \text{ mm}, \qquad \dot{y}_d(t_f) = 0.025 \text{ m/s}, \qquad \ddot{y}_d(t_f) = 0.0 \text{ m/s}^2$$

are satisfied. In simulation, Stubb's proposed controller appears effective in tracking a desired trajectory particularly when cyclic position adaptability is applied. Unfortunately, a full assessment on the controller's performance cannot be made without any experimental validations.

A similar control scheme as [Stubbs, 2000] is later published in [Tai et al., 2001] with a slightly different approach in configuring the plant setup and reference trajectory. They presented an EMV model that accounts for mechanical valve lash dynamics and employed linear methodologies to describe the relationship between magnetic force and coil current. In formulating their reference trajectory, $y_d(t)$, takes the simple exponential form of

$$y_d(t) = a\, e^{bt} + c \tag{2.10}$$

with a, b and c coefficients dictated by the following desired boundary conditions.

$$y_d(t_0) = x(t_0), \; \dot{y}_d(t_0) = \dot{x}(t_0), \; y_d(t_f) = 4 \text{ mm}, \; \dot{y}_d(t_f) = \dot{x}(t_f)$$

Experimentally, [Tai et al., 2001] shows open-loop instability in their system with recorded impact velocities ranging between 0.2 - 0.5 m/s. This unstable region is revealed in their mathematical analysis for such systems to occur when the valve moves within one third of its total lift [Tai and Tsao, 2002]. To reduce perturbation sensitivity and improve repeatability, they asserted that feedback control is necessary. The implementation of their proposed control resulted to plant stabilization and valve velocities contacting below 0.05 m/s. Even though impact specifications and power supply limitations are fulfilled, the scheme to fully seat the valve softly required a transition time of 10 ms. It indicates softer springs are used, and therefore, such slow dynamics are not applicable in real engines [Wang, 2001].

Improvements in transition times are accomplished in [Tai and Tsao, 2002] with stiffer springs. They have eliminated the lash adjuster to allow both armature and valve stems to be in direct contact with each other. This minor modification is reflected in their mass-spring system by modeling the connection as a stiff spring. Instead of using current mode and valve positions, feedback control is now based on voltage input mode and armature position measurements. They remarked that closed-loop control is only executed at a range relatively short from landing positions to impede higher energy consumption. Flux leakage and saturation effects are neglected in their force-current and voltage-current relations. A notch filter is included for impact excitation prevention while feedback control is based on Linear Quadratic (LQ) optimal methods to maintain armature motion along its reference. In their work, the design of a trajectory design is avoided by obtaining a reference motion from an experimental cycle in which a tuned open-loop control sequence produces acceptable landing conditions. This tuned control sequence, in turn, would serve as the feedforward signal (or approach control) during and prior to feedback control initiation.

Consistent closed-loop responses and shorter transition times are shown in their experimental results for a 50 cycle test run. The average valve seating velocity is 0.093 m/s with a standard deviation of 0.034 m/s and the armature average seating velocity is 0.048 m/s with a standard deviation of 0.029 m/s. However, such positive responses are only achievable with power supplies exceeding 42 V, and in their case, 50 V and 80 V power supplies are used for testing. The availability of higher voltage simplifies the control problem since the current time-constant is shorter and, in turn, increases the input force bandwidth.

[Tai and Tsao, 2003] enhance the plant model to reflect saturation. Given that force-current relationship in [Tai and Tsao, 2002] does not hold at near seating positions, the equation is modified to

$$F(x,\, i_c) = -\frac{L_0\, g\, i_c^2}{2\,[x+g]^2}\,\rho(x, i_c) \qquad (2.11)$$

where L_0 is the coil inductance constant, g is the gap distance between the stem and housing and $\rho(x, i_c)$ is some constant that varies as a function of air gap and coil current. Using Equation (2.11), they were able to improve previous valve seating results. In a test run of 200 cycles, a mean valve contact velocity of 0.061 m/s with a standard deviation of 0.028 m/s is achieved. Yet, high armature impacts are produced with an average of 0.278 m/s considering the armature position is the main feedback control variable. It seems the experiment has been set up to allow valve landings to occur slightly before the armature lands. At this instance, the armature is traveling at its slowest, which consequently explains why low valve seating velocities are achieved.

Similar to [Tai et al., 2001], [Hoffmann et al., 2003] developed an observer-based output feedback in conjunction with an Iterative Learning Controller (ILC) to achieve desired performance. Feedback control based on Linear Quadratic Regulator (LQR) methodology is executed during the last portion of armature travel to track a desired

trajectory. In doing so, unnecessary control inputs at large distances are avoided since magnetic forces at this range have weak authority. Unfortunately, tracking performances rely heavily on the ILC learning capabilities which can be inhibited if excessive contact velocities exist. The ILC updates approach control signals cyclically based on weighted errors between the actual and desired armature positions. Experimental results using this two stage control structure show significant reduction in contact velocities after 35 cycles at 0.04 m/s with an average travel interval of 3.9 ms. However, a 200 V power supply is required.

A self-tuning nonlinear controller using extremum seeking to reduce impact magnitudes is describe in [Peterson and Stefanopoulou, 2004, Peterson et al., 2004]. This work is motivated by the fact that experimental results in [Peterson et al., 2002] did not achieve desired impact requirements of 0.1 m/s. In extremum seeking control, the controller utilizes measurements of sound impact intensities to tune a nonlinear feedback. Impact velocities below 0.1 m/s and transition times of less than 4.0 ms are achieved with the nonlinear controller having the form

$$U_c = \frac{K_1}{\gamma + x}\dot{x} + \frac{K_2}{\beta + x} \tag{2.12}$$

where K_1, K_2, γ and β are tuning parameters for achieving desired performance. Valve positions are measured with an eddy current sensor, velocities are estimated with a nonlinear observer [Peterson et al., 2002] and impact sound intensities are acquired by a microphone.

Effective application of extremum seeking control is dependent on the appropriate selection of tuning parameter while minimizing a cost function. The cost function is given as follows

$$Q = [S_{des} - S_{meas}(k)]^2 \tag{2.13}$$

where S_{des} is the desired sound intensity and $S_{meas}(k)$ is the measured sound intensity of the armature impacting the coil at the k^{th} iteration. To account for slow-varying unknown factors that affect system performance, only β in Equation (2.12) is compensated cyclically to reduce impact velocity. The authors remark that extremum seeking control methodologies used in their work is intended for static nonlinearities. Adopting it for experimental implementation is conducted by discretizing the control algorithm at a sampling rate equal to the rate of valve events so that the dynamics of the EMV adapts as a static nonlinearity.

By reducing sound intensities, experimental results show a mean impact velocity of 0.07 m/s but requires a 200 V power supply. The use of a microphone for sound intensity measurements is not practical for automotive applications due to a multitude of other sound sources. Furthermore, tuning of parameter β requires long iterations of approximately 40 cycles before low impact converges.

2.4 Summary

In summary, soft landing of the armature and valve is a challenging control problem that requires consideration of several factors that include system nonlinearities, unstable and low control authorities, and varying parameter and disturbances. An overview of various research progress for different EMV control methodologies have been presented and they are summarized in Table 2.2. In most of these proposed strategies, different control strategies are applied in distinct zones in order to achieve desired impact dynamics. Since armature influence at large air gaps is minimal, an approach control scheme is usually enabled during the initial stage of armature travel before soft landing feedback control takes over. This way, energy consumption is more efficient as available force increases greatly with lower current for reducing air gaps [Fulks, 1989, Hoffmann et al., 2003, Peterson and Stefanopoulou, 2004, Tai and Tsao, 2003].

Table 2.2: Control strategies for gas exchange solenoid actuators

CONTRIBUTORS	APPROACH CONTROL	CLOSED-LOOP END CONTROL
[Butzmann et al., 2000]	Adaptive control with quotient observation	Sensorless control based on $\frac{di_c/dt}{i_c} = \frac{\dot{x}}{x}$
[Stubbs, 2000] [Tai et al., 2001]	Cycle-to-cycle learning approach control	Proportional-derivative controller
[Peterson et al., 2002]	N/A	Output observer-based feedback control
[Tai and Tsao, 2002]	Tuned open-loop control	LQ optimal control

continued on next page

Table 2.2: *continued*

CONTRIBUTORS	APPROACH CONTROL	CLOSED-LOOP END CONTROL
[Wang et al., 2002]	Cycle-to-cycle learning approach control	Position feedback
[Gunselmann and Melbert, 2003]	Take-off and approach control	Sensorless control
[Tai and Tsao, 2003]	Repetitive learning approach control	LQR feedback control
[Peterson et al., 2004] [Peterson and Stefanopoulou, 2004]	Extremum seeking to tune nonlinear feedback parameter	Nonlinear feedback control

This thesis presents a new closed-loop solution for low impact actuator control. It assumes an approach control scheme is developed to deliver the armature state to within a certain window tolerance before switching over to an end-control algorithm. The approach control scheme is not the subject of this dissertation and, therefore, it is thus assumed to be working. A flatness-based voltage end controller is proposed to achieve linear stable tracking error dynamics for the final portion of motion. The flat property of the actuator provides a convenient framework for solving tracking problems when trying to meet a number of important motion planning constraints. A flat output is parameterized using B-spline basis functions and a nonlinear constrained problem is solved numerically to obtain a feasible open-loop control. Focus on the performance of the end-control scheme will be demonstrated using simulation and on an experimental testbed.

CHAPTER 3

MODELING AND NONLINEAR CONTROL

One of the most challenging aspects in establishing an EMV model is defining functional relationships to describe nonlinear physical behavior. The exact description of this behavior is difficult due to many complex physical phenomena such as eddy currents, flux leakage and magnetic saturation. However, the success in a robust control design is dependent upon accurate performance predictions while conforming to multiple performance specifications. The dynamic equations that are used here to describe actuator behavior are nonlinear and incorporate model parameters that vary as a function of armature position and coil current. A real prototype gas exchange solenoid valve provided by DaimlerChrysler AG is used to generate experimental data for validating simulation comparison and determining model parameters.

3.1 Mechanical System Model

Consider the electromagnetic solenoid actuator shown schematically in Figure 3.1. The armature position denoted by x, has a range of $x \in$ [-4, 4] mm, with $x = 0$ mm being the midpoint between the two coils. The EMV is modeled by a single degree of freedom mass-spring damped configuration under the following assumptions:

1. The force characteristics of the springs are linear (spring nonlinearities are con-

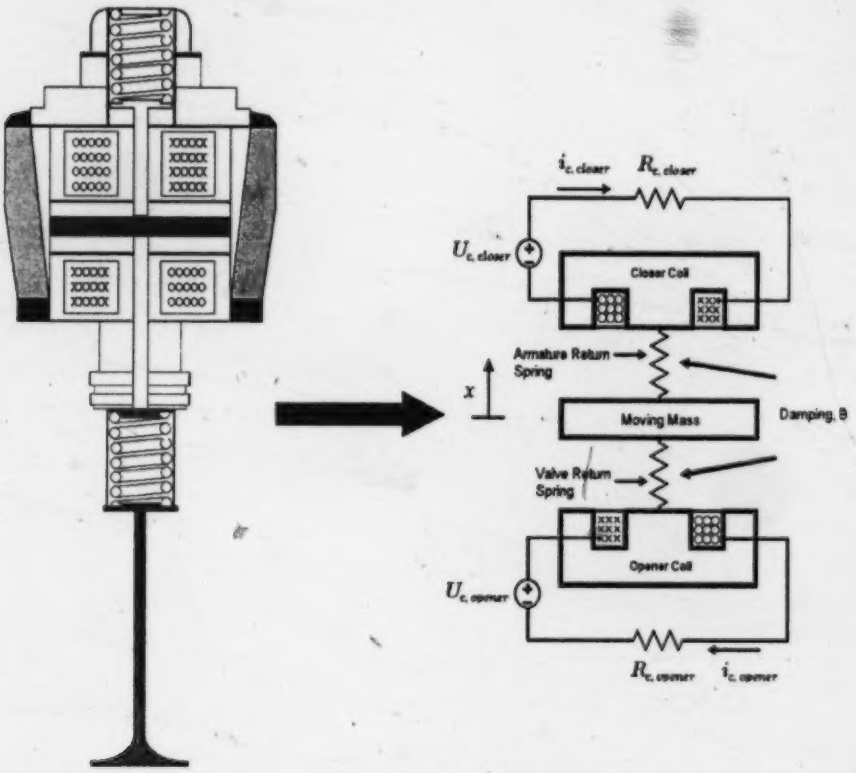

Figure 3.1: Schematic of a two spring solenoid actuator valve

sidered insignificant with small displacements).

2. Modeling the hydraulic lash adjuster is ignored as this device is not implemented in the testbed. The armature-valve connection is considered rigid without separation throughout the range of motion.

3. The dynamics of bounce after first impact are neglected to reduce model complexity. These effects should be minimal if impact velocities at first collisions are low.

4. External disturbances such as cylinder pressure gas forces on the valve are not

tested during experimentation, and hence, will not be considered in the model.

Using Newton's law, the differential equation that describes the mechanical system is

$$m\ddot{x} = F(x,\ i_c) - K_s x - B\dot{x} \tag{3.1}$$

where m is the lumped moving mass, K_s is the total armature and valve spring constant, B is the damping coefficient and $F(x, i_c)$ is the electromagnetic force.

3.2 Electromagnetic Force Model

The electromagnets generate an attracting force to pull the armature towards the coil and to hold the armature when it comes in contact with the coil. The magnetic forces, as shown in Figure 3.2, are prominent when air gap distances between the armature and coil are relatively small. Most force models that were described in Section 2.3 incorporate lumped parameter modeling that do not address complications introduced by saturation effects. When using a simplified model, magnetic forces for small armature distances are overestimated, which results in sharp acceleration prediction errors just before contact [Wang et al., 2002]. Force models, as in Equations (2.3) and (2.4), characterize magnetic force behavior by segregating into two distinct regions. While saturation effects are considered, such models are unwieldy to implement. In this section, a force model which captures nonlinearities and effective for control design is presented.

For high dynamic control performance, nonlinearities of flux linkage, $\lambda(x, i_c)$, are taken into account, namely the saturation of the magnetic circuit. This characteristic is described by a flux linkage-current function that has the form similar to [Ilic'-Spong et al., 1987].

$$\lambda(x, i_c) = \lambda_s \left[1 - e^{-i_c f(x)}\right], \quad i_c \geq 0 \tag{3.2}$$

where λ is coil flux linkage, λ_s is saturated coil flux linkage and i_c is coil current. The function, $f(x)$, is chosen to reflect varying armature positions and it is defined as

$$f(x) = \frac{2C_1}{C_2 - x} + C_3 \tag{3.3}$$

where C_1, C_2, and C_3 are coefficients derived from experimental data. Here, $f(x)$ governs the severity of saturation by influencing the curvature of the profile while λ_s provides flux linkage data as the actuator enters saturation [Torrey and Lang, 1994]. Without available experimental flux linkage data, C_1, C_2 and C_3 are determined from fitting a force function defined by $F(x, i_c)$ to experimental data. $F(x, i_c)$, which is the magnetic force exerted by coils on the armature for both saturated and unsaturated magnetic operations, is obtained by conducting a co-energy analysis. The co-energy function is defined in [Roters, 1941, Schmitz and Novotny, 1965] as:

$$W_c(x, i_c) = \int_0^{i_c} \lambda(x, \xi) d\xi \tag{3.4}$$

Differentiating Equation (3.4) gives

$$F(x, i_c) = \frac{\partial W_c(x, i_c)}{\partial x} \tag{3.5}$$

And by substituting (3.2) into (3.5), the magnetic force function is given by

$$F(x, i_c) = \frac{\lambda_s f'(x)}{f^2(x)} \left[1 - [1 + i_c f(x)]\, e^{-i_c f(x)}\right] \tag{3.6}$$

where $f'(x) = 2C_1/[C_2 - x]^2$. Coefficients λ_s, C_1, C_2, and C_3 are determined by taking a least squares fit to static experimental force data shown in Figure 3.2. Procedures on how steady state force-armature position for constant current input data are acquired can be referred to [Chladny, 2003]. Only the closer coil is considered here and the

coils are assumed to have no magnetic coupling. This is a valid assumption since the end controller in this work uses only the closer coil to land the armature.

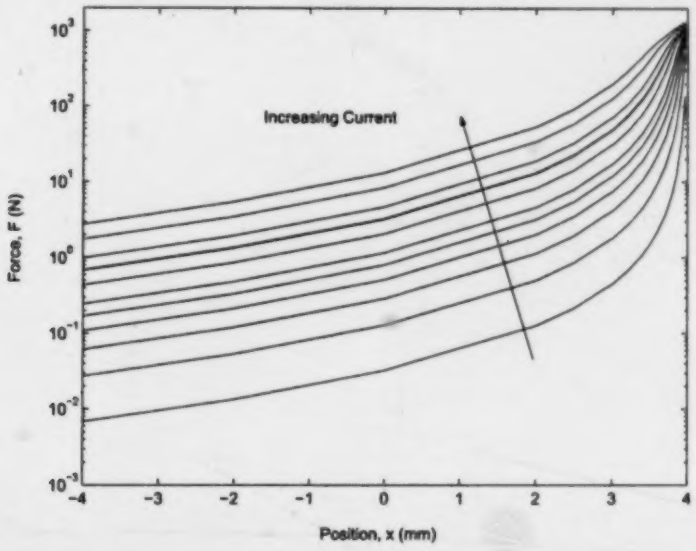

Figure 3.2: Experimental force versus position for varying current

Matlab's optimization toolbox provides a convenient method for solving nonlinear curve-fitting (data-fitting) problems in the least-squares sense. The command, `lsqcurvefit`, solves nonlinear least squares problems via the *Trust-Region* algorithm which allow the user to specify coefficient constraints [Byrd et al., 1988]. Considerable effort has been spent in the curve fitting process for determining C_1, C_2 and C_3 values that are uniform for all constant current inputs without significantly degrading force approximations. Sensitivity to initial guess values for C_1, C_2 and C_3 are observed as `lsqcurvefit` generates a plurality of solutions that give a reasonably good curve fit for each data set. Thus, an iterative approach is taken such that the solved coefficients for each force versus armature position data set (at constant current) does not

fluctuate considerably from one another. The resulting parameters are:

$$\begin{aligned} \lambda_o &= 0.076 \pm \tfrac{0.024}{0.015} \text{ Wb} \\ C_1 &= 2.30e^{-2} \pm \tfrac{0.042}{0.0063} \text{ mm/A} \\ C_2 &= 4.04 \pm \tfrac{0.023}{0.040} \text{ mm} \\ C_3 &= 4.18e^{-4} \pm \tfrac{0.000058}{0.00039} \text{ A}^{-1} \end{aligned}$$

Figure 3.3 shows experimental force data points (shown as crosses) to be in good agreement with (3.6), in particular, the region of control interest where the armature is near the closer coil.

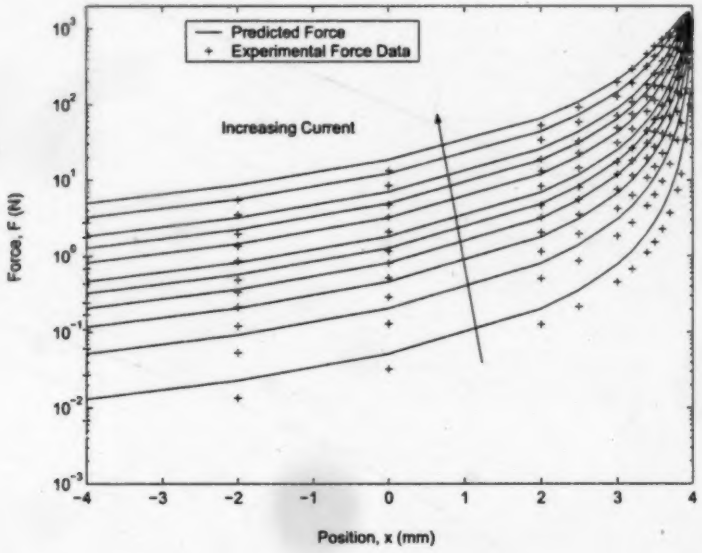

Figure 3.3: Comparison of (3.6) with experimental force

3.3 Electrical Coil Dynamics Model

Electrical coil dynamics models are often represented as an inductor in series with a resistance [Chladny, 2003]. By ignoring the effects of eddy currents, Faraday's law and Kirchhoff's law may be used to show

$$U_c = R_c\, i_c + \frac{d\lambda}{dt}(x,\, i_c) \tag{3.7}$$

where R_c is the coil resistance and U_c is the coil voltage. For this system to achieve accurate simulation results, it is important to account for eddy current effects [Kallenbach et al., 1997]. Accurate predictions of current dynamics results in correct determination of generated electromagnetic forces. Eddy currents are induced as a direct result of flux changes within the actuator coil [Feeley, 1996, Hartwig et al., 2004, Kriezis et al., 1992, Schmitz and Novotny, 1965]. The direction of the eddy currents is such that the flux they produce opposes the flux produced by the primary coil. As a result, net flux is reduced causing electromechanical response times to increase (i.e. an inductive time delay effect) [Feeley, 1996, Hartwig et al., 2004]. However, computing the amplitude and distribution of the eddy currents is a challenging analytic problem [Schmitz and Novotny, 1965] which depends on the nature of the time-varying current flowing in the coil and the position of the armature. A simple model that is useful for eddy currents is an equivalent circuit representation of the electrical subsystem which consist of a secondary branch resistance, $R_e(x, i_c)$, and an inductance, $L_e(x, i_c)$ [Brauer and Chen, 2000, Chladny et al., 2005, Rao, 1964]. Figure 3.4 shows the equivalent circuit with the eddy inductance and resistance in parallel with the magnetizing inductance.

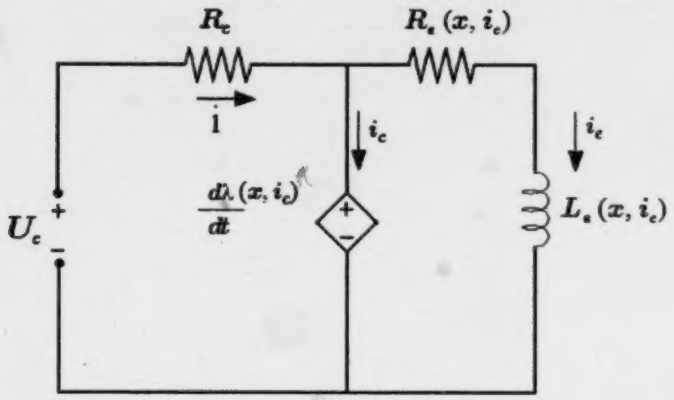

Figure 3.4: Equivalent circuit diagram of the electrical coil subsystem

The coil dynamic equations of this circuit is given by

$$\frac{d\lambda}{dt}(x, i_c) = U_c - R_c[i_c + i_e] \tag{3.8}$$

$$\frac{di_e}{dt} = \frac{1}{L_e(x, i_c)}\left[U_c - R_c[i_c + i_e] - R_e(x, i_c)\, i_e\right] \tag{3.9}$$

$$i = i_c + i_e \tag{3.10}$$

where U_c is the coil input voltage, R_c is the coil resistance, $R_e(x, i_c)$ is the parasitic resistance, $L_e(x, i_c)$ is the parasitic inductance and i_e is the eddy current. The coil resistance, R_c, is measured at room temperature (0.52 Ohms) and it is assumed to be constant. Values for $R_e(x, i_c)$ and $L_e(x, i_c)$ are not constant and difficult to determine as they vary with respect to both current magnitude and armature position. However, a reasonable approximation can be made from transient FEA solutions conducted by [Chladny, 2003]. Using Equation (3.8), (3.10) and an FEA $\lambda(x, i_c)$ look-up table, i_e data can be predicted based on step voltages over a range of air gaps. The parameters $R_e(x, i_c)$ and $L_e(x, i_c)$ are then approximated with Equation (3.9) by performing least squares curve fitting over i_e data. Note that velocity induced eddy currents are

neglected in the model as it is validated in [Chladny et al., 2005] that transient excitation losses are dominant with skin depths estimated at approximately 1 mm.

3.4 EMV System Nonlinear Model

Combining the derived equations in Sections 3.1 to 3.3 results to a nonlinear lumped parameter model of the EMV. Choosing states, x, $\dot{x}$ and i_c, the dynamics of the system are given by:

$$\frac{dx}{dt} = \dot{x} \tag{3.11a}$$

$$\frac{d^2x}{dt^2} = \frac{1}{m}\left[F(x,\, i_c) - K_s\, x - B\dot{x}\right] \tag{3.11b}$$

$$\begin{aligned}\frac{di_c}{dt} &= \frac{1}{\frac{d\lambda}{dt}(x, i_c)}\left[U_c - R_c[i_c + i_e] - \frac{d\lambda(x, i_c)}{dx}\frac{dx}{dt}\right] \\ &= \frac{e^{i_c f(x)}}{\lambda_s f(x)}\left[U_c - R_c[i_c + i_e] - \lambda_s f'(x)\, \dot{x}\, i_c\, e^{-i_c f(x)}\right]\end{aligned} \tag{3.11c}$$

Equations 3.11a and 3.11b describe the mechanical behavior of the actuator. As well, Equation 3.11b represents the magnetic system while Equation 3.11c represents the electrical behavior of the actuator.

3.5 Flatness-Based Control

This section presents a flatness-based static state feedback voltage end-control for the armature to converge exponentially to a desired trajectory. As in [Löewis, 2002, Woittennek, 1999] and [Lévine et al., 1996], flatness provides a convenient framework for solving trajectory tracking problems in context of EMV actuators. Flatness is originally introduced by [Fliess et al., 1992, Martin, 1992] and later extended in [Fliess et al., 1995], [Nieuwstadt et al., 1994] and [van Nieuwstadt and Murray, 1995]. A system is flat if a set of outputs equal in number to the number of inputs is found

such that all states and inputs are expressed in terms of those outputs and their derivatives [Martin et al., 1997, Mercorelli et al., 2003]. To be more precise, if the system has state variables $\dot{x} = f(x, u)$ and inputs $u = (u_1, \ldots, u_m)$, the system is flat if there exist an m-dimensional flat output $y = (y_1, \ldots, y_m)$ of the form

$$y = \gamma\left(x,\ u,\ \dot{u}, \ldots,\ u^{(\alpha)}\right) \tag{3.12}$$

satisfying

$$\begin{aligned} x &= \phi\left(y, \ldots,\ y^{(\beta)}\right) \\ u &= \psi\left(y, \ldots,\ y^{(\beta+1)}\right) \end{aligned} \tag{3.13}$$

This is an important property as the system's behavior can be expressed by its flat output without the need for integration [Martin et al., 1997]. That is, given boundary conditions and trajectory constraints, it would be possible to plan a trajectory in flat output space and then algebraically map back to the original state and input space as shown in Figure 3.5. The concept is powerful in that trajectory generation for flat systems can be reduced from a dynamic problem, requiring high computationally efforts and techniques that are extremely difficult to implement in real-time, to a tractable algebraic problem. However to date, there are no necessary and sufficient conditions for nonlinear systems that suggests the existence of flatness. One would have to use Equations (3.12) and (3.13) to verify the chosen flat output. Given the model describe in Section 3.4, it can be shown that the armature position

$$y = x \tag{3.14}$$

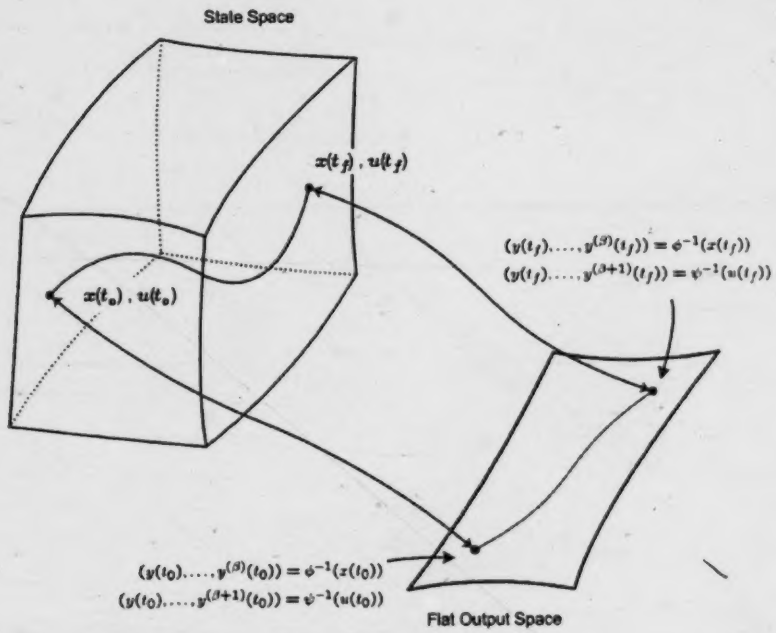

Figure 3.5: Correspondence between flat output space and state space

is a flat output for the actuator. Using Equations (3.1) and (3.14), the states, x, $\dot{x}$ and i_c, can be expressed as functions of y and a finite number of its time derivatives:

$$x = y \tag{3.15a}$$

$$\dot{x} = \dot{y} \tag{3.15b}$$

$$i_c = -\frac{1}{f(y)}\Big[W_{-1}\big(-g(y,\,\dot{y},\,\ddot{y})/e\big) + 1\Big] \tag{3.15c}$$

where

$$g(y,\ \dot{y},\ \ddot{y}) = 1 - \frac{f^2(y)\left[m\ddot{y} + K_s y + B\dot{y}\right]}{\lambda_s f'(y)}$$

and W_{-1} is a real-valued branch of Lambert's W function [Corless et al., 1996]. Note that the argument of W_{-1} is well-defined between $-1/e$ and 0 and $0 \leq g(y,\ \dot{y},\ \ddot{y}) < 1$. Section 3.5.1 provides further details on the derivation of Equation (3.15c) and the Lambert W function.

To obtain an expression for the control input, U_c, the third time derivative of y is taken

$$y^{(3)} = \frac{1}{m}\left[\dot{F}(y, i_c) + K_s\dot{y} + B\ddot{y}\right] \tag{3.16}$$

with

$$\dot{F}(y, i_c) = 2\dot{y}F(y, i_c)\left[\frac{1}{(C_2 - y)} - \frac{f'(y)}{f(y)}\right] + \frac{i_c f'(y)}{f(y)}\left[U_c - R_c\left[i_c + i_e\right]\right] \tag{3.17}$$

to solve for

$$\begin{aligned} U_c = \frac{f(y)}{i_c f'(y)}\Bigg[& m y^{(3)} + K_s\dot{y} + B\ddot{y} - 2\dot{y}F(y, i_c) \\ & \left[\frac{1}{(C_2 - y)} - \frac{f'(y)}{f(y)}\right]\Bigg] + R_c\left[i_c + i_e\right] \end{aligned} \tag{3.18}$$

Based on Equations (3.15) and (3.18), the system is flat with all its states and input expressed locally as a function of a finite number of y time derivatives. Consequently, convenient methods for solving trajectory tracking problems exist [Fliess et al., 1995, 1999]. The trajectory is determined in flat output space and, in turn, Equation (3.18) can be used to obtain feedforward control inputs. Note that this equation has a singularity at $i_c = 0$, however, the trajectory optimization in Section 3.5.2 ensures

nonzero open-loop current. The next step is to augment this feedforward control with a feedback control law that forces the system to track a desired trajectory when there are disturbance and system parameter variations.

3.5.1 The Lambert W Function

The Lambert W function [Corless et al., 1996] was first introduced by Euler in 1779 [Euler, 1779] when he studied Lambert's transcendental equation in [Lambert, 1758]. It is defined to be the multivalued inverse of the function $w \mapsto we^w = z$, $z \in \mathbb{C}$. It is the solution to

$$W(z)e^{W(z)} = z \tag{3.19}$$

In the complex plane, Equation (3.19) has a countably infinite number of solutions that are represented by k branches ranging over integers. If only real arguments are used, then for all real $z \geq 0$, Equation (3.19) has exactly one real solution that is represented by the principal branch, W_0, in Figure 3.6. For all real z in the range $0 > z > -1/e$, the function is multivalued with two real solutions that are represented by the W_0 and W_{-1} branches. Given that coil current, i_c, is defined as a state in Section 3.4 and it is a fundamental parameter for calculating the open-loop trajectory in Section 3.7, the Lambert W function is used to solve for i_c.

By rearranging Equation (3.1) to

$$\left[1 + i_c f(y)\right] e^{-i_c f(y)} = 1 - \frac{f^2(y)\left[m\ddot{y} + K_s y + B\dot{y}\right]}{\lambda_s f'(y)} \tag{3.20}$$

the following equation can be formulated to have a similar form as in Equation (3.19).

$$-\left[1 + i_c f(y)\right] e^{-\left[1+i_c f(y)\right]} = -g(y, \dot{y}, \ddot{y})/e \tag{3.21}$$

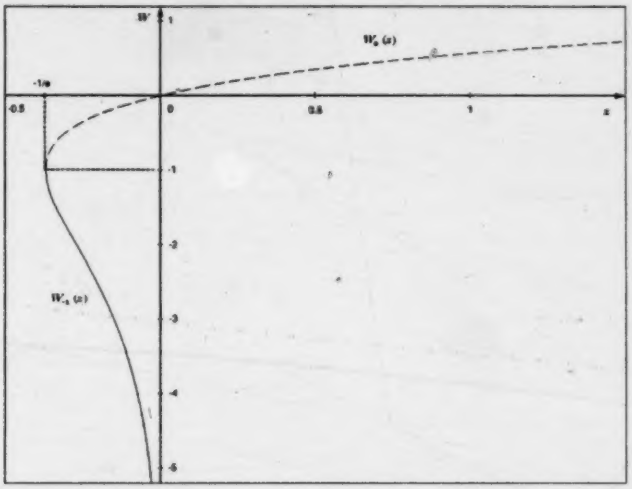

Figure 3.6: Two real branches of the Lambert W function

Solving Equation (3.19) for i_c gives

$$i_c = -\frac{1}{f(y)}\left[W_{-1}(-g(y,\ \dot{y},\ \ddot{y})/e) + 1\right] \tag{3.22}$$

For $i_c \geq 0$, the principal real branch, $W_{-1}(z)$, is considered. since the argument z varies from -1 to -∞.

3.5.2 Feedback End-Control

Although the flatness-based strategy solves the open-loop trajectory tracking problem, an additional feedback can be determined to compensate the effect of external disturbances and system parameter variations. Disturbances that include power supplies, temperature, sensor noise and several other uncertain factors can affect armature motion.

Letting y_d denote the desired trajectory for the armature and $\widetilde{y} = y - y_d$ denote

tracking error with $y = x$, linear error dynamics of the form

$$\tilde{y}^{(3)} + k_2\ddot{\tilde{y}} + k_1\dot{\tilde{y}} + k_0\tilde{y} = 0. \tag{3.23}$$

are chosen. The coefficients k_0, k_1 and k_2 are real such that the third degree characteristic polynomial $P_3(s) = s^3 + k_2s^2 + k_1s + k_0$ is Hurwitz. Recall that this property ensures that all three roots of P_3 have negative real parts which results in exponential system stability. Provided the controller gains, k_0, k_1 and k_2, are positive and selected appropriately, y locally converges to y_d exponentially. Solving Equation (3.23) for $y^{(3)}$ gives

$$y^{(3)} = y_d^{(3)} - k_2\ddot{\tilde{y}} - k_1\dot{\tilde{y}} - k_0\tilde{y} \tag{3.24}$$

and substituting this expression for $y^{(3)}$ into (3.18) generates an expression for the closed-loop voltage control which is

$$\begin{aligned} U_c = \frac{f(y)}{i_c f'(y)}\Bigg[& m\left[y_d^{(3)} - k_2\ddot{\tilde{y}} - k_1\dot{\tilde{y}} - k_0\tilde{y}\right] + K_s\dot{y} + B\ddot{y} \\ & - 2\dot{y}F(y, i_c)\left[\frac{1}{(C_2 - y)} - \frac{f'(y)}{f(y)}\right]\Bigg] + R_c\left[i_c + i_e\right] \end{aligned} \tag{3.25}$$

The block diagram of the flatness-based end-control is shown in Figure 3.7.

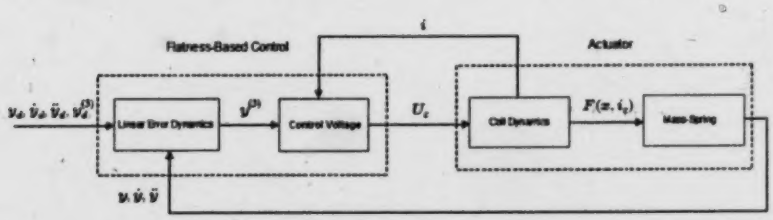

Figure 3.7: Scheme of the flatness-based end-control loop for the actuator

3.6 System Identification of Mass-Spring Properties

The EMV actuator that is used in this work differs slightly in moving mass to those described in [Koch et al., 2002] and [Koch et al., 2004] as it uses a custom eddy current armature position sensor. Armature position for free oscillations are experimentally measured and system identification is used to determine the mass-spring parameters. Neither coils are energized after the armature's release from the closer coil and in order to exclude the effect of back electro-magnetomotive forces (EMF), initial data after the armature release is ignored. Recall that back EMF is generated from changing magnetic field passing through the coil windings. Even when reverse polarity voltages (i.e. (quasi) -42 V) are applied to achieve faster armature release [Peterson et al., 2002], initial armature travel after its release from the closer coil will temporarily developed back EMFs. This will cause a slight increase in coil current and generate magnetic forces to attract the armature [Wang et al., 2002]. The coil resistance, R_c, for the closer coil (after it has been warmed up) is measured at 0.52 Ω at room temperature and it is considered constant without temperature variation.

Matlab's System Identification toolbox [Ljung, 1987, 2004] is used to estimate m, K_s and B for the defined mass-spring structure given by Equation (3.26). In this case, a simple state-space structure is sufficient in estimating plant parameters accurately for a given input and output response. It provides the ability to explicitly define which parameters are to be estimated as well as specify system initial conditions. The state variables are selected as $x_1 = x$ and $x_2 = \dot{x}$ to give

$$\begin{bmatrix} \dot{x_1} \\ \dot{x_2} \end{bmatrix} = \begin{bmatrix} 0 & 1 \\ -\frac{K_s}{m} & -\frac{B}{m} \end{bmatrix} \begin{bmatrix} x_1 \\ x_2 \end{bmatrix} + \begin{bmatrix} 0 \\ \frac{1}{m} \end{bmatrix} u$$

$$y_{output} = \begin{bmatrix} 1 & 0 \end{bmatrix} \begin{bmatrix} x_1 \\ x_2 \end{bmatrix} \tag{3.26}$$

Note that u in Equation (3.26) is equal to $F(x, i_c)$ which is zero since neither coils are energized to generate electromagnetic force. A starting value of the parameters is required to initiate the identification procedure. Performing a prediction error estimate (Matlab's `PEM` command) returns a good fit of 97.08 % with the following estimated parameters

$$\begin{aligned} m &= 0.28 \text{ kg} \\ K_s &= 250.98 \text{ N/mm} \\ B &= 12.75 \text{ Ns/m} \end{aligned}$$

Figure 3.8 shows the measured and fitted positions while Figure 3.9 shows that the error is less than 8×10^{-5} m. However, for small armature motion (not shown in the figures), the error increases which perhaps is due to non-linear friction force. Cross-validation of the mass-spring model based on the above estimated parameters is not conducted in this work. The parameters are considered to remain relatively constant since the experimental testbed is setup in a controlled environment where temperature variations and external disturbances are minimal.

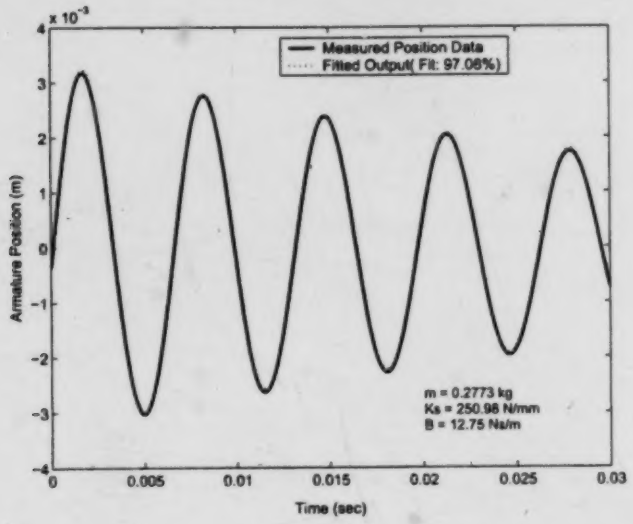

Figure 3.8: Plant model parametrization

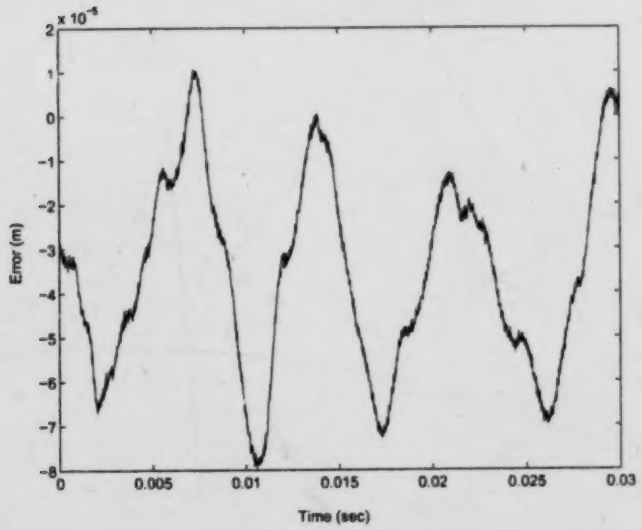

Figure 3.9: Error between measured and fitted armature positions

3.7 Open-Loop Trajectory Design

To implement flatness-based control, a suitable desired trajectory, y_d, must be defined for the system given by Equation (3.11). The objective is to move the actuator's armature from an initial state to a known final state that minimizes impact velocity at the instance of first collision with the coil. The following nonlinear programming procedure in Section 3.7.1 finds a trajectory that connects the initial and final state while taking into account of magnetic saturation, eddy current effects, armature motion constraints and voltage limits. This dissertation considers control of the armature for the final fraction of travel using the closer coil and, as such, this control scheme is termed "end-control". A rigid connection between the armature and valve is assumed which implies the armature and valve have similar dynamics. Hence, low impact control of the armature will translate to low valve seating velocity. To ensure existence of a feasible trajectory, it is essential that realistic values (based on experimental observations) are specified for initial and final armature state conditions in the design routine.

3.7.1 Nonlinear Constrained Problem

In general, a nonlinear optimization problem can be formulated into the following form

$$\begin{aligned} &\min_X F(X) \\ &\text{subject to: } A\,X \leq B \quad \text{(Linear Constraints)} \\ &\qquad\qquad A_{eq}\,X = B_{eq} \quad \text{(Linear Equality Constraints)} \\ &\qquad\qquad C(X) \leq 0 \quad \text{(Nonlinear Constraints)} \\ &\qquad\qquad C_{eq}(X) = 0 \quad \text{(Nonlinear Equality Constraints)} \end{aligned} \tag{3.27}$$

where $[A,\ A_{eq},\ B,\ B_{eq},\ C(X),\ C_{eq}(X),\ X] \in \mathbb{R}^n$. Solving a nonlinear constrained optimization problem as in (3.27) can be very difficult, which requires minimizing X for a nonlinear cost function $F(X)$ to a set of linear and nonlinear constraints [Milam, 2003]. The implementation of program algorithms to solve such a problem can take many iterations and function evaluations. In this dissertation, the trajectory design modifies (3.27) by neglecting the minimization of $F(X)$. Instead, a nonlinear feasibility problem will be solved such that the parameterized y_d will satisfy imposed trajectory constraints. Considering the particular case of the armature towards the closer coil, the position constraints are subjected to

$$y_d(t_0) = 2.55 \text{ mm} \tag{3.28}$$

$$y_d(t_f) = 4.00 \text{ mm} \tag{3.29}$$

where t_0 is the time at which the end control is turned on, and t_f is an unknown free time variable that defines when the armature lands.
The constraints on armature velocity are

$$\dot{y}_d(t_0) = 2.59 \text{ m/s} \tag{3.30}$$

$$\dot{y}_d(t_f) \leq 0.10 \text{ m/s} \tag{3.31}$$

Constraint (3.31) is critical in ensuring reduced wear and acoustical noise. The constraints on acceleration are

$$\ddot{y}_d(t_0) = \frac{1}{m}\left[F(y_d(t_0), i_c(t_0)) - K_s' y_d(t_0) - B\dot{y}_d(t_0)\right] \quad \text{m/s}^2 \tag{3.32}$$

$$\ddot{y}_d(t_f) = 0.0 \quad \text{m/s}^2 \tag{3.33}$$

$$\ddot{y}_d(t) > -\frac{1}{m}\left[K_s y_d(t) + B\dot{y}_d(t)\right] \quad \text{m/s}^2, \quad t_0 < t < t_f \tag{3.34}$$

$$i_c(t_0) = 8.9 \quad \text{A} \tag{3.35}$$

Constraint (3.34) is required as the coil can only attract the armature. Since an approach control scheme (not part of this dissertation) is initiated prior to the end control phase, a coil current is prescribed at the end of the approach phase to inhibit large initial control voltage requirements (or singularities) at $t = t_0$. Also, an advantage for applying a preset current prior to enabling end control is that it allows anticipation for significant coil inductance (back EMFs) by ensuring sufficient flux levels are available within the coil [Hoffmann et al., 2003, Peterson and Stefanopoulou, 2004].

Given that Equation (3.18) is an explicit expression for the control input of these coils, the design voltage is

$$|U_c(t)| \leq 42 \text{ V}, \quad t_0 \leq t \leq t_f \tag{3.36}$$

This is chosen to match the experimental actuator design requirements and possible future 42 V on-board vehicle voltage standard [Chang et al., 2002]. However, constraint (3.36) cannot be enforced directly into the nonlinear constraint program problem due to Equation (3.9) that varies as a function of U_c, i_c and i_e. Instead, the constraint is modified by assuming variations of $R_c i_e$ in Equation (3.18) to be reasonably small and constant with $R_c i_e = 3$ V as the armature approaches the closer coil. This gives

$$|U_c(t) - R_c i_e| \leq 39 \text{ V}, \quad t_0 \leq t \leq t_f \tag{3.37}$$

which can easily be implemented as a nonlinear inequality constraint. Experimental test procedures using an open-loop current scheme require current magnitudes of ap-

proximately 10 to 15 A to ensure the armature lands successfully. Since coil resistance is measured to be 0.52 Ω and eddy current effects are assumed to be approximately half of the total current, i, the presumption $R_c i_e = 3$ V is valid. Thus Equation (3.37) is a more stringent constraint to determine a trajectory than the original constraint in Equation (3.36).

3.7.2 Parametrization of the Flat Output Trajectory

In Section 3.5, the nonlinear dynamic problem has been reduced to an algebraic problem by selecting a set of flat outputs that completely characterize the actual states and inputs of the actuator. Section 3.7.1 provides a nonlinear programming foundation to give a solution for the trajectory generation problem. This section will discuss how the desired trajectory, y_d, is parameterized with B-spline basis functions. An overview of B-splines from which the following is derived can be found in [Löewis and Rudolph, 2003] and [Boor, 1978].

The advantage of using B-spline basis functions is that continuous derivative operations can be computed with relative ease from spline coefficients. Since the actual states and input, in this case, are a function of the flat output and its derivatives, the spline function should be smooth such that its third time derivative along the curve is continuous (see Equation (3.25)). Besides providing an accurate basis solution to the trajectory generation problem, B-spline basis functions are numerically stable for handling complex nonlinear problems. For this reason, they are favored here over other functions such as higher order polynomials. A single high order polynomial would be necessary to satisfy the prescribed constraints and solving for the coefficients would be inefficient and ill-conditioned [van Nieuwstadt and Murray, 1995].

Following [Löewis, 2002], the desired trajectory, y_d, is defined by

$$y_d(t) = \theta^T B_k(t), \quad t = t_0, \ldots, t_f \tag{3.38}$$

where θ is a vector of spline coefficients and B_k is a vector of B-spline basis functions of order k for the knot interval $[t_0, t_f]$. The knots are taken to be strictly increasing sequence of real numbers with each knot representing the point at which the basis functions are joined. As long as $B_k(t) \neq 0$ over the interval $[t_0, t_f]$, it is possible to determine a $y_d(t)$ that matches the constraints given in Section 3.7.1 [Boor, 1978].

The nonlinear constrained problem is solved via Matlab's Spline and Optimization Toolboxes to obtain optimal spline coefficients, θ, that meets the prescribed constraints. It is important when using `fmincon` that the initial guess to θ is sufficiently close to a solution in order to guarantee convergence of the method. Sequential quadratic programming (SQP) method is used by `fmincon` at each iteration to solve a quadratic program (QP) subproblem whose solution is used as a search direction for a line search procedure. An overview of SQP can be found in [Gill et al., 1981]. Due to Equation (3.18), fourth order (i.e. $k = 5$) B-splines over evenly spaced simple knots on $[t_0 = 0, t_f = 0.00184]$ sec are taken, as shown in Figure 3.10, to ensure Equation (3.18) is continuous in time.

Conditions (3.28), (3.29), (3.30), (3.32) and (3.33) are passed to `fmincon`'s optimization of θ as linear equality constraints. Condition (3.31) is a linear inequality constraint on θ. As well, conditions (3.34) and (3.37) are discretized as nonlinear inequality constraints. The solution is sensitive to knot selections and by choosing a suitable transient time from $t_0 = 0$ to $t_f = 0.00184$ s, a feasible trajectory is obtained with the following optimal spline coefficients

$$\theta^T = 1.00e^{-3}\begin{bmatrix} 0.87 & 2.10 & 3.06 & 3.68 & 3.96 & 3.99 & 3.97 & 4.03 & 4.01 \end{bmatrix}^T$$

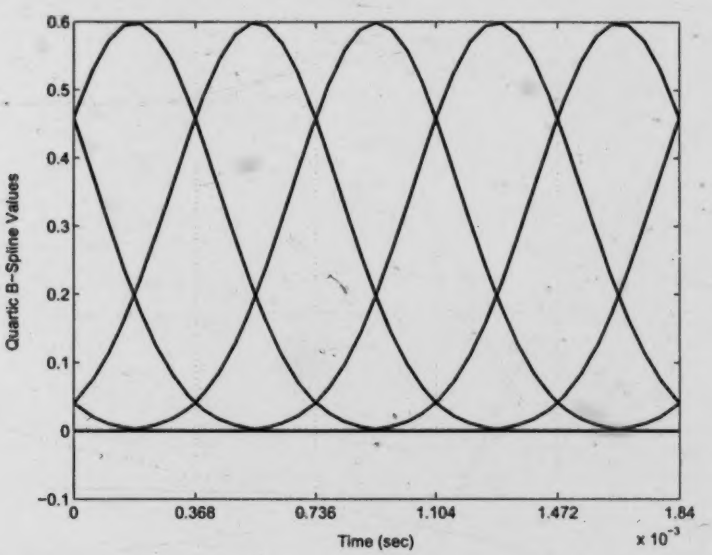

Figure 3.10: Quartic B-splines over $[t_0,\ t_f]$

Figures 3.11 to 3.15 shows the desired armature motion along with open-loop coil current inputs for feedback end-control. Finally, Figure 3.16 shows the desired voltage control input, U_c, assuming $R_c i_e = 3$ V for $y_d(t)$ where $0 \leq t \leq 0.00184$ s, are within 42 V at each knot instance. It is important to note that on the experimental testbed, the voltage level inputs are not continuous but are approximated by a high frequency Pulse Width Modulated (PWM) on/off voltage switch using power electronics (see Section 4.3.5). Negative voltages are realizable as the power electronics (see Section 4.3.5) in the actual system provides three output modes (+ 42 V, 0 V and (quasi) -42 V) for regulating voltage to the actuator coils.

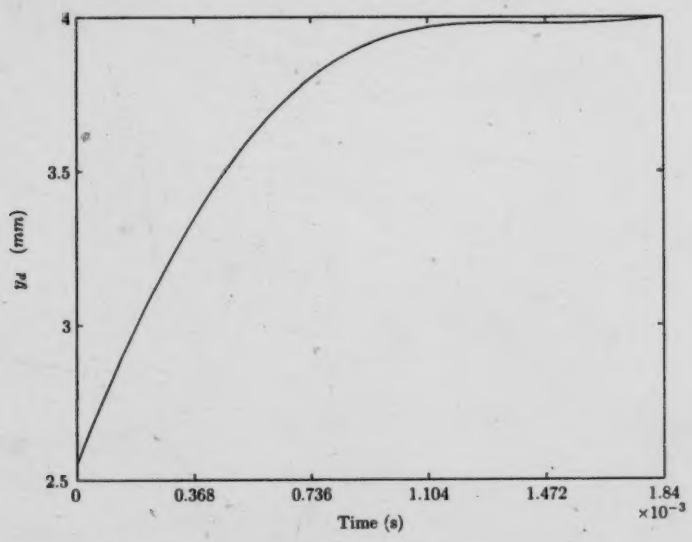

Figure 3.11: Reference armature position (y_d)

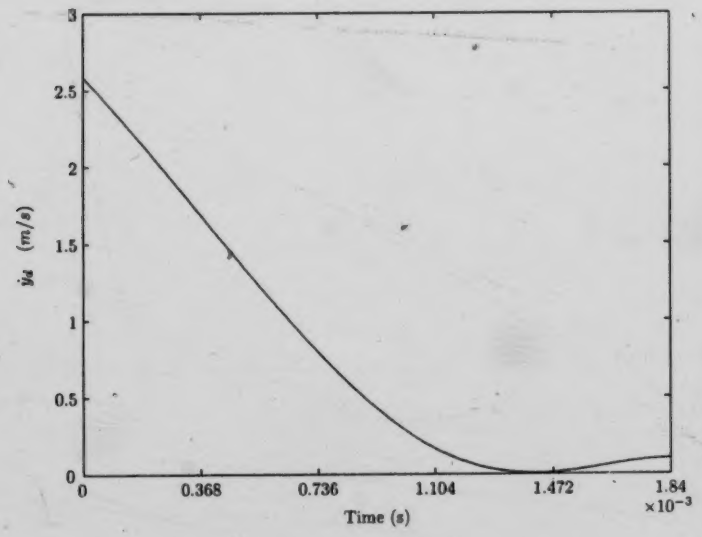

Figure 3.12: Reference armature velocity ($\dot{y}_d$)

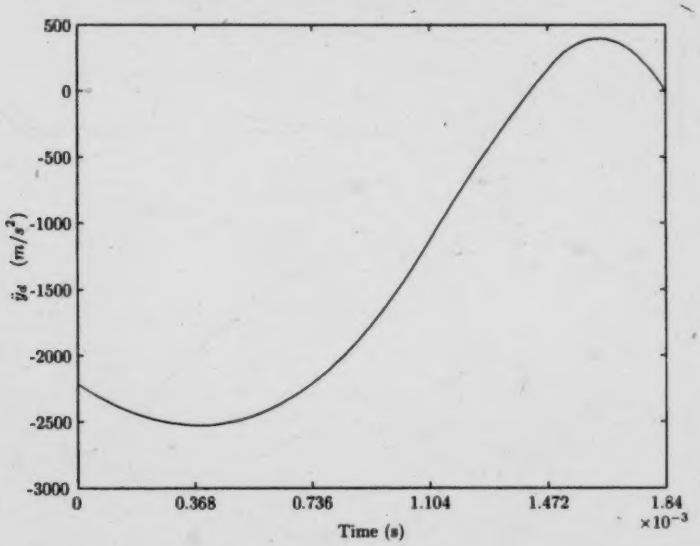

Figure 3.13: Reference armature acceleration ($\ddot{y}_d$)

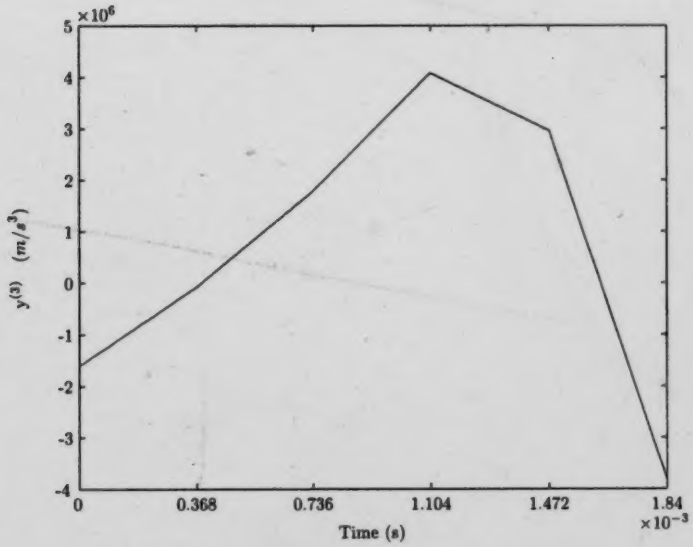

Figure 3.14: Reference armature jerk ($y_d^{(3)}$)

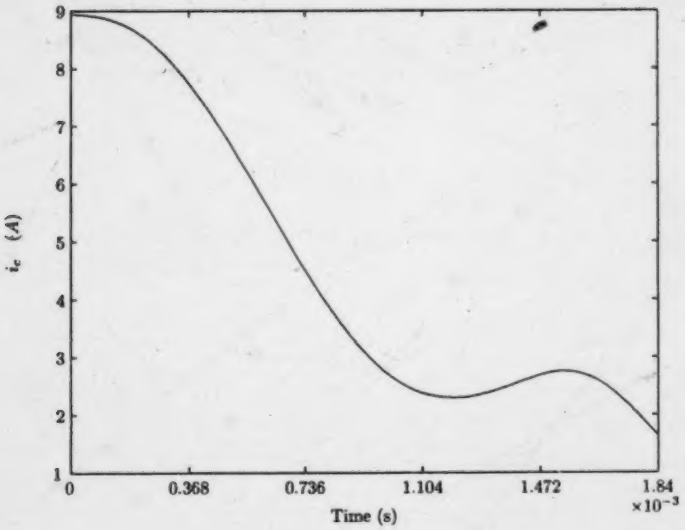

Figure 3.15: Reference coil current (i_c)

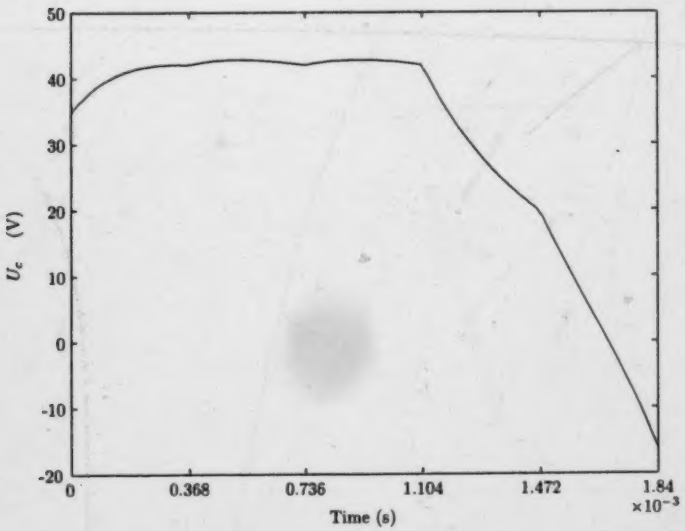

Figure 3.16: Reference coil voltage (U_c)

3.8 Summary

This chapter presents a lumped parameter model of the solenoid actuator which includes magnetic saturation and eddy current effects. By taking into consideration of these nonlinear properties, simulation accuracy can be improved as well as correct calculation of voltage control inputs. A system identification scheme has been used to parameterize the mechanical subsystem that is represented by a simple mass-spring model. For the electrical coil system, a simple equivalent circuit model is used to approximate coil currents and eddy currents with reasonable accuracy. Computing exact eddy current magnitude is challenging, however, transient FEA $\lambda(x, i_c)$ data can be used to determine parasitic inductance and resistance values. Since the main focus in this dissertation is on seating control, saturation effects in electromagnetic forces are essential to the modeling procedure. This nonlinear force behavior is represented by a continuous function that provides a relation between electromagnetic force and current for every armature position.

A flatness-based voltage end-control has been derived to provide linear stable tracking error so that low impact velocity can be maintain. The differential flatness property of this actuator allows an open-loop trajectory to be designed using nonlinear constrained programming and B-spline basis functions to parameterizes the flat output. Further details on the proposed scheme implementation for simulation and real-time experimentation are discussed in Chapter 5.

CHAPTER 4

EXPERIMENTAL SETUP AND APPARATUS

This chapter briefly describes the experimental testbed setup for a prototype EMV actuator. The setup is used primarily to evaluate flatness-based voltage end-control and to validate the proposed analytic model. Although these actuators are designed to function as gas exchange valves in internal combustion (IC) engines, here the testing is conducted in the lab on a testbed. Figure 4.1 shows the actual apparatus along with dedicated peripherals required for control execution and data acquisition. Most of the equipment discussed in this dissertation are similar to the apparatus described in [Chladny, 2003]. General specifications for these equipment can be referred to Table 4.1.

4.1 EMV Actuator

A linear prototype solenoid actuator built by TEMIC (donated by DaimlerChrysler AG) is used for testing the proposed control scheme. The EMV is designed to provide fast response times of approximately 4 ms and high holding force capabilities over a stroke of 8 mm. A partial sectional view of the actuator is shown in Figure 4.2.

The actuator uses two preloaded linear compression springs to achieve fast valve flight times while minimizing electrical energy input as well as overcoming friction and gas disturbances. Spring stiffness is selected such that the system's undamped

Figure 4.1: Experimental testbed setup

natural frequency is approximately 150 Hz in order to accommodate a maximum IC engine speed of 5000 $\sim$ 6000 RPM [Chladny et al., 2005]. Since this system operates as a mass-spring oscillator, the armature motion and lift is dependent on its natural frequency regardless of crank rotational speed. Thermal expansions can affect spring properties, however, these variations are small and thus are ignored. Coil-wounded electromagnets are used specifically for attracting and holding the armature at either stroke bound. The closer coil has 79 turns and the opener coil has 72 turns. Flat pole and armature geometries provide large surface areas and minimal fringing for maximum force per actuator volume [Roters, 1941]. However, such a configuration has an inherent nonlinear force vs position relationship as shown in Figure 3.2.

The back iron of the actuator is constructed out of QStE500 sintered powder

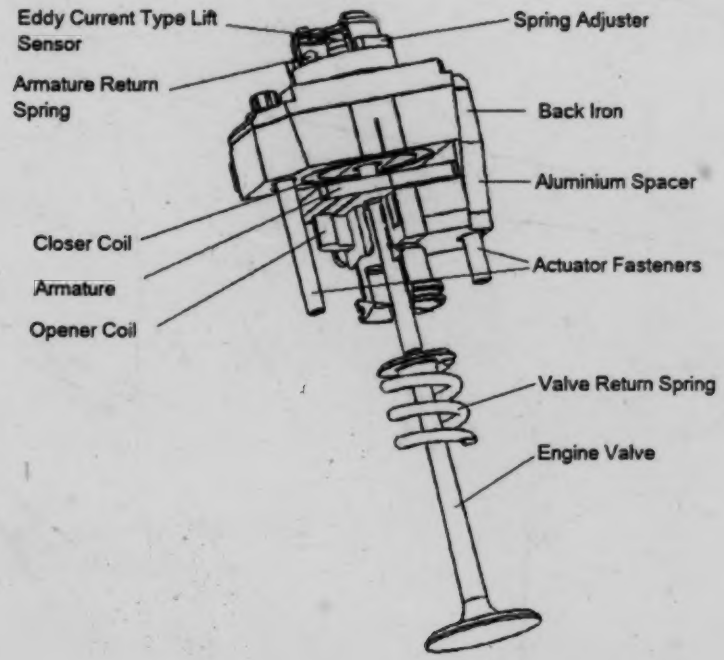

Figure 4.2: TEMIC actuator and valve sectional view [Chladny, 2003]

steel material while the armature is made from Vacoflux silicon steel. Adopting such fine grain materials are intended to mitigate eddy current progressions, however, the occurrence of resistive and eddy current heating was found at peak current loads in excess of 40 A [Chladny, 2003]. Aluminium spacers are also used to reduce flux flow from one coil to another without passing through the armature.

In this dissertation, only experimental results from the closer are presented since they are representative of landing the valve on its valve seat. The validation of flatness-based end-control for low impact armature seating on the closer coil is the main goal of this work. The physical parameters of the actuator that include moving mass, spring constant and damping coefficients are not physically measured but rather estimated by system identification techniques (see Section 3.6). Actuator operation

is similar in principle to [Chladny, 2003, Koch et al., 2004] but differs in position measurement capability due to a built-in Eddy Current type lift position sensor.

4.2 Computer Hardware and Software

The experiment employs a Microsoft Windows 2000 operating System host personal computer (PC) and a DS1103 PowerPC (PPC) target controller board. Communication between the controller board and the host PC is established via a standard peripheral component interconnect (PCI) card in the host PC and an industry standard architecture (ISA) card bus in the target backplane. This interface between the host and target provides a bidirectional communication for program download and real-time data transfer. The target controller consist of a master and a slave processor (see Section 4.2.1).

Control and plant models are developed in Matlab 6.5.1 Release 13 - Simulink 5.1 environment. However, for real-time implementation, all control tasks are written in C language (refer to Appendix C for the control algorithm structure). This code is compiled and linked on the host and downloaded to the target board. The target is then controlled and managed on the host PC by dSPACE's experimental software (ControlDesk 2.4) that allows a user to define a graphical user interface for data acquisition, data plots and various parameter instrument panels. Figures 4.3 and 4.4 shows the constructed virtual template.

4.2.1 dSPACE DS1103 Controller Board

For this work, the dSPACE DS1103 controller target board is set to a 50 kHz sample rate while executing control algorithms. All task algorithms are coded in C language, compiled and downloaded from the host PC to its DS1103 board. The DS1103 board comes equipped with a separate 400 MHz master PPC 604e microprocessor and a

Figure 4.3: ControlDesk data collection template

Figure 4.4: ControlDesk parameter instruments template

20 MHz Texas Instruments TMS320F240 Slave processor with extensive I/O capability [dSPACE GmBH, 2003]. ControlDesk 2.4 is an experimental software developed by dSPACE to provide real-time experiment management. Figure 4.5 shows the control board as well as its microprocessor.

Figure 4.5: dSPACE DS1103 controller board and PowerPC 604e microprocessor

Primarily, the control board acquires and evaluates current and armature position measurements, and outputs dedicated control signals to the respective power transistors located within a custom designed power electronics shown in Section 4.3.5. Digital I/O signals and PWM signals (handled by the slave processor) are transmitted to respective transistors in order to regulate voltage in the closer coil.

4.3 Testbed Setup and Equipment

The testbed setup is located in the Mechanical Engineering Building (4^{th} floor, Controls Laboratory) at the University of Alberta. Figure 4.6 shows the actuator assembly for fastening the prototype actuator in a horizontal position.

Facing to this assembly is a valve assembly which consist of a valve body, a valve return spring and a non-contact eddy current displacement sensor. The valve assembly is bolted down while the actuator assembly is fastened to a steel stage that

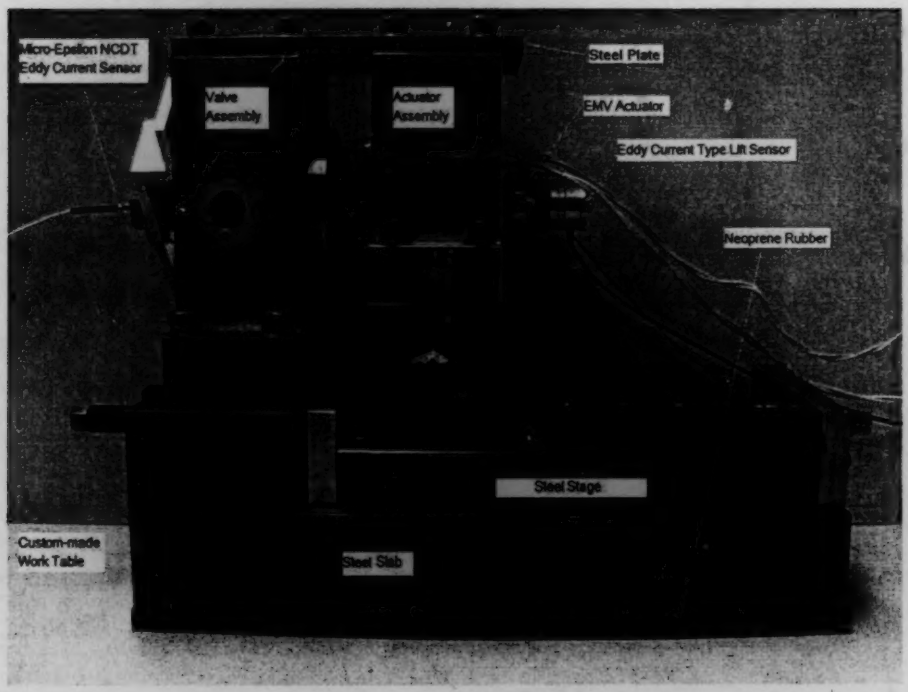

Figure 4.6: Testbed setup

allows relative horizontal displacement adjustment. Since a hydraulic lash adjuster is not implemented, this adjustment is necessary to ensure proper centering and contact of both actuator and valve. A steel plate is fastened above both assemblies to prevent bending during operation. Underneath the steel stage, a steel slab is used as the main mount and sits on a layer of neoprene rubber to dampen vibrations generated during test runs. Finally, the entire apparatus is bolted through steel members of a a custom-made work table.

4.3.1 Power Supplies

A Sorenson DCS60-18E 1kW programmable switching power supply (120 VAC input) is employed in the experiment to drive custom-built power electronics that are used for

actualizing the prototype EMV. The power electronics can switch the supply voltage up to 60 VDC. Although the power supply is rated to a maximum of 18 A, [Chladny, 2003] observed that this device can provide currents in excess of 50 A at 50 VDC in short periods of less than 5 ms. This transient response is ideal for the intended test application since it may require current loads of up to 35 A for short periods of time. An external overload protection circuit provides a remote shutdown of the power supply in the event of current overload. This experiment sets the power supply to 42 VDC to comply with how the design voltage of the actuator which conforms with emerging voltage standards for future vehicles [Kassakian et al., 1996].

A Hewlett Packard 6236B triple output linear power supply is used to provide continuous +5 VDC and ±15 VDC power source to several equipment. Some of the power electronics circuitry and overcurrent protection circuit requires a +5 VDC source while the power electronics on-board hall effect current sensors and opto-isolator requires input of ± 15 VDC. Figure 4.7 shows both power supplies.

Figure 4.7: Sorenson DCS60-18E and Hewlett Packard 6236B power supplies

4.3.2 Circuit Protection

A important requirement for the solenoid valves is proper protection from overcurrents. Overcurrent can cause irreversible damage to the actuator coils by overheating and melting coil insulation. This experiment incorporates hardware fault protection devices to prevent damage of the actuator and dSPACE control board in the case of a system failure.

4.3.2.1 Overcurrent Protection Circuit

An overcurrent protection device shown in Figure 4.8 prevents damage of EMV coils from large steady current flow levels. The device filters current signals measured from a Hall-effect current sensor and compares the low-pass filtered signal to a shutoff threshold. Should a software or power electronics error (i.e. low frequency current greater than shutoff limit) occur, the device will trigger a signal to the Sorenson power supply for immediate shutdown. The shutoff threshold is manually adjusted to allow a suitable current limit. Electrical schematics of the overcurrent device can be referred to Figure B.1.

Figure 4.8: Overcurrent protection circuit

4.3.2.2 Opto-Isolator

The implementation of an opto-isolator allows both DS1103 control board and power electronics to be connected to each other without running into any risk of damage from electrical transients such as spikes and surges. If such transients occurs from the power electronics, the control board should be unaffected due to an optical isolator. Figure 4.9 shows the physical opto-isolator component while Figure B.2 shows the electrical schematics. The use of a 6N137, HCPL-2601/2611 single-channel opto-coupler provides high speed switching times of 10MBit/s such that signal delays are minimized. Working principles of a opto-isolator may be referred to [Mooney, 1981] and [Fairchild, 2005].

Figure 4.9: 16 channel opto-isolator

4.3.3 Current and Voltage Sensing

A Hall-effect current sensor manufactured by LEM (LA55-P) is used to measure current flow generated on-board the power electronics. The sensor is implemented as part of the power electronics circuitry and measures current through an actuator

coil. The sensor functions by directing magnetic field ($B = \frac{\mu_0 I}{2\pi r}$) produced by a flowing current into a semiconducting material using a steel yoke. When an impinging field exist, a positive current, i_p, is produced, translating to a voltage potential, V_H, in the hall element. An op-amp then generates a current flow, i_s, through a secondary winding. This i_s is proportional to V_H and acts as an opposing flux to compensate the induction created by the semiconducting material. Since i_s is an exact representation of i_p, i_s is the intended current for measurement. The op-amp voltage is measured and related to the current flow in the conductor by $V_M = \frac{I_s R_M}{N}$. By achieving practically zero magnetic flux, the sensor is considered linear over a wide measuring range. Figure 4.10 shows the actual current sensor and Figure 4.11 illustrates the sensor schematically.

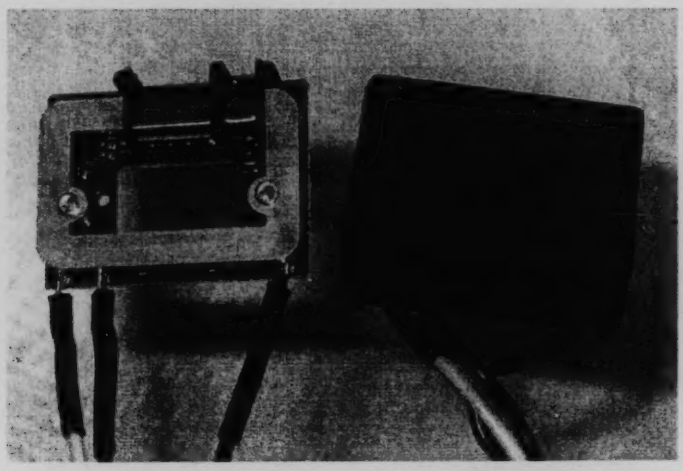

Figure 4.10: LEM LA55-P hall-effect current sensor

Coil voltage, U_c, in the dSPACE controller is measured by dividing coil voltage with a differential operational amplifier circuit. The value of the gain and resistors are chosen such that the output voltage is a convenient fraction of the actual voltage across the coil. Figure B.4 in Appendix B shows the current voltage sensing circuit

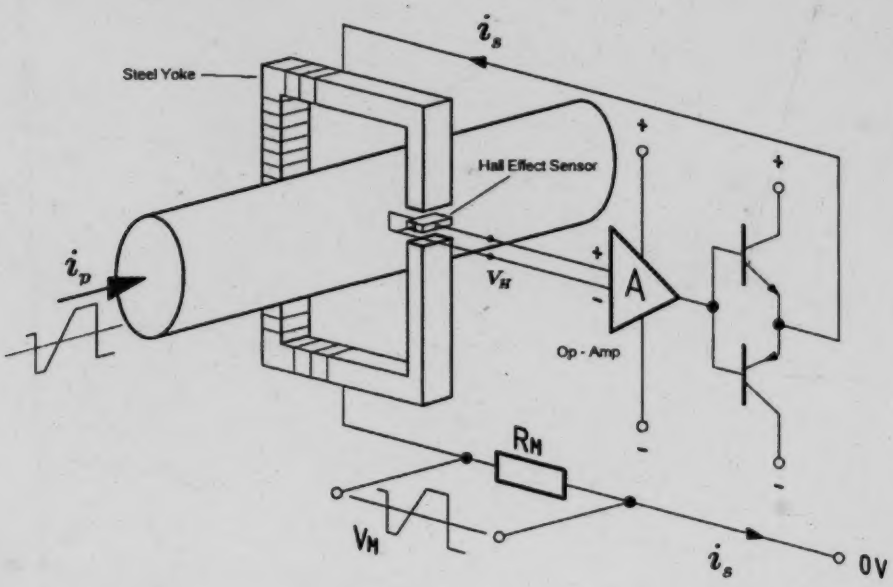

Figure 4.11: Schematic of hall-effect current sensor

onboard the power electronics.

4.3.4 Armature Displacement Sensor

Armature displacement measurements are conducted via a custom Eddy-Current type lift sensor with a high signal-to-noise ratio of more than 84 dB and a bandwidth greater than 20 kHz. It is reliable at a high temperature range and provides output voltages that are linearly scaled to the armature displacement. Circuit schematics pertaining to the eddy current type lift sensor circuitry is unavailable, however, its functionality is fundamentally similar to a basic eddy current displacement sensor. Figure 4.12 show the main components of this sensor.

Figure 4.12: Eddy current type lift sensor

It is important to note that armature velocities and accelerations are not measured but rather approximated by a standard Kalman filter and an exponentially moving average filter, respectively. The use of filter algorithms based on sampled low-noise position data are accurate and simple to implement in real-time. Appendix A provides further mathematical details related to these filters.

4.3.5 Power Electronics

Custom power electronics using standard H-Bridge circuit configurations were designed and built by Bazooka Electronics Ltd. (Figure 4.13). The power electronics provide three output modes (+ 42 V, 0 V and (quasi) -42 V) for regulating voltage to the actuator coils. Figure 4.14 schematically illustrates the power electronic circuit in all three modes.

All modes are achieved by switching two high speed voltage-controlled insulated gate bipolar transistors (IGBT IRG4BC40W) with control signals at a sample rate of 50 kHz. The PWM signals from the DS1103 controller board has a duty cycle of 50 kHz and triggers transistor T_1 while a digital TTL output signal triggers transistor T_2. Two flyback diodes, D_1 and D_2, are connected antiparallel to their respective transistors. At +42 V mode, both T_1 and T_2 are closed to allow current to flow from the power supply through the actuator. At 0 V mode, T_1 is opened while T_2 remains closed. This results in a net potential difference across the actuator of 0 VDC and current drops through diode, D1. In (quasi) -42 V mode, T_1 and T_2 are opened to drive current down so that the net potential difference across the actuator is -42 VDC. Certainly, a reverse polarity is only attainable when there is current flow, otherwise it is 0 VDC. This mode essentially switches the actuator off more rapidly than 0 V mode so that magnetic field, and hence, forces are reduced quickly. The arrows in Figure 4.14 represents realizable switch modes in a sequential order during operation. Because of the way the transistors are powered, T_1 is incapable of switching independently, the switch from +42V to (quasi) -42V mode is not feasible. T_2 must be closed in order to charge a subsidiary capacitor that provides power for T_1 to switch.

With sufficiently fast switching frequencies, it is reasonable to assume that PWM duty cycle variation regulates average linear voltage outputs effectively [Deng and

Figure 4.13: Power electronics

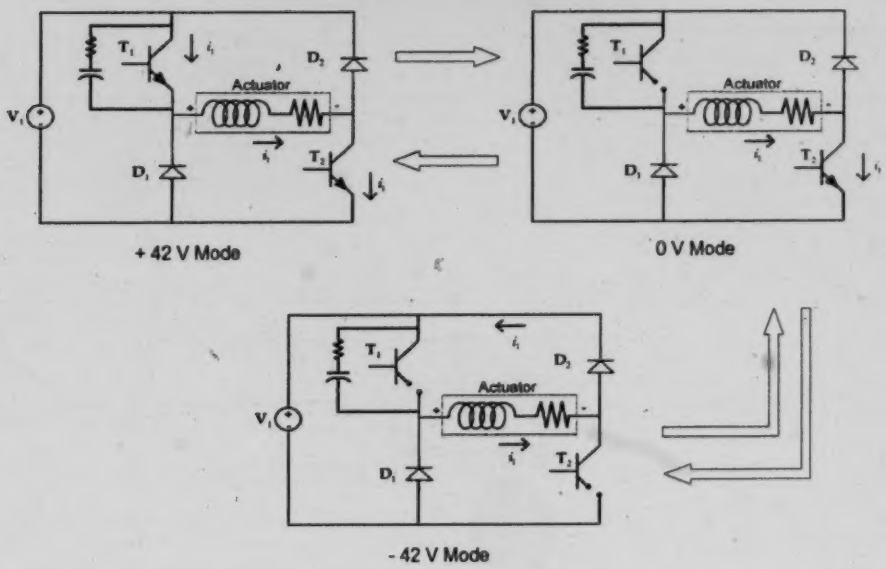

Figure 4.14: Power electronics output modes

Nehl, 1998, Pawlak and Nehl, 1988, Peterson and Stefanopoulou, 2004]. A pulse width modulated signal is an on/off signal in which the duty cycle of a PWM signal is the ratio of "on-time" divided by total time for one complete cycle, which in this case, it is 20 μs. Note: It is important that the "on-time" should not exceed the power dissipation limits of the coil to avoid coil overheating and irreversible damage to the coil.

4.4 Summary

The chapter provided a brief summary of hardware and softwares used to perform dynamic actuator experimental testing for control evaluation. The schematic in Figure 4.15 shows the interconnection of all the hardware components. Table 4.1 details the general specifications of the equipment used.

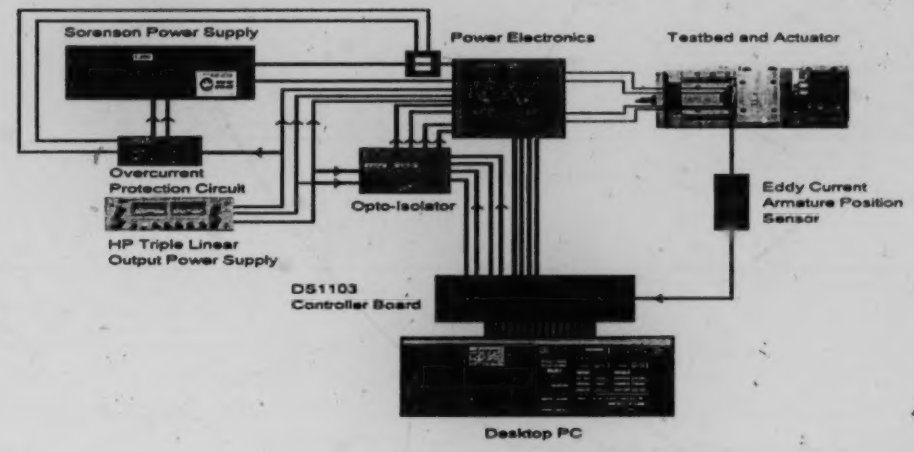

Figure 4.15: Experimental testbed setup schematic

Table 4.1: Relevant experimental equipment specifications

Unit Item	Description	Relevant Specifications
Prototype Actuator	TEMIC linear actuator donated by DaimlerChrysler AG.	8mm stroke
Host PC	Windows 2000 desktop computer for data collection, actuator control, simulation and model validation.	AMD Athlon XP 1800 1.53 GHz CPU 1 GB Ram
dSPACE Controller	DS1103 Controller Board Panel ControlDesk 2.4 PowerPC 604e Processor - 400 Mhz TMD320F240 Slave Processor - 20 MHz	16 Bit Sampling PWM and I/O signal output at 50 kHz
Actuator Power Supply	Sorenson DCS60-18E programmable switching power supply.	0-60VDC, 0-18A Input: 120 VAC Max. output: 1kW
Accessory Power Supply	Hewlett Packard 6236B triple output linear power supply.	+6VDC ± 20VDC
Power Electronics	Custom H-bridge driver for actuator control with on-board current-voltage sensor.	IGBT IRG4BC40W switching to 50kHz Cap: 200V @ 70A
Opto-Isolator	Provide linkage between DSll03 control board and power electronics with an optical gap. Variable overload protection.	10MBit/s ±15VDC Input
Overcurrent Protection Circuit	Shuts down Sorenson power supply in the case of power electronics error. Actuator coil burn-out protection.	+5VDC Input
Eddy Current Type Lift Sensor	Armature displacement sensor.	Bandwidth $\geq$ 20kHz High signal-to-noise ratio $\geq$ 84dB

Chapter 5

Results and Discussion

This chapter summarizes and discusses results obtained during simulation and experimental investigation for a prototype gas exchange solenoid actuator donated by DaimlerChrysler AG. Flatness-based voltage end-control is evaluated based on maintaining low impact armature velocities of ≤ 0.1 m/s. In addition, a classical Proportional-Integral (PI) current end controller is implemented and compared to the proposed control scheme.

5.1 Simulink Model of an EMV Actuator

A lumped parameter model has been formulated in Matlab's Simulink environment to simulate dynamic electromechanical actuator behavior with flatness-based end-control. The main objective is to verify the end controller's capability in tracking the armature to its reference so that the seating velocity is less than 0.1 m/s. Mathematical representations that were derived in Chapter 3 are incorporated into the model to obtain expedited solutions with sufficient accuracy. Since only the end-control is studied, the model does not include an approach control strategy but rather assumes that it has delivered the armature states to near desired conditions (defined in Section 3.7) and is then disabled. At which point, the flatness-based end controller is enabled. Figure 5.1 shows a schematic of the control structure for flatness-based end-

control. Since the initial desired armature position is $y_d(t_0) = 2.55$ mm, the model will conduct simulation for the last 1.45 mm portion of the entire 8.00 mm armature motion without considering external disturbances.

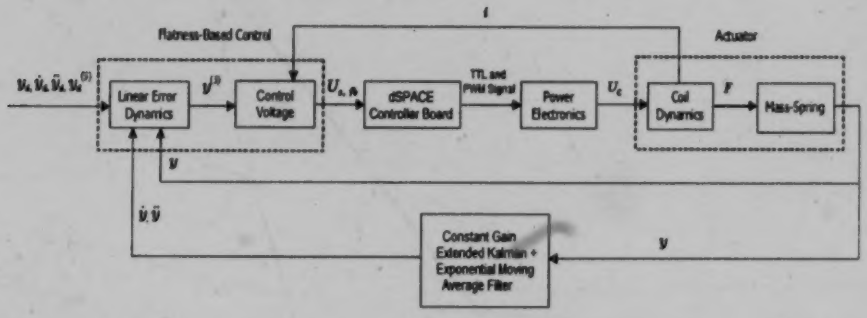

Figure 5.1: Scheme of flatness-based voltage end-control with estimation of state variables

Referring to the model in Figure 5.1, armature positions are approximated with Equations (3.1) and (3.6) using mass-spring properties estimated by system identification methods in Section 3.6. Coil dynamic behavior are predicted with Equations (3.8), (3.9) and (3.10) to generate current and magnetic force information. For flatness-based end-control, Equations (3.24) and (3.25) are utilized to ensure stable tracking linear error dynamics are achieved by calculating desired control voltage inputs which is now denoted as $U_{c,fb}$. In turn, $U_{c,fb}$ signals are converted by a DS1103 controller board model to output TTL/PWM signals. These signals are required for triggering power electronic transistors that provide operative switch modes of +42 V, 0 V and (quasi) -42 V.

The augmentation of a simple power electronics model developed by [Chladny et al., 2005] using Matlab-Simulink's SimPower toolbox improves simulation accuracy for coil voltage transients, U_c. As shown in Figure 5.2, it parameterizes circuital properties according to manufacturer's specifications. An example of expected voltage transients when subjected to various switch modes is shown in Figure 5.3, demon-

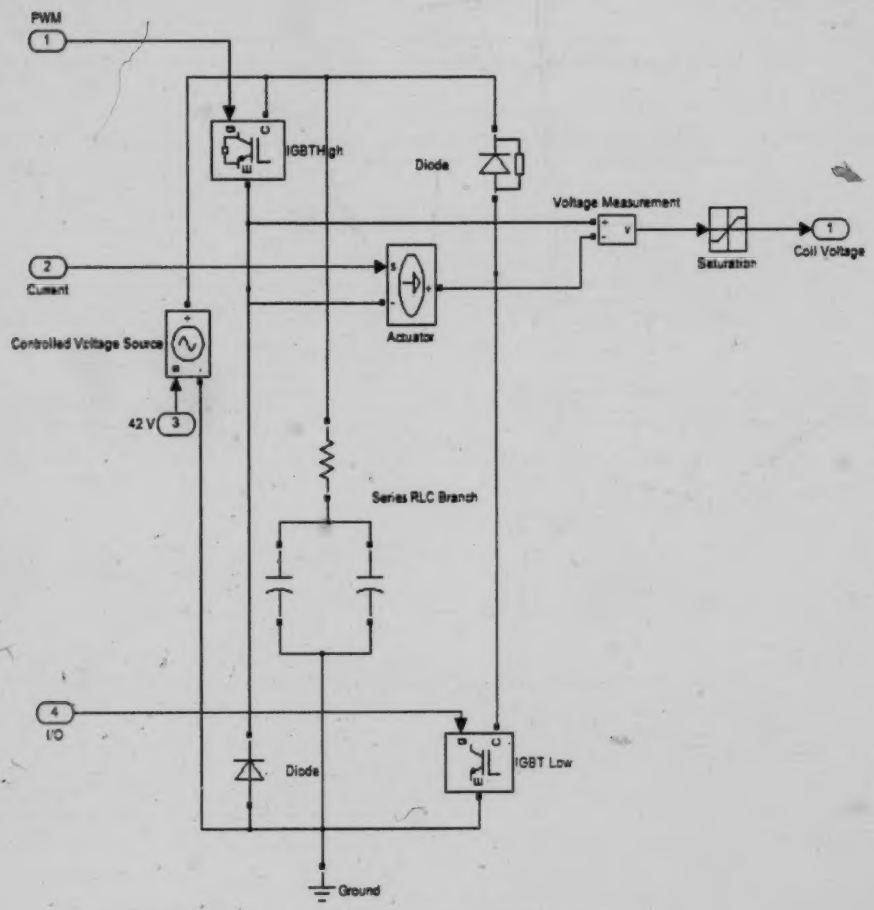

Figure 5.2: Simulink power electronics model [Ryan Chladny - personal communication]

strating comparable results between measured and simulated coil voltages. Minor differences are due to the assumption in the model that all circuitry components and voltage supply are ideal [Chladny et al., 2005].

The filter algorithms used in RTI to estimate armature velocity and acceleration

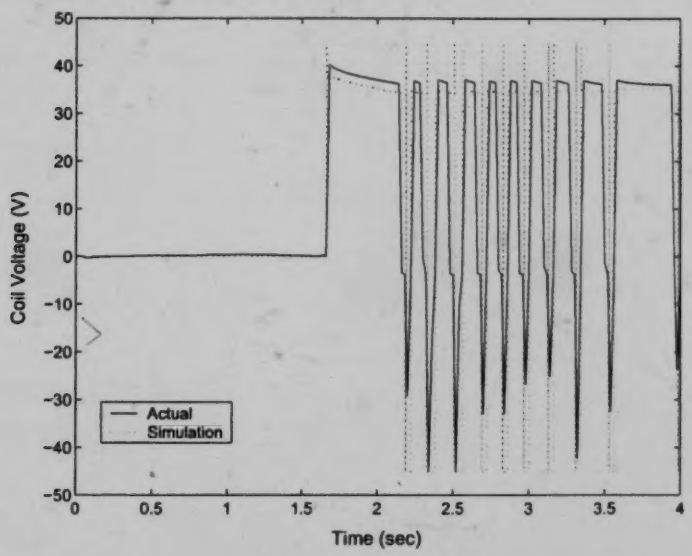

Figure 5.3: Actual and simulated power electronics output voltages

are also implemented in the Simulink model. Since velocity and acceleration states are not measured during RTI applications, the position measurements are passed into a constant gain extended Kalman filter and a exponential moving average filter to estimate velocity and acceleration, respectively. Further details regarding both filters can be referred to Appendix A.

5.2 Simulation Results

5.2.1 Simulation Case 1

A situation where the initial armature position $y(t_0) = 2.53$ mm , armature velocity $\dot{y}(t_0) = 2.58$ m/s and coil current $i_c(t_0) = 8.90$ A is considered for simulating flatness-based end-control. These assumed state conditions are practical and realistic under normal experimental conditions. Due to a variety of reasons, the approach control

scheme will not deliver the actual system states to the exact desired conditions defined in Section 3.7. Pole locations in the complex s-plane are selected for Equation (3.24) to ensure fast convergence of the actual trajectory to the desired trajectory is achieved within the time interval $t_f - t_0 = 1.84 \times 10^{-3}$ s. This results in linear error dynamic controller gains k_0, k_1 and k_2 to be 8.00×10^{12} s^{-3}, 1.02×10^{9} s^{-2} and 6.00×10^{4} s^{-1}, respectively.

The integration method in Simulink uses an adaptive step size ode15s (stiff/NDF) solver with a relative error tolerance of 0.90 percent. Figures 5.4 to 5.7 shows comparison of the reference and simulated armature trajectories. In Figure 5.4, the flatness-based end-control demonstrates convergence of the armature position to its reference trajectory. Figure 5.5 exhibits armature velocity is limited to 0.10 m/s although the armature seems to have made earlier contact with the coil than the reference. This minor discrepancy is perhaps due to the use of a Kalman filter in the model to predict armature velocities. Impact dynamics are not included in the plant, and therefore, velocity predictions do not show bounce effects after contact has been established. Figure 5.6 displays acceleration converges to zero at impact in spite of using an exponential moving average filter for approximating $\ddot{y}(t)$. Coil current dynamics are illustrated in Figure 5.7 indicating slightly higher simulated current levels required to track the reference trajectory. The effects of eddy current shown in Figure 5.8 are reasonable and expected for an approaching armature that induces opposing flux caused by increasing/decreasing transient coil currents and armature motion. Figure 5.9 shows simulated voltage levels remain within ± 42 V constraints while achieving the desired performance.

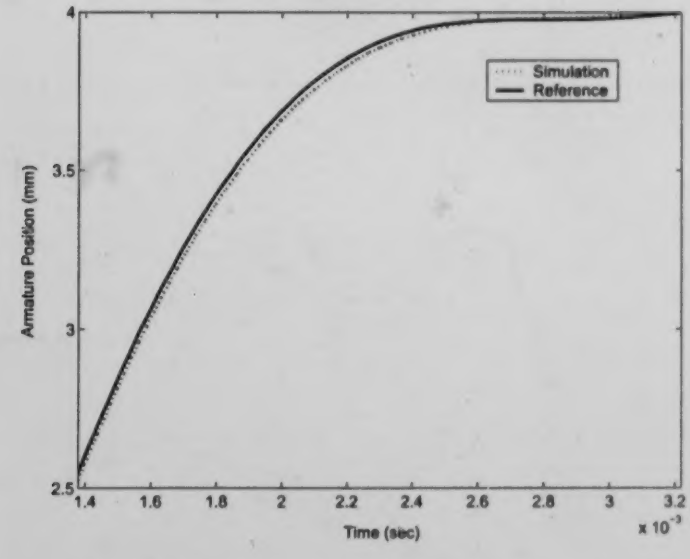

Figure 5.4: Desired and simulated armature position

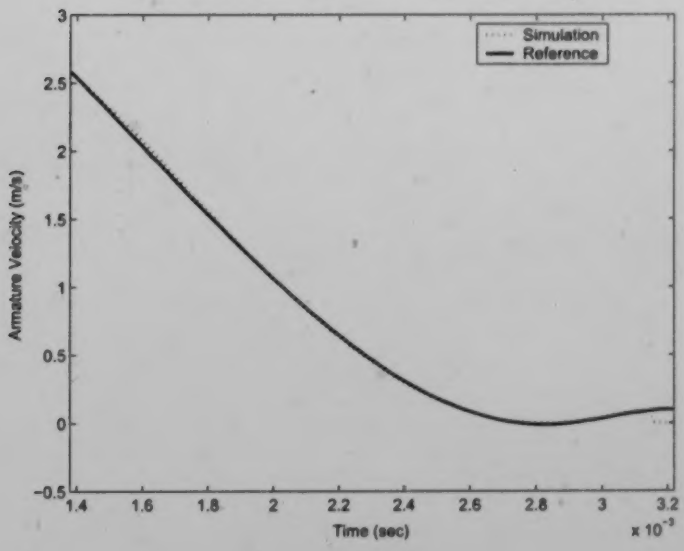

Figure 5.5: Desired and simulated armature velocity

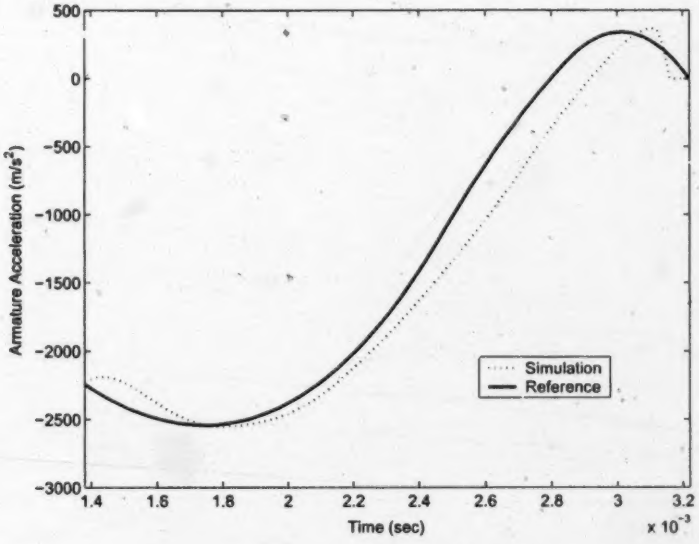

Figure 5.6: Desired and simulated armature acceleration

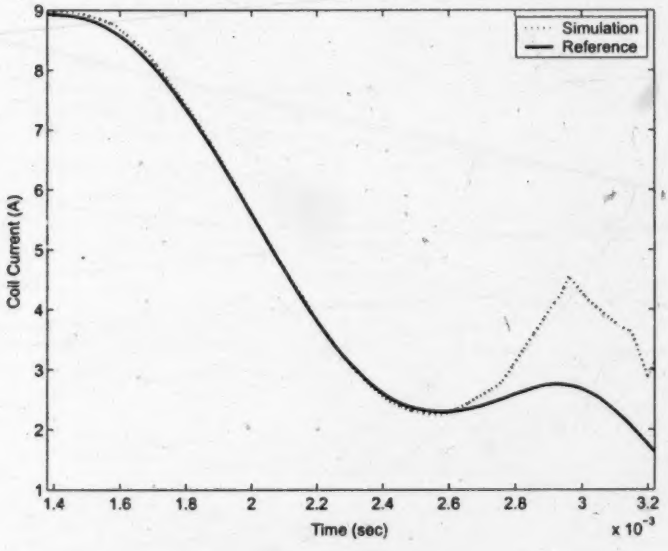

Figure 5.7: Desired and simulated coil current

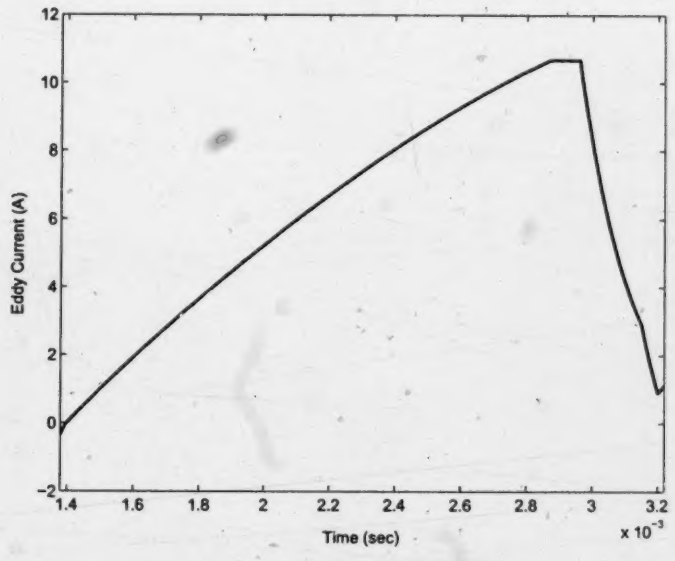

Figure 5.8: Simulated eddy currents

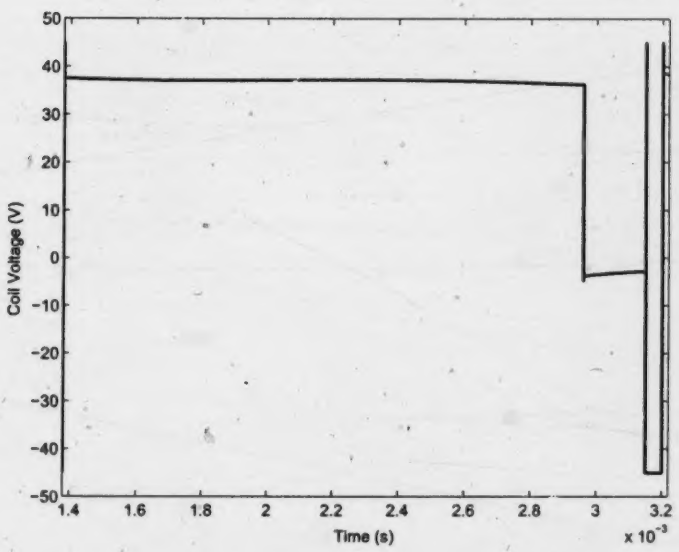

Figure 5.9: Simulated coil voltage input

5.2.2 Simulation - Sensitivity to Initial Position and Velocity Conditions

In the previous section, flatness-based end-control is able to follow a trajectory for a defined transient time when starting state conditions are within a small tolerance to the desired states. However, there are probable circumstances where the approach control's influence during real-time experimentation may result to larger deviations in initial state conditions. For this reason, it is worthwhile to evaluate the end-control's response to such situations in fulfilling the targeted trajectory. The information obtained would provide a gauge in tuning the real-time approach scheme so that desirable results are realized by the end controller. This section will consider the following cases for simulation.

$$\text{Case 2} \rightarrow y(t_0) = 2.51 \text{ mm and } \dot{y}(t_0) = 2.59 \text{ m/s}$$

$$\text{Case 3} \rightarrow y(t_0) = 2.56 \text{ mm and } \dot{y}(t_0) = 2.57 \text{ m/s}$$

The time interval and controller gains are chosen to be the same as in the previous section. Note also that the coil current is preset to $i_c(t_0) = 8.90$ A for these simulation cases.

Figures 5.10 to 5.12 illustrate how flatness-based end-control fared in tracking the desired trajectory for both cases. In Case 2, the control inputs shown in Figures 5.13 to 5.15 resulted to an impact velocity of 0.17 m/s. This is can be explained by the requirement of having the end-control, which started at $y(t_0) = 2.51$ mm, to remain at +42 V (Figure 5.15) for a longer period of time to ensure armature landing. By the time compensations are made for a fast approaching armature, the armature is too close to the coil for any significant manipulation. Even if evaluations are performed for lower $\dot{y}(t_0)$ while $y(t_0)$ remained the same, the end results (although not shown here) are unsatisfactory that either led to a higher impact or not landing at all.

In Case 3, flatness-based end-control is enabled when the armature position overshoots the reference slightly at a lower velocity. By starting at $y(t_0) = 2.56$ mm, control efforts are forced to turn off momentarily (Figures 5.13 to 5.15) until the armature motion is below its reference. Even though +42 V is injected into the system for the remaining course, the system is unable to recover sufficient energy to pull the armature in within the short time period. The same responses (not shown here) are also achieved when simulations are performed for a higher $\dot{y}(t_0)$ at $y(t_0) = 2.56$ mm. Based on Case 2 and 3 results, the success of flatness-based end-control is dependent on initial state conditions. The controller gains may have been varied for these cases, however, flatness-based end-control is not as susceptible to gain variations than it is to starting state conditions. These plots indicate how difficult it is to implement landing control for this actuator. The difficulty is mainly due to the inherent slow response of current (and force) to a change in the input voltage. This response speed decreases with decreasing air gap, and in turn, exacerbates the control problem. Therefore, when tuning the real-time approach control scheme, effort should be made in ensuring initial state conditions are close to the reference.

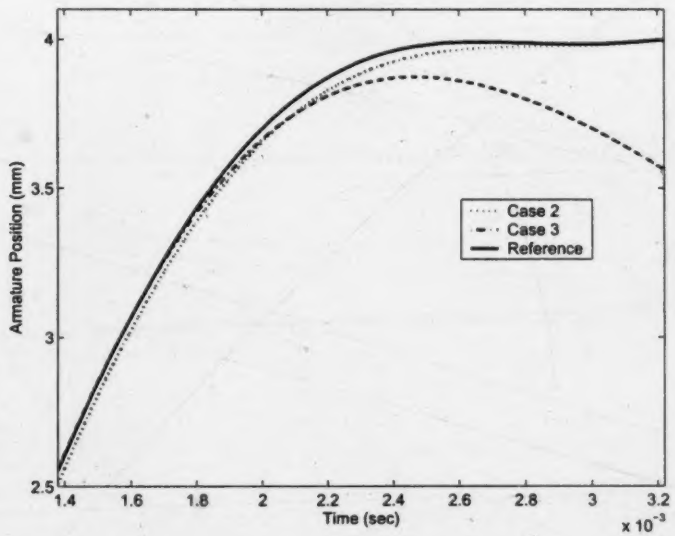

Figure 5.10: Desired and simulated armature position (Case 2 and 3)

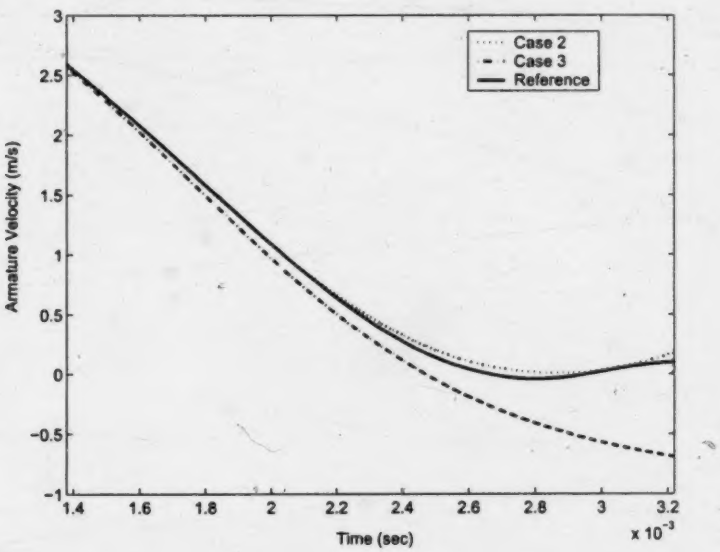

Figure 5.11: Desired and simulated armature velocity (Case 2 and 3)

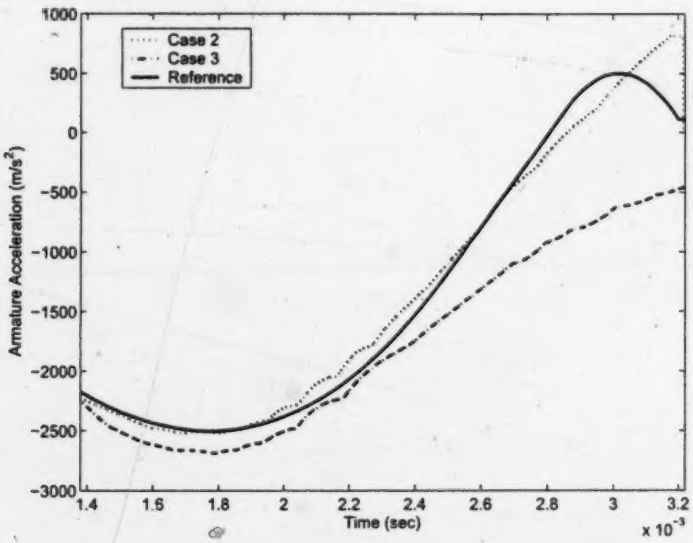

Figure 5.12: Desired and simulated armature acceleration (Case 2 and 3)

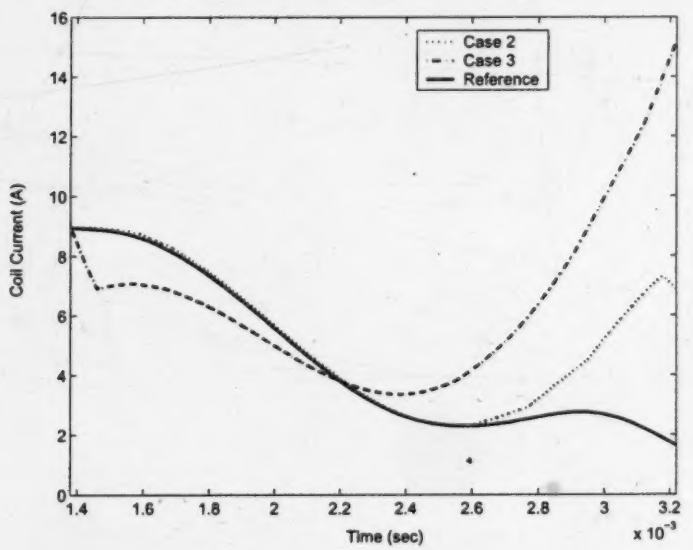

Figure 5.13: Desired and simulated coil current (Case 2 and 3)

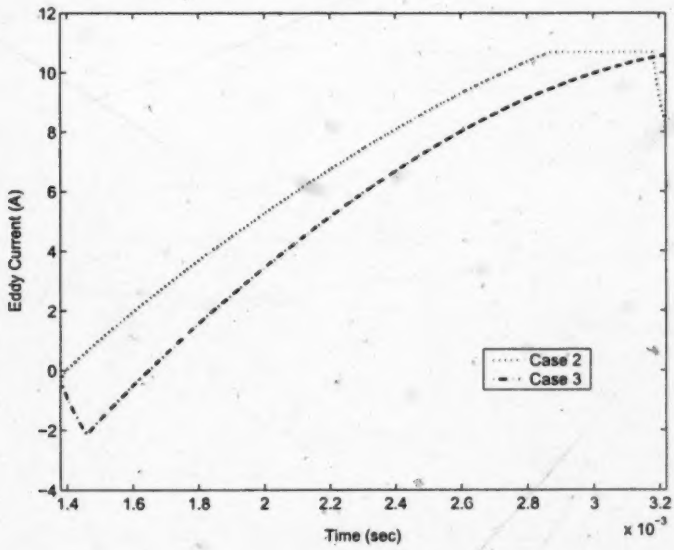

Figure 5.14: Simulated eddy currents (Case 2 and 3)

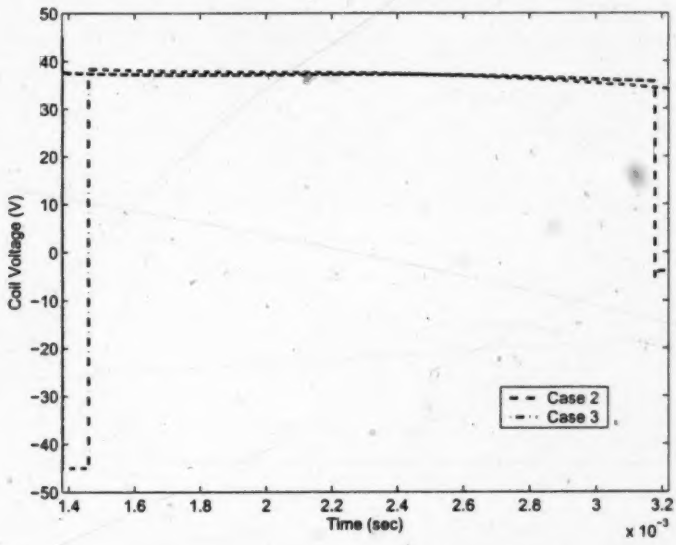

Figure 5.15: Simulated coil voltage input (Case 2 and 3)

5.3 Experimental Implementation

Flatness-based and PI end-control have been implemented on the testbed using a dSPACE system. The primary emphasis is to seat the armature softly in which these proposed schemes are executed during the final part of armature motion. The next two subsections briefly discuss control features implemented in real-time.

5.3.1 Flatness-Based Voltage End-Control

The control algorithm for flatness-based end-control is implemented in C language which is executed at a sample rate of 50 kHz on the DS1103 controller board. This end controller is combined with an open-loop current scheme as well as a hold mode to traverse the armature from one end of the coil to another during real-time implementations (RTI). A flow chart outlining the structure of control events is shown in Figure 5.16.

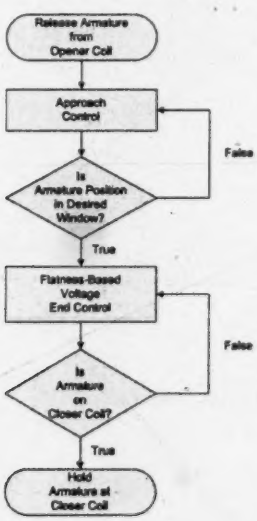

Figure 5.16: Control algorithm for flatness-based voltage end-control

In addition to C code control development, lookup tables based on y_d, $\dot{y}_d$, $\ddot{y}_d$ and $y_d^{(3)}$

profiles in Section 3.7 are formed. These desired trajectories data are tagged with numerical index values at intervals of 20 μs, for cross-referencing linear error dynamic calculations. Instead of $y = x \in$ [-4, 4] mm defined in Section 3.1, the armature coordinates are modified to $y = x \in$ [-8, 0] mm where the closed and open positions are defined as 0 mm and -8 mm, respectively. Figure 5.17 shows parameter input values entered into respective virtual instrument panels developed in ControlDesk for the approach (or open-loop) current control, flatness-based end-control and holding current control.

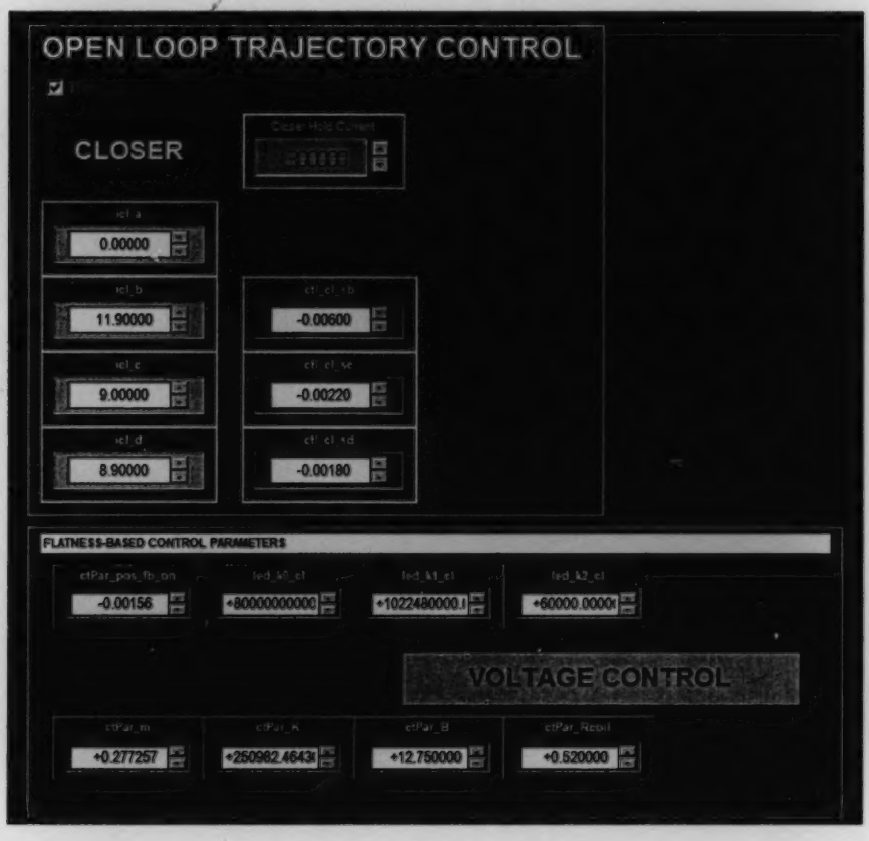

Figure 5.17: Approach control and flatness-based end-control parameter inputs in ControlDesk

In the approach control scheme, various current levels are set at different armature positions to deliver the armature states as close to the desired initial conditions (described in Section 3.7) as possible. By setting the following,

$$y \text{ (ctl_cl_sb)} \geq -0.0060 \text{ m} \longrightarrow \text{icl_b} = 11.9 \text{ A (Constant)}$$
$$y \text{ (ctl_cl_sc)} \geq -0.0022 \text{ m} \longrightarrow \text{icl_c} = 9.0 \text{ A (Negative Ramp)}$$
$$y \text{ (ctl_cl_sd)} \geq -0.0018 \text{ m} \longrightarrow \text{icl_d} = 8.9 \text{ A (Constant)}$$

actual armature states approach with $y = 2.525$ mm and $\dot{y} = 2.580$ m/s when flatness-based end-control is enabled. These states are, in fact, similar to the assumed initial conditions previously considered for simulation in Section 5.2.1 with a difference of 0.2 % in y and 0.01 % in $\dot{y}$. The parameter ctPar_pos_fb_on shown in Figure 5.17 initialize flatness-based control voltage calculations. When the real-time dSPACE controller registers $y \geq -1.56 \times 10^{-3}$ m (or $y \leq 2.44$ mm), $U_{c,fb}$ values are calculated one time step later (i.e. 20 μs) beginning at $y = 2.525$ mm and $\dot{y} = 2.580$ m/s. System parameters ctPar_m, ctPar_K, ctPar_B and ctPar_Rcoil defined in Section 3.6 are used for flatness-based voltage input computations. Similarly, linear error dynamic gains described in Section 5.2 are used with led_k0_cl, led_k1_cl and led_k2_cl set to 8.00×10^{12} s^{-3} and 1.02×10^{9} s^{-2} and 6.00×10^{4} s^{-1}, respectively. When armature contact is established and quasi-static conditions are reached, a holding current of 3 A is applied to the closer coil to hold the armature.

5.3.2 Proportional-Integral Current End-Control

A PI controller is implemented experimentally for comparison with the proposed flatness-based end-control. It functions strictly as an end controller and manipulates current input based on deviations from the closed position. Hence, closed-loop control

has the following expression

$$i_{pi} = K_p[y - y_s] + K_i \int_0^t [y - y_s](\tau)\, d\tau \tag{5.1}$$

where y_s is the end position of the closer coil, i_{pi} is the current control input, K_p is the proportional gain and K_i is the integral gain. A block diagram for the PI end-control structure is shown in Figure 5.18

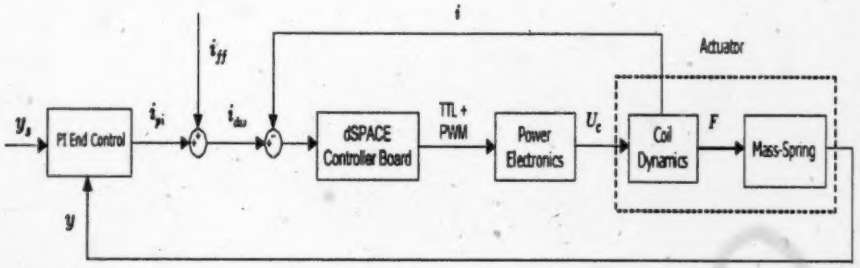

Figure 5.18: Scheme of proportion-integral current end-control for real-time implementation

Likewise, control algorithms pertaining to PI end-control are coded in C language for real-time testing. The approach scheme, denoted here as i_{ff}, is specifically tuned differently for this controller in order to achieve the desired end conditions. Figure 5.19 shows the respective variable inputs entered into ControlDesk with PI end-control enabled at y (s_cl_pi) $\geq -1.70 \times 10^{-3}$ m. Proportion, K_p (kp_pi_cl) $= 2.50 \times 10^3$ A/m, and integral, K_i (ki_pi_cl) $= 3.50 \times 10^2$ A/m^2, gains are used to achieve system stability and low impact velocity.

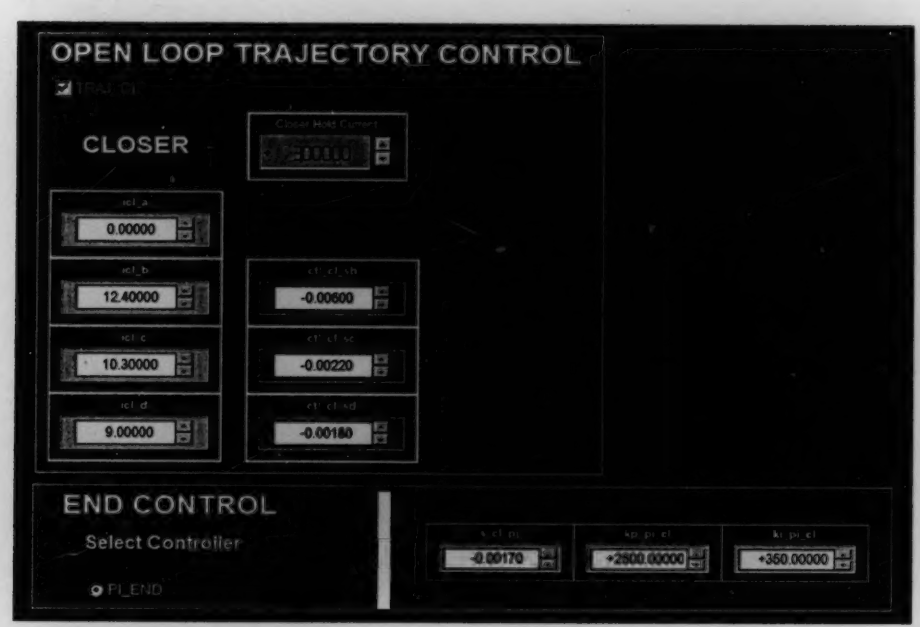

Figure 5.19: Approach control and proportional-integral end-control parameter inputs in ControlDesk

5.4 Experimental Results

Figures 5.20 to 5.24 shows experimental results obtained for both flatness-based and PI end-control schemes. Even though each approach control scheme and window of control initiation is defined differently, a comparison can still be made with respect to impact velocity. In addition to these plots, simulation results from Section 5.2 are plotted to verify the plant model.

Convergence of the actual armature position as a result of flatness-based end-control is demonstrated in Figure 5.20 with minor discrepancy to simulated position responses (maximum error = 3.84%). As well, PI end-control exhibits convergence to the closed position despite different armature path and control conditions. The discrepancy is more apparent in Figure 5.21 where flatness-based end-control's actual impact occurs earlier than desired with a greater velocity of 0.11 m/s as opposed to its

reference landing velocity of 0.10 m/s. This result is still relatively good considering the difficulty involved in controlling such devices and how real-time control voltage inputs calculations may have been affected by unmodeled parameters uncertainties and disturbances. Figure 5.21 also illustrate apparent bounce effects for experimental results. Usually, after-impact velocities are low and tends to settle quickly for the holding part in Figure 5.16 to be initiated. Experimental results confirm that as long as this impact condition is satisfied, bounce dynamics should be minimal. Armature velocity due to PI end-control, on the other hand, contacts the coil at 0.12 m/s. The higher impact is directly related to higher current levels, as shown in Figure 5.23, to induce greater magnetic force on the closer coil so that the armature would land successfully. When too much current has been injected into the system, compensations made by PI end-control to reduce current levels are not fast enough to reduce the armature incoming speed. Hence, this results in the armature landing slightly harder and earlier than flatness-based control.

Similar trends are shown for actual and simulated acceleration in Figure 5.22 with flatness-based end-control matching the simulation closely. Despite minor differences, the lumped parameter simulation model provides fast and sufficiently accurate solutions without having to consider disturbances and uncertainties such as armature deformation, stiction, nonlinear damping/spring constant as well as other time varying parameters. Errors associated in parameterizing variables for Equations (3.3) and (3.1) are expected in this modeling process. Indeed, armature velocity and acceleration approximated from low noise position measurements using Kalman and exponential moving average filter algorithms would also contribute discrepancies in experimental results. In Figure 5.23, actual and simulated current levels for flatness-based end-control are in good agreement. Given the complexities of accurately modeling eddy current effects and power electronic circuital properties, the simulation model is valid, and consequently, it can be used to design new control algorithms.

Actual voltage levels are shown to be within ±42 V in Figure 5.24. All voltage polarity schemes are similar, in particular, simulation and actual signals pertaining to flatness-based end-control. When $t \leq 2.85$ μs, +42 V is enabled to pull the armature in. Beyond this time (or $t > 2.85$ μs), control efforts by flatness-based and PI end-control differ in the attempt to reduce magnetic force imparted onto a fast approaching armature.

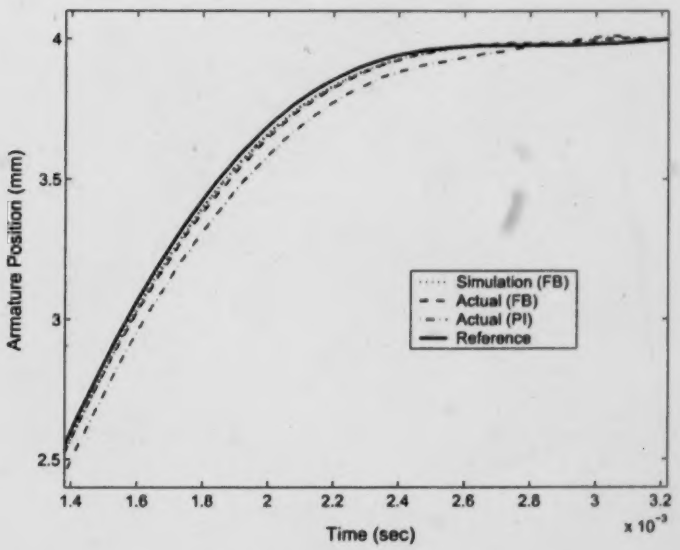

Figure 5.20: Desired, simulated and experimental results for armature position

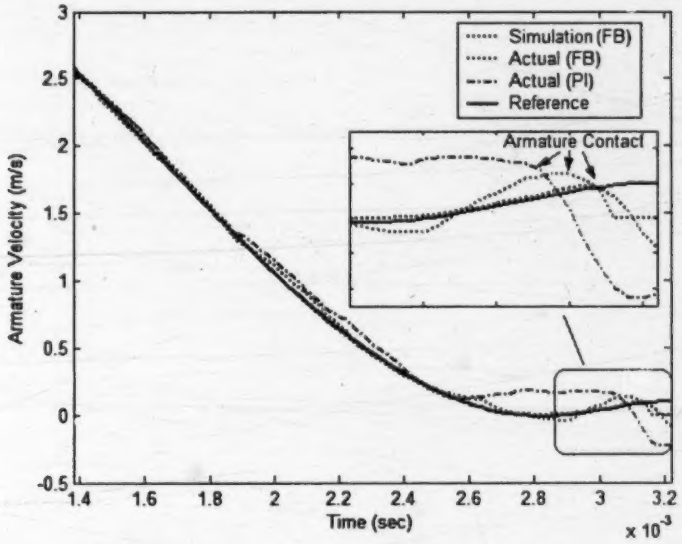

Figure 5.21: Desired, simulated and experimental results for armature velocity

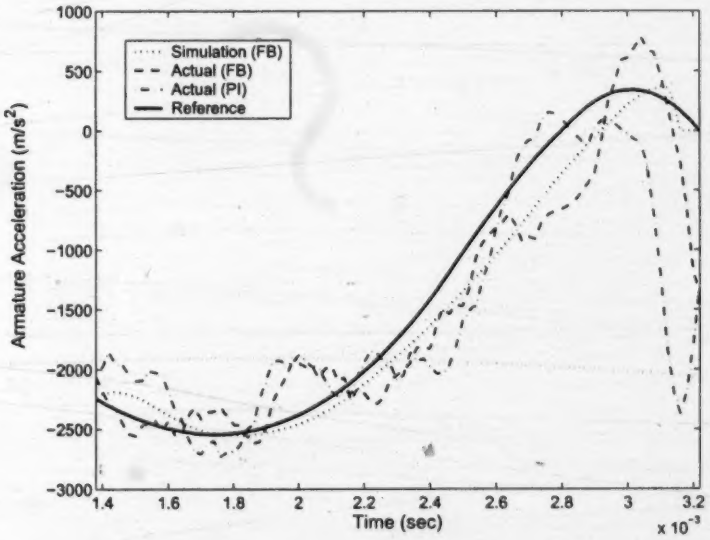

Figure 5.22: Desired, simulated and experimental results for armature acceleration

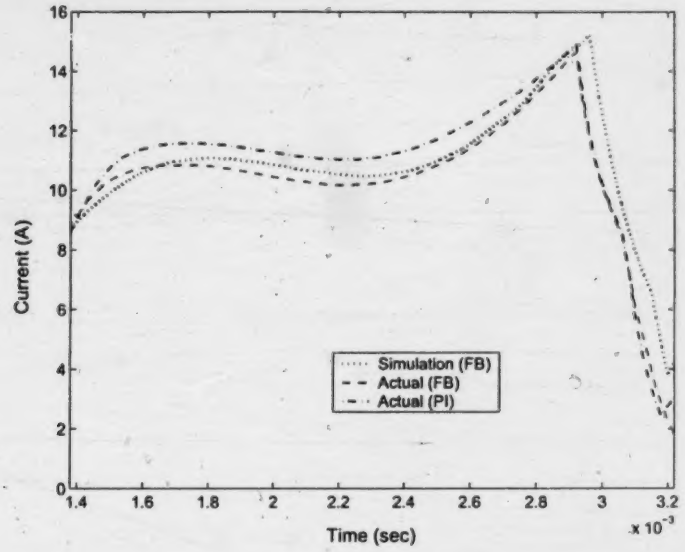

Figure 5.23: Simulated and experimental results for current

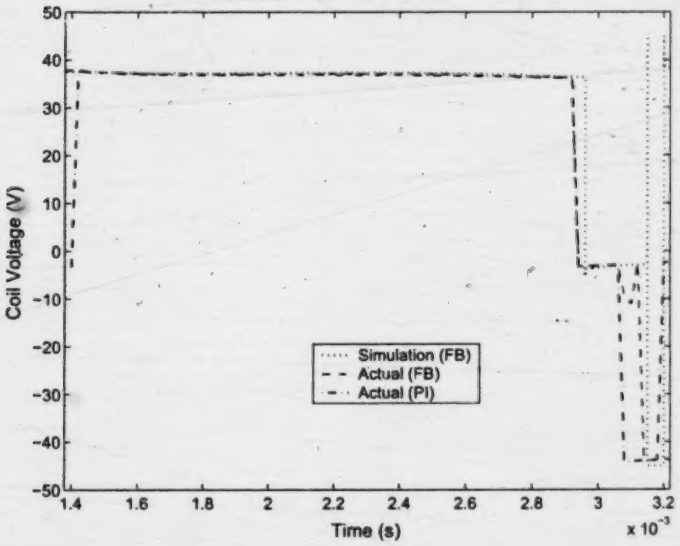

Figure 5.24: Simulated and experimental results for coil voltage

Repeatability tests are conducted for flatness-based end-control to verify its consistency in maintaining low impact velocity. The tuned approach control scheme in Figure 5.17 is combined with the end controller for a 50 cycle test run. Even when initial armature states varied slightly from one cycle to another, the proposed end-control scheme was consistent in landing the armature as shown in Figure 5.25. A statistical analysis in Figure 5.26 shows the distribution of armature impact velocities to have an average velocity of 0.097 m/s with a standard deviation of 0.028 m/s.

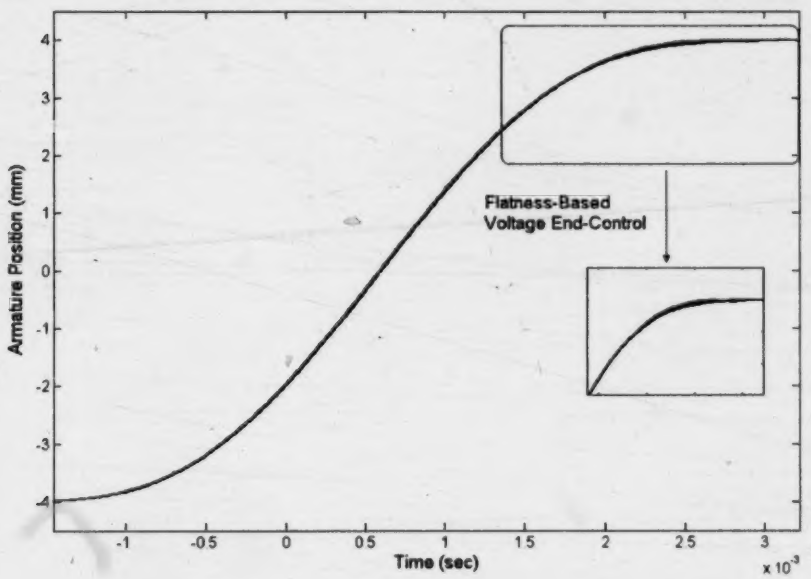

Figure 5.25: 50 cycles of experimental armature position data for flatness-based voltage end-control

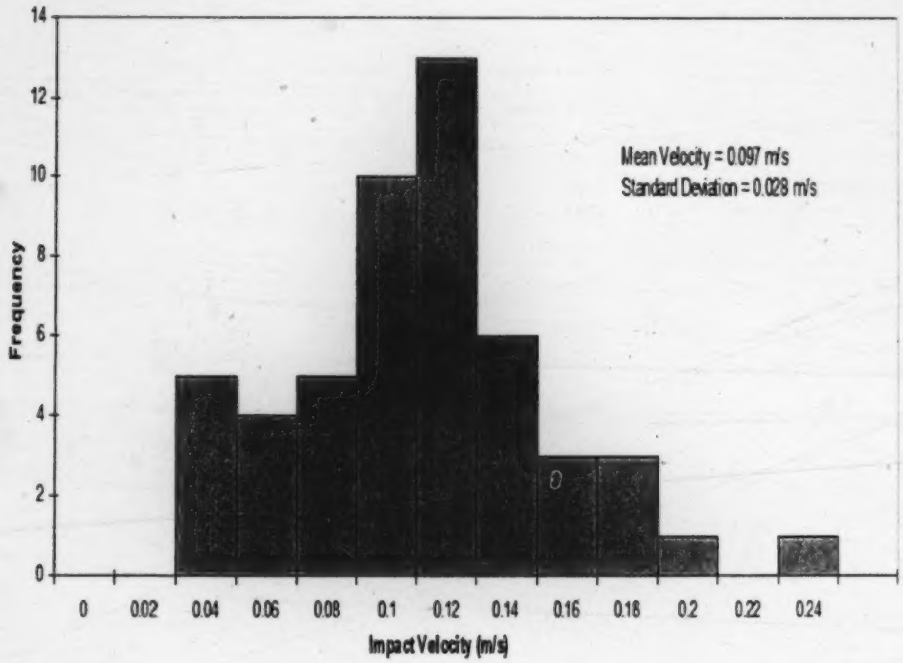

Figure 5.26: Distribution of armature impact velocity for 50 cycles using flatness-based voltage end-control

A similar test cycle using PI end-control is conducted for comparison purposes. Figure 5.27 shows the distribution of armature impact velocities with a slightly higher average velocity of 0.12 m/s and standard deviation of 0.045 m/s than flatness-based end-control. The results illustrate that flatness-based end-control is fairly robust as long as initial state conditions and system parameter variations are small. Furthermore, it is enabled at a later phase than PI end-control (i.e. when the armature is closer to the coil) and, thereby, requires less feedback control effort.

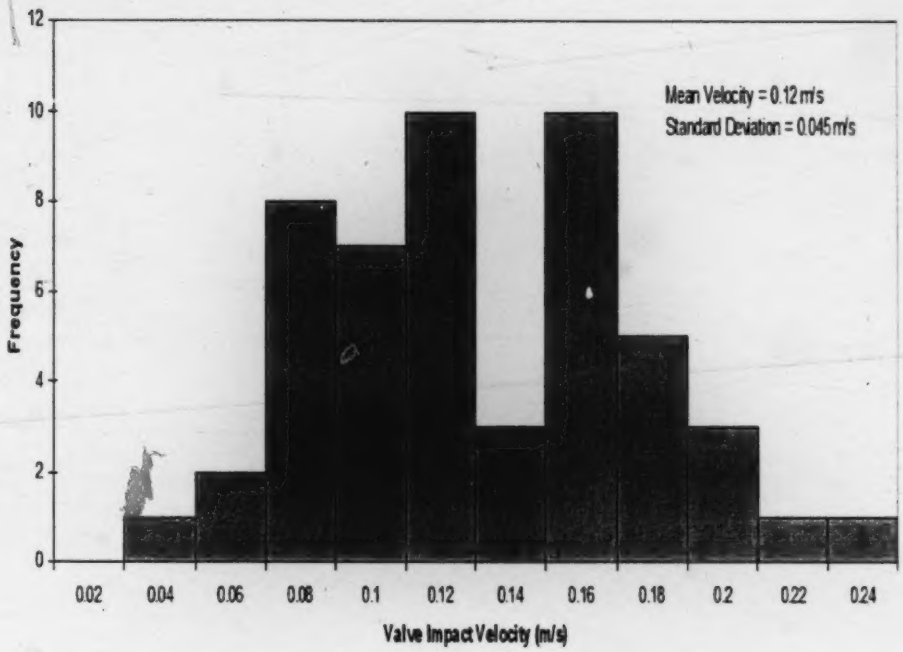

Figure 5.27: Distribution of armature impact velocity for 50 cycles using proportional-integral current end-control

5.5 Summary

Flatness-based voltage end-control is demonstrated in simulation and validated experimentally. The flatness-based end-control scheme on the actuator testbed achieves the design objectives of an impact velocity of less than 0.10 m/s while maintaining voltage levels within ±42 V. Agreement between simulated and actual armature responses indicate good model fidelity for the simulation model without excessive computation. Thus, this model is useful for control development. Although small discrepancies are apparent, these differences are normally expected due to the tradeoff between model complexity and model accuracy. In conducting a test run of 50 cycles, flatness-based end-control is capable of maintaining low impacts granted adaptive approach control is unavailable. PI end-control, on the other hand, produced slightly higher average velocity of 0.12 m/s and standard deviations of 0.045 m/s for a 50 test cycle.

Chapter 6

Conclusions and Further Research

The nonlinear dynamics of solenoid actuators and stringent performance has made its modeling and control design a challenging problem. In this dissertation, a closed-loop end-control solution is proposed and achieves soft seating operations of 0.1 m/s with a voltage supply of 42 V. Based on the simulation and experimental results, the following concluding remarks can be made:

1. A relatively simple and accurate EMV model is developed for control development and evaluation. The simulation model takes eddy current effects, magnetic saturation, power electronics and filter algorithms into account to improve transient behavior approximations.

2. Physical parameters pertaining to electrical and mechanical dynamics in the model are determined with system identification and least-square curve fitting techniques. These procedures are based on FEA $\lambda(x, i_c)$ and experimental force data obtained from an actual prototype actuator.

3. Flatness-based voltage end-control is developed for the solenoid actuator to ensure the armature converges exponentially to a desired trajectory. Here, the flat output of the flat system is parameterized with B-spline basis functions using nonlinear programming to obtain a feasible open-loop control input. The

design procedure considers the final portion of armature travel and incorporates Lambert W function, eddy current and saturation effects, a number of motion constraints, and voltage limitations.

4. A feedback control scheme is used in conjunction with the flatness-based open loop trajectory to achieve the desired dynamic performance.

5. The developed simulation model is validated and accurately predicts actuator dynamics. For example, in the case Section 5.2.1, the simulated results are comparable to the experimental results with a maximum position and velocity errors of approximately 3.8% and 10.0%, respectively. Thus, the simulation model is useful for developing new control algorithms.

6. The desired performance constraints are achieved by flatness-based voltage end-control on the experimental testbed with impact velocities averaging at 0.097 m/s and a standard deviation of 0.028 m/s for a 50 cycle test run. The PI current end-control resulted in an average velocity of 0.12 m/s and a standard deviation of 0.045 m/s. The flatness-based end-control showed better performance than the PI end-control and also showed that flatness-based end-control requires less control effort as it is enabled at later stage when the armature is closer to the coil.

7. The flatness-based end controller is sensitive to initial armature conditions. To ensure the armature lands properly, the end controller should be enabled at state conditions that are within a certain tolerance from initial desired reference values.

6.1 Further Research

Future research could be concentrated in the following areas:

1. To simulate varying gas exchange pressure disturbances of a real engine, experimental tests could be conducted on the testbed with an air pressure cavity.

2. Control up to the end-control should be implemented. One possible method is a scheme that utilizes recursive parameter estimation to influence armature motion at large air gaps.

3. To characterize the valve actuator in an engine more accurately, the simulation model could be extended to include a hydraulic lash adjuster.

4. The end-control developed here needs to be tested on a single cylinder engine and the control algorithm can be tested for various combustion types such as homogeneous charge compression ignition (HCCI).

5. The simulation model developed here can be used to explore new control strategies.

6. Apply and extend flatness-based control to a hinged actuator described in [Chladny, 2003].

BIBLIOGRAPHY

Ahmad, T. and Theobold, M. A. (1989). A survey of variable-valve-actuation technology. *SAE*, 891674.

Birch, S. (2000). Renault Research. *Automotive Engineering International Online.*

Boor, C. D. (1978). *A Practical Guide to Splines.* Springer-Verlag, New York.

Brauer, J. R. and Chen, Q. M. (2000). Alternative dynamic electromechanical models of magnetic actuators containing eddy currents. *IEEE Transactions on Magnetics*, 36(4):1333–1336.

Brüstle, C. and Schwarzental, D. (2001). VarioCam Plus - A highlight of the Porsche 911 turbo engine. *SAE*, 2001-01-0245.

Butzmann, R., Melbert, J., and Koch, A. (2000). Sensorless control of electromagnetic actuators for variable valve train. *SAE*, 2000-01-1225.

Byrd, R. H., Schnabel, R. B., and Shultz, G. A. (1988). Approximate solution of the trust region problem by minimization over two-dimensional subspaces. *Mathematical Programming*, 40:247–263.

Chang, W. S., Parlikar, T. A., Seeman, M. D., Perreault, D. J., Kassakian, J. G., and Keim, T. A. (October 2002). A new electromagnetic valve actuator. *IEEE Workshop on Power Electronics in Transportation, Auburn Hills, MI*, pages 109–118.

Chladny, R. (2003). Modeling and simulation of automotive gas exchange valve solenoid actuators. Master's thesis, University of Alberta.

Chladny, R. R., Koch, C. R., and Lynch, A. F. (2005). Modeling of automotive gas exchange solenoid valve actuators. *IEEE Transactions on Magnetics*, 41(3):1155–1162.

Chui, C. K. and Chen, G. (1991). *Kalman Filtering with Real-Time Applications, 2nd Edition*. Springer-Verlag, Berlin, New York.

Chung, S. K. (2002). Full state feedback control for electromagnetic solenoid valve actuator. *EE660 Term Report, Department of Electrical Engineering, University of Alberta*.

Corless, R., Gonnet, G., Hare, D., Jeffrey, D., and Knuth, D. (1996). On the Lambert W function. *Advances in Computational Mathematics*, 5:329–359.

Deng, F. and Nehl, T. W. (1998). Analytical modeling of eddy-current losses caused by pulse-width-modulation switching in permanent-magnet brushless direct-current motors. *IEEE Transactions on Magnetics*, 34(5):3728–3736.

Dresner, T. and Barkan, P. (1989). A review of variable valve timing benefits and modes of operation. *SAE*, 891676.

dSPACE GmBH (2003). DS1103 PPC Controller Board Features Release 4.0.

Euler, L. (1989 (orig. date 1779)). De serie lambertina plurismique eius insignibus proprietatibus. *Leonhardi Euleri Opera Omnia, Ser. 1 Opera Mathematica, Bd 6*.

Fairchild (2005). Fairchild Semiconductor Hight Speed - 10MBit/s Logic Gate Optocouplers. *http://www.fairchildsemiconductor.com/ds/HC/HCPL-2611.pdf*.

Feeley, J. J. (1996). A simple dynamic model for eddy currents in a magnetic actuator. *IEEE Transactions on Magnetics*, 32(2):453–458.

Flierl, R. and Klüting, M. (2000). The third generation of valvetrains - New fully variable valvetrains for throttle-free load control. *SAE*, 2000-01-1227.

Fliess, M., Lévine, J., Martin, P., and Rouchon, P. (1992). On differentially flat nonlinear systems. *Proceedings of the IFAC-Symposium NOLCOS 1992, Bordeaus, France*, pages 408–412.

Fliess, M., Lévine, J., Martin, P., and Rouchon, P. (1995). Flatness and defect of non-linear systems: Introductory theory and examples. *International Journal of Control*, 61(6):1327–1361.

Fliess, M., Lévine, J., Martin, P., and Rouchon, P. (1999). A Lie-Bäcklund approach to equivalence and flatness of nonlinear systems. *IEEE Transactions on Automatic Control*, 44(5):922–937.

Fukuo, K., Iwata, T., Sakamoto, Y., Imai, Y., Nakahara, K., and Lantz, K. A. (1997). Honda 3.0 Liter New V6 Engine. *SAE*, 970916.

Fulks, G. C. (1989). High speed solenoid control techniques. *Automotive Power Electronics*, pages 54–59.

Geringer, A., Geringer, R., and Geringer, D. (1991). Electromagnetic door lock device. *U.S. Patent 5,033,779.*

Giglio, V., Iorio, B., Police, G., and di Gaeta, A. (2002). Analysis of advantages and of problems of electromechanical valve actuators. *SAE*, 2002-01-1105.

Gill, P. E., Murray, W., and Wright, M. H. (1981). *Practical Optimization.* Academic Press, London.

Gottschalk, M. (1993). Electromagnetic valve actuator drives variable valvetrain. *Design News.*

Gramann, M., Nagel, M., Rockl, T., and Wilczek, R. (2000). Electromagnetic actuator. *US Pat. 6,037,851.*

Gray, C. (1988). A review of variable engine valve timing. *SAE*, 880386.

Grohn, M. and Wolf, K. (1989). Variable valve timing in the new Mercedes Benz four-valve engines. *SAE*, 891990.

Gunselmann, C. and Melbert, J. (2003). Improved robustness and energy consumption for sensorless electromagnetic valve train. *SAE*, 2003-01-0030.

Harmer, K., Jewell, G. W., and Howe, D. (2002). Transient performance of a short-stroke linear solenoid actuator. *IEE Proceedings of Electric Power Applications*, 149(5):379–384.

Hartwig, C., Josef, O., and Gebauer, K. (2004). Transients of electromagnetic valve train (EMVT) actuators. *SAE*, 2004-01-1388.

Haskara, I., Kokotovic, V. V., and Mianzo, L. A. (2004). Control of an electromechanical valve actuator for a camless engine. *International Journal of Robust and Nonlinear Control*, 14:561–579.

Heffel, J. W. (2003). Improving the power curve of an ICE using electromagnetic valve actuation. *SAE*, 2003-01-2276.

Hoffmann, W., Peterson, K., and Stefanopoulou, A. G. (2003). Iterative learning control for soft landing of electromechanical valve actuator in camless engines. *IEEE Transactions on Control Systems Technology*, 11(2):174–184.

Hughes, A., Stephenson, J. M., and Sloan, C. (1998). Dynamic modelling and control of a normal force actuator. *IEE Proceedings of Electric Power Applications*, 145(5):449–454.

Ilic'-Spong, M., Marino, R., Peresada, S. M., and Taylor, D. G. (1987). Feedback linearizing control of switched reluctance motors. *IEEE Transactions on Automatic Control*, 32(5):371–379.

Kajima, T. (1995). Dynamic model of the plunger type solenoids at deenergizing state. *IEEE Transactions on Magnetics*, 31(3):2315–2323.

Kajima, T. and Kawamura, Y. (1995). Development of a high-speed solenoid valve: Investigation of solenoids. *IEEE Transactions on Industrial Electronics*, 42(1):1–8.

Kallenbach, E., Feindt, K., and Herman, R. (1997). Design of electromagnetic actuators with fast dynamics. *SAE*, 97AE013.

Kalman, R. E. (1960). A new approach to linear filtering and prediction problems. *Transactions of the ASME–Journal of Basic Engineering*, 82(Series D):35–45.

Kassakian, J. G., Wolf, H.-C., Miller, J. M., and Hurton, C. J. (1996). Automotive Electrical Systems circa 2005. *IEEE Spectrum*, pages 22–27.

Koch, C., Lynch, A., and Chladny, R. (2002). Modeling and control of solenoid valves for internal combustion engines. *Proceedings of the 2nd IFAC Conference on Mechatronic Systems, Berkeley, CA*, pages 213–218.

Koch, C., Lynch, A., and Chung, S. (2004). Flatness-based automotive solenoid valve control. *Proceedings of the 6th IFAC Symposium on Nonlinear Control System, Stuttgart, Germany*, 3:1091–1096.

Konrad, R. (1998). Verfahren zur Bewegungssteuerung für einen ankers eines elektromagnetishen Aktuators. *German Pat. Appl. 19834548 A1*.

Kontarakis, G., Collings, N., and Ma, T. (2000). Demonstration of HCCI using a single cylinder four-stroke SI engine with modified valve timing. *SAE*, 2000-01-2870.

Kreuter, P., Heuser, P., and Schebitz, M. (1992). Strategies to improve SI-engine performance by means of variable intake lift, timing and duration. *SAE*, 920449.

Kriezis, E. E., Tsiboukis, T. D., Panas, S. M., and Tegopoulos, J. A. (1992). Eddy currents: Theory and applications. *Proceedings of the IEEE*, 80(10):1559–1589.

Lambert, J. H. (1758). Observationses variae in mathesin puram. *Acta Helvetica, physicomathematico-anatomico-botanico-medica, Basel*, 3:128–168.

Lequesne, B. (1990). Dynamic model of solenoids under impact excitation, including motion and eddy currents. *IEEE Transactions on Magnetics*, 26(2):1107–1116.

Lévine, J., Lottin, J., and Ponsart, J.-C. (1996). A nonlinear approach to the control of magnetic bearings. *IEEE Transactions on Control Systems Technology*, 4(5):524–544.

Lim, K. W., Cheung, N. C., and Rahman, M. F. (1994). Proportional control of a solenoid actuator. *Proceedings of the 20th International Conference of Industrial Electronics, Control and Instrumentation (IECON)*, 3:2045–2050.

Ljung, L. (1987). *System Identification: Theory for the User*. Prentice-Hall, Englewood Cliffs, NJ.

Ljung, L. (2004). *System Identification Toolbox for use with Matlab: User's Guide Version 6*. MathWorks, Inc., Natick, Mass.

Löewis, J. (2002). *Flachheitsbasierte Trajektorienfolgeregelung elektromechanischer Systeme*. PhD thesis, TU-Dresden.

Löewis, J. and Rudolph, J. (2003). Real-time trajectory generation for flat systems with constraints. In Zinober, A. and Owens, D., editors, *Nonlinear and Adaptive Control*, pages 385–394. New York, NY.

Ma, T. H. (1988). Effect of variable engine valve timing on fuel economy. *SAE*, 880390.

Maekawa, K., Ohsawa, N., and Akasaka, A. (1989). Development of a valve timing control system. *SAE*, 890680.

Martin, P. (1992). *À l'étude des systèmes diffèrentielement plats.* PhD thesis, École des Mines de Paris.

Martin, P., Murray, R. M., and Rouchon, P. (1997). Flat Systems. In Bastin, G. and Gevers, M., editors, *Plenary Lectures and Minicourses, Proceedings of the European Control Conference 1997*, pages 211–264. Brussels.

Maybeck, P. S. (1979). *Stochastic Models, Estimation and Control, Volume 1.* Academic Press, New York, N. Y.

Mercorelli, P., Lehmann, K., and Liu, S. (2003). Robust flatness based control of a electromagnetic linear actuator using adaptive PID controller. *Proceedings of the 42nd IEEE Conference on Decision and Control*, 4(4):3790–3795.

Milam, M. B. (2003). *Real-Time Optimal Trajectory Generation for Constrained Dynamical Systems.* PhD thesis, University of Alberta.

Mooney, W. J. (1981). *Optoelectronic Devices and Principles.* Prentice-Hall, Englewood Cliff, New Jersey.

Moriya, Y., Watanabe, A., Uda, H., Kawamura, H., Yoshioka, M., and Adachi, M. (1996). A newly developed intelligent variable valve timing system - Continuously controlled cam phasing as applied to a new 3-Liter In-Line-6 engine. *SAE*, 960579.

Nieuwstadt, M. V., Rathinam, M., and Murray, R. M. (1994). Differential flatness and absolute equivalence. *Proceedings of the 33rd Conference on Decision and Control, Lake Buena Vista, FL*, pages 326–333.

Nonaka, K. and Baillieul, J. (2001). Open loop robust vibrational stabilization of a two wire system inside the snap-through instability region. *Proceedings of the 40th IEEE Conference on Decision and Control, Orlando, Florida*, 2:1334–1341.

Pawlak, A. M. and Nehl, T. W. (1988). Transient finite element modeling of solenoid actuators: The coupled power electronics, mechanical and magnetic field problem. *IEEE Transaction on Magnetics*, 24(1):270–273.

Payne, D. (1899). Electrically controlled valve gear for gas or other motors. *U.S. Patent 623821.*

Peterson, K., Stefanopoulou, A., Megli, T., and Haghgooie, M. (2002). Output observer based feedback for soft landing of electromechanical camless valvetrain actuator. *Proceedings of American Control Conference, Anchorage, AK*, pages 1413–1418.

Peterson, K. S. and Stefanopoulou, A. G. (2004). Extremum seeking control for soft landing of an electromechanical valve actuator. *To appear in Automatica.*

Peterson, K. S., Stefanopoulou, A. G., Wang, Y., and Haghgooie, M. (2004). Nonlinear self-tuning control for soft landing of an electromechanical valve actuator. *Proceedings of IFAC Mechatronic Conference.*

Piron, M., Sangha, P., Reid, G., Miller, T. J. E., Ionel, D., and Coles, J. R. (1999). Rapid computer-aided design methods for fast-acting solenoid actuators. *IEEE Transactions on Industrial Applications*, 35(5):991–999.

Pischinger, F. and Kreuter, P. (1984). Electromagnetically operating actuator. *US Pat. 4,455,543.*

Rao, V. S. (1964). Equivalent circuit of solid iron core for impact excitation problems. *IEE Proceedings*, 111(2):349–357.

Roters, H. (1941). *Electromagnetic Devices.* John Wiley and Sons, New York.

Schechter, M. M. and Levin, M. B. (1996). Camless engine. *SAE*, 960581.

Schmitz, N. L. and Novotny, D. W. (1965). *Introductory Electromechanics.* The Ronald Press Company, New York.

Sellnau, M. and Rask, E. (2003). Two-step variable valve actuation for fuel economy, emissions and performance. *SAE*, 2003-01-002.

Smith, D. S., Jenkins, M. K., and Howe, D. (1994). The transient time domain analysis of non-linear electro-mechanical systems. *IEEE Transactions on Magnetics*, 30(5):3260–3263.

Stubbs, A. (2000). Modeling and controller design of an electromagnetic engine valve. Master's thesis, University of Illinois.

Tai, C., Stubbs, A., and Tsao, T.-C. (2001). Modeling and controller design of an electromagnetic engine valve. *Proceedings of the American Control Conference, Arlington, VA*, pages 2890–2895.

Tai, C. and Tsao, T.-C. (2002). Control of an electromechanical camless valve actuator. *Proceedings of the American Control Conference, Anchorage, AK*, pages 262–267.

Tai, C. and Tsao, T.-C. (2003). Control of an electromechanical actuator for camless engines. *Proceedings of the American Control Conference, Denver, Colorado*, pages 3113–3118.

Theobold, M. A., Lequesne, B., and Henry, R. (1994). Control of engine load via electromagnetic valve actuators. *SAE*, 940816.

Torrey, D. A. and Lang, J. H. (1994). Modelling a nonlinear variable-reluctance motor drives. *IEE Proceedings B - Electric Power Applications*, 137(5):314–326.

van Nieuwstadt, M. J. and Murray, R. M. (1995). Approximate trajectory generation for differentially flat systems with zero dynamics. *Proceedings of the 34th Conference on Decision and Control, New Orleans, LA*, pages 4224–4230.

Venkataramu, B. K., Nagarajan, T., Ram, K. A., Ravishankar, S., and Prasad, C. S. (1988). Evaluation and analysis of fast acting solenoid. *Current Science*, 57(15):815–820.

Wang, Y. (2001). Camless engine valvetrain: Enabling technology and control techniques. Master's thesis, University of California.

Wang, Y., Megli, T., Haghgooie, M., Peterson, K. S., and Stefanopoulou, A. G. (2002). Modeling and control of electromechanical valve actuator. *SAE*, 2002-01-1106.

Wang, Y., Stefanopoulou, A., Haghgooie, M., Kolmanovsky, I., and Hammoud, M. (2000). Modeling of an electromechanical valve actuator for a camless engine. *Proceedings of the 5th International Symposium on Advanced Vehicle Control*, 93.

Warnecke, V., Kramer, W., and Koch, A. (1999). The electrical and mechanical property of the electromechanical valve train system components. Aachem Colloquium.

Woittennek, F. (1999). Untersuching flachheitsbasierter nichtlinearer Regler für magnetgelagerte Wellen. Master's thesis, TU-Dresden, Germany.

APPENDIX A

FILTER ALGORITHMS FOR REAL-TIME APPLICATIONS

A.1 Constant Gain Extended Kalman Filter

The Kalman filter [Kalman, 1960] is simply an "optimal recursive data processing algorithm" tailored for real-time applications where unmeasured system state variables can be approximated accurately from all available data. Regardless of corrupted data as a result of noise, biases, device inaccuracies and other uncertain factors, the filter process all observed measurements along with prior system knowledge to generate desired state estimates while statistically minimizing errors [Maybeck, 1979]. Consider a nonlinear system defined in [Chui and Chen, 1991] as

$$x_{k+1} = f_k(x_k) + H_k(x_k)\xi_k \tag{A.1a}$$

$$v_k = g_k(x_k) + \eta_k \tag{A.1b}$$

where f_k and g_k are vector-valued functions with ranges in $\mathbb{R}^n$ and $\mathbb{R}^q$, respectively, $1 \leq q \leq n$, and H_k a matrix-valued function with range in $\mathbb{R}^n \times \mathbb{R}^q$, such that for each k the first order partial derivatives of $f_k(x_k)$ and $g_k(x_k)$ with respect to all the components of x_k are continuous. Zero-mean Gaussian white noise sequences, ξ_k and η_k, with ranges in $\mathbb{R}^p$ and $\mathbb{R}^q$, respectively, $1 \leq p, q \leq n$ are considered.

It is shown in [Chui and Chen, 1991] that Equation(A.1) can be approximated by

a linear model (Equation (A.2)) through a real-time linearization process.

$$x_{k+1} = A_k x_k + u_k + \Gamma_k \xi_k \tag{A.2a}$$

$$w_k = C_k x_k + \eta_k \tag{A.2b}$$

where A_k, C_k, w_k and Γ_k are determined in real-time and x_k is the state sequence. Since ξ_k and η_k are random sequence vectors, they are assumed Gaussian white noise with a mean value of zero. In effect, the expected values are $E(\xi_k) = 0$ and $E(\eta_k) = 0$ whereas the covariances are $Cov(\xi_k, \xi_j) = Q_{kj}$ and $Cov(\eta_k, \eta_j) = R_{kj}$ with Q_{kj} and R_{kj} being symmetric and positive definite. Based on the above state-space description, it is sufficient to derive an optimal estimate $\hat{x}_k$ of x_k. To compute $\hat{x}_k$ in real time, the recursive formula in [Chui and Chen, 1991] is derived as

$$\hat{x}_{k|k} = \hat{x}_{k|k-1} + G_k \left[v_k - g_k \hat{x}_{k|k-1} \right] \tag{A.3a}$$

$$\hat{x}_{k|k-1} = A_{k-1} \hat{x}_{k-1|k-1} \tag{A.3b}$$

where $\hat{x}_k = \hat{x}_{k|k}$ is from the prediction $\hat{x}_{k|k-1}$, $\hat{x}_{k|k-1}$ is from the estimate of $\hat{x}_{k-1} = \hat{x}_{k-1|k-1}$ and G_k is the Kalman gain matrix. An initial estimate $\hat{x}_0 = \hat{x}_{0|0}$ is required as a starting point for the algorithm. This is an unbiased estimate of the initial state, x_0, and therefore, it is valid to assume $\hat{x}_{0|0} = E(x_0)$. As for the gain matrix, G_k, it is recursively calculated with

$$G_k = P_{k,\,k-1} \left[\frac{\partial g_k}{\partial x_k} (\hat{x}_{x|k-1}) \right]^T \left[\left[\frac{\partial g_k}{\partial x_k} (\hat{x}_{k|k-1}) \right] P_{k,\,k-1} \left[\frac{\partial g_k}{\partial x_k} (\hat{x}_{k|k-1}) \right]^T + R_k \right]^{-1} \tag{A.4}$$

where

$$P_{k,\,k-1} = \left[\frac{\partial f_{k-1}}{\partial x_{k-1}}(\hat{x}_{k-1})\right] P_{k-1|k-1} \left[\frac{\partial f_{k-1}}{\partial x_{k-1}}(\hat{x}_{k-1})\right]^T + H_{k-1}(\hat{x}_{k-1}) Q_{k-1} H_{k-1}^T(\hat{x}_{k-1}) \tag{A.5}$$

Combining the above results, an optimal estimate of $\hat{x}_k$ of the state x_k from v_k can be obtained as follows

$$P_{0|0} = Var(x_0)$$

$$P_{k,\,k-1} = \left[\frac{\partial f_{k-1}}{\partial x_{k-1}}(\hat{x}_{k-1})\right] P_{k-1|k-1} \left[\frac{\partial f_{k-1}}{\partial x_{k-1}}(\hat{x}_{k-1})\right]^T + H_{k-1}(\hat{x}_{k-1}) Q_{k-1} H_{k-1}^T(\hat{x}_{k-1})$$

$$G_k = P_{k,\,k-1} \left[\frac{\partial g_k}{\partial x_k}(\hat{x}_{x|k-1})\right]^T \left[\left[\frac{\partial g_k}{\partial x_k}(\hat{x}_{k|k-1})\right] P_{k,\,k-1} \left[\frac{\partial g_k}{\partial x_k}(\hat{x}_{k|k-1})\right]^T + R_k\right]^{-1}$$

$$P_{k,\,k} = \left[I - G_k \left[\frac{\partial g_k}{\partial x_k}(\hat{x}_{k|k-1})\right]\right] P_{k,\,k-1}$$

$$\hat{x}_0 = E(x_0)$$

$$\hat{x}_{k|k-1} = f_{k-1}(\hat{x}_{k-1})$$

$$\hat{x}_{k|k} = \hat{x}_{k|k-1} + G_k(v_k - g_k(\hat{x}_{k|k-1}))$$

$$k = 1,\ 2, \ldots$$

This algorithm may be realized as shown in Figure A.1.

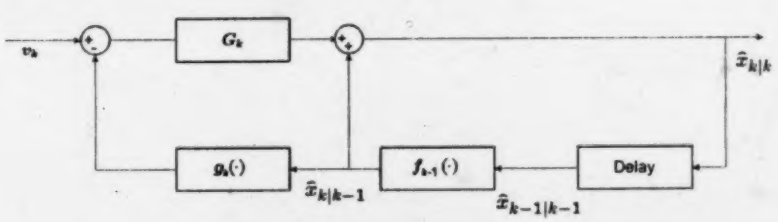

Figure A.1: Block diagram of Kalman filter algorithm

In real-time applications, however, [Chui and Chen, 1991] remarked that it is sometimes necessary to perform Kalman filtering with a nonrecursive gain matrix instead of G_k to save computationally time. Hence, the limiting (or steady state) Kalman filter is defined by replacing G_k with its limit G as $k \to \infty$, where G is a constant gain matrix. Note that the system is time-invariant, simplifying the algorithm to

$$\vec{x}_{k|k} = \vec{x}_{k|k-1} + G(v_k - g(\vec{x}_{k|k-1})) \tag{A.6a}$$

$$\vec{x}_{k|k-1} = f(\vec{x}_{k-1}) \tag{A.6b}$$

$$\vec{x}_{0|0} = E(x_0) \tag{A.6c}$$

Utilizing G does not deteriorate actual optimal estimations of $\hat{x}_k$ and, in fact, it is shown that the sequence, G_k, exponentially converges to its limit (see details in [Chui and Chen, 1991]). Equation (A.6) is easily implemented experimentally to estimate armature velocity using position data measurements.

A.2 Exponentially Weighted Moving Average Filter

The exponentially weighted moving averaged filter is a noise reduction algorithm commonly used in the industry. It places more emphasis to more recent data by discounting preceding data in an exponential manner. Such a filter can be designed with the starting point where the mean is expressed as:

$$\bar{a}_k = \frac{1}{n_i} \sum_{i=k-n+1}^{k} a_i \tag{A.7}$$

Expanding Equation (A.7) to include one additional point gives

$$\bar{a}_{k+1} = \frac{1}{n+1} \sum_{i=k-n+1}^{k+1} a_i = \frac{1}{n+1} \left[a_{k+1} + \sum_{i=k-n+1}^{k} a_i \right] \tag{A.8}$$

Since $\sum_{i=k-n+1}^{k} a_i = n\bar{a}_k$, Equation (A.8) is redefined as,

$$\bar{a}_{k+1} = \frac{1}{n+1} [a_{k+1} + na_k] = \left[\frac{1}{n+1} \right] a_{k+1} + \left[\frac{n}{n+1} \right] \bar{a}_k \tag{A.9}$$

By shifting the time index back one time-step, the corresponding expression for $\bar{a}_k$ is

$$\bar{a}_k = \left[\frac{1}{n+1} \right] a_k + \left[\frac{n}{n+1} \right] \bar{a}_{k-1} \tag{A.10}$$

Letting $\alpha = \frac{n}{n+1}$, the filter can be written as:

$$\bar{a}_k = \alpha\, \bar{a}_{k-1} + [1-\alpha] a_k \tag{A.11}$$

Modifying Equation (A.11), armature acceleration in real time can be approximated

$$\bar{a}_k = \alpha \bar{a}_{k-1} + [1-\alpha] \frac{v_k - v_{k-1}}{dt}$$

where $dt = 20\ \mu$s and v_k is the armature velocity predicted by the kalman filter. Note that the filter constant, α, dictates the degree of filtering. Since $n \geq 0$, this means that $0 \leq \alpha \leq 1$. In the experiment, a filter constant, $\alpha = 0.8$, is used.

Appendix B

Experimental Equipment Schematics

The following provides electronic schematics for the equipment used during the course of the experiments.

B.1 Overcurrent Protection Circuit

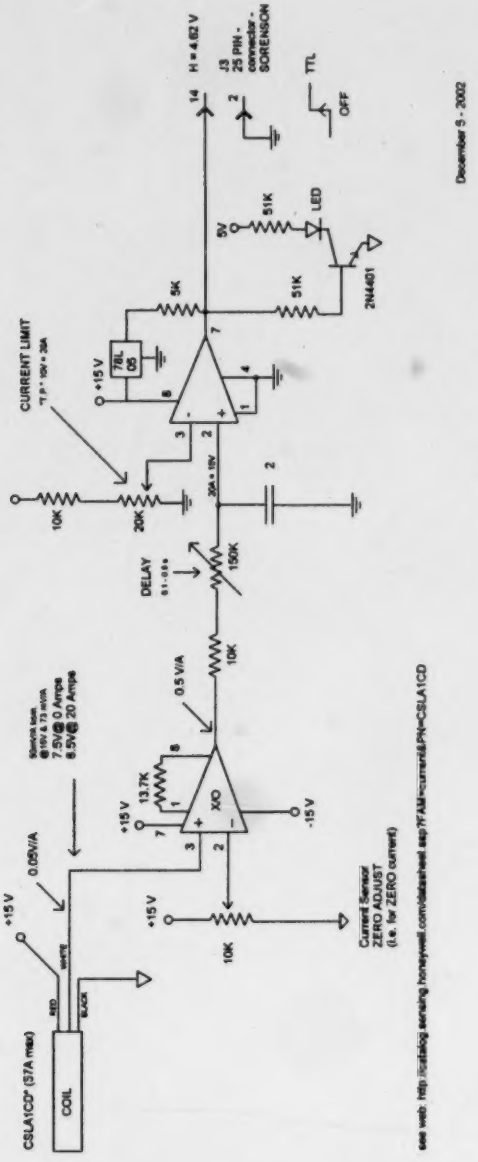

Figure B.1: Overcurrent protection circuit schematics

B.2 Opto-Isolator

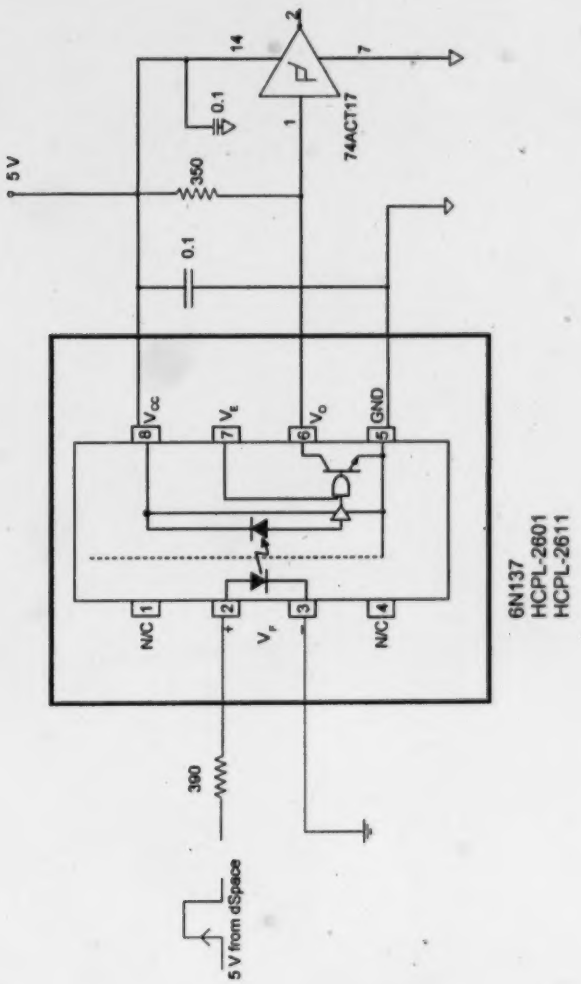

Figure B.2: Opto-isolator circuit schematics

B.3 Power Electronics Current-Voltage Sensing

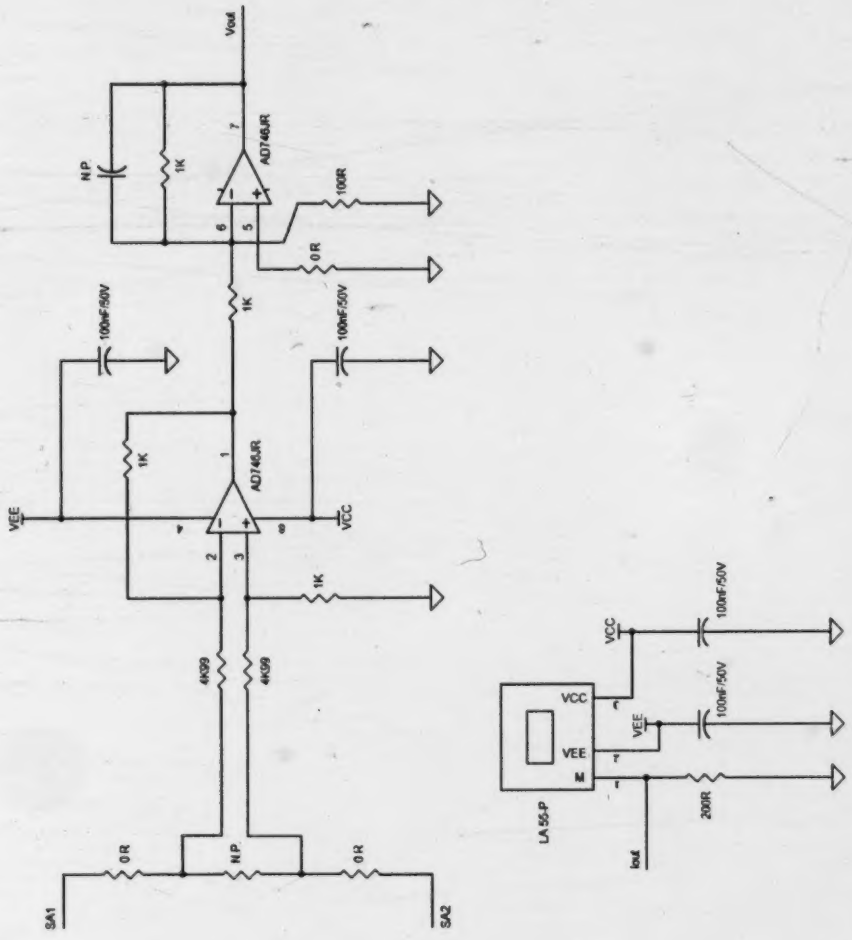

Figure B.3: Onboard power electronics current-voltage sensing

B.4 LEM LA55-P Current Transducer Specifications

Current Transducer LA 55-P

I_{PN} = 50 A

For the electronic measurement of currents : DC, AC, pulsed..., with a galvanic isolation between the primary circuit (high power) and the secondary circuit (electronic circuit).

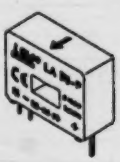

Electrical data

I_{PN}	Primary nominal r.m.s. current			50			A
I_P	Primary current, measuring range			0 .. ± 70			A
R_M	Measuring resistance @		T_A = 70°C		T_A = 85°C		
			$R_{M\,min}$	$R_{M\,max}$	$R_{M\,min}$	$R_{M\,max}$	
	with ± 12 V	@ ± 50 A_{max}	10	100	60	95	Ω
		@ ± 70 A_{max}	10	50	60[1]	60[1]	Ω
	with ± 15 V	@ ± 50 A_{max}	50	160	135	155	Ω
		@ ± 70 A_{max}	50	90	135[2]	135[2]	Ω
I_{SN}	Secondary nominal r.m.s. current			50			mA
K_N	Conversion ratio			1 : 1000			
V_C	Supply voltage (± 5 %)			± 12 .. 15			V
I_C	Current consumption			10 (@ ±15 V) + I_S			mA
V_d	R.m.s. voltage for AC isolation test, 50 Hz, 1 mn			2.5			kV

Accuracy - Dynamic performance data

X	Accuracy @ I_{PN}, T_A = 25°C	@ ± 15 V (± 5 %)		± 0.65	%
		@ ± 12 .. 15 V (± 5 %)		± 0.90	%
ε_L	Linearity			< 0.15	%
			Typ	Max	
I_O	Offset current @ I_P = 0, T_A = 25°C			± 0.2	mA
I_{OM}	Residual current[3] @ I_P = 0, after an overload of 3 x I_{PN}			± 0.3	mA
I_{OT}	Thermal drift of I_O	0°C .. + 70°C	± 0.1	± 0.5	mA
		- 25°C .. + 85°C	± 0.1	± 0.8	mA
t_{ra}	Reaction time @ 10 % of I_{PN}			< 500	ns
t_r	Response time @ 90 % of I_{PN}			< 1	µs
di/dt	di/dt accurately followed			> 200	A/µs
f	Frequency bandwidth (- 1 dB)			DC .. 200	kHz

General data

T_A	Ambient operating temperature		- 25 .. + 85	°C
T_S	Ambient storage temperature		- 40 .. + 90	°C
R_S	Secondary coil resistance @	T_A = 70°C	80	Ω
		T_A = 85°C	85	Ω
m	Mass		18	g
	Standards [4]		EN 50178(97.10.01)	

Notes : [1] Measuring range limited to ± 60 A_{max}
[2] Measuring range limited to ± 55 A_{max}
[3] Result of the coercive field of the magnetic circuit
[4] A list of corresponding tests is available

Features

- Closed loop (compensated) current transducer using the Hall effect
- Printed circuit board mounting
- Insulated plastic case recognized according to UL 94-V0.

Advantages

- Excellent accuracy
- Very good linearity
- Low temperature drift
- Optimized response time
- Wide frequency bandwidth
- No insertion losses
- High immunity to external interference
- Current overload capability.

Applications

- AC variable speed drives and servo motor drives
- Static converters for DC motor drives
- Battery supplied applications
- Uninterruptible Power Supplies (UPS)
- Switched Mode Power Supplies (SMPS)
- Power supplies for welding applications.

030709/9

APPENDIX C

SOFTWARE STRUCTURE

This section details the software structure coded in C language for actuator control. A brief description of the structure and individual software modules is provided.

C.1 Program Development Structure Objectives

The main requirements of the software design are listed below:

1. **Modularity for control algorithms, sensors and actuator allowing simple replacement of individual software modules:** The software should provide a framework in which different control strategies can be tested easily.

2. **Calibration of control parameters and dynamic viewing:** The experimental setup consist of a dSPACE system interfaced to an actuator testbed and a development PC. Real-time system changes can be made on the development PC by changing global variables on virtual calibrating instruments.

3. **Multi-platform usage of the program:** The software should provide separate platforms for debugging purposes and real-time executions. Debugging of inputs and outputs are read and written offline to a file. In real-time, the system is coupled to virtual calibration instruments.

C.2 Program Structure

Figure C.1 illustrate the structure of main program modules, and how offline debugging and real-time platforms are realized from individual modules. Each platform must be selected before the program is compiled since the platforms are implemented with pre-compiler switches. A brief description of each modules are given in Section C.3.

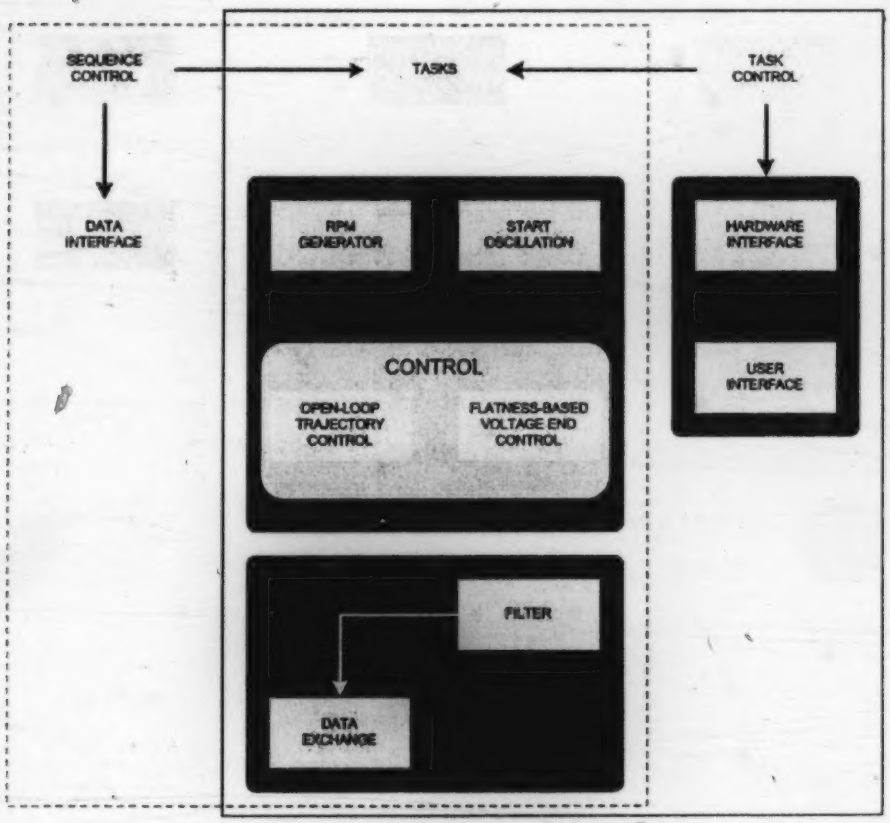

Figure C.1: Multi-platform program structure (dotted line → debugging file I/O platform and solid line → real-time platform)

C.3 Modules Description

C.3.1 Tasks

The tasks module provides a linkage for various program modules to be executed together. It interface core modules of the program (i.e. Swing Oscillator, RPM Generator, Control and etc.) with modules defined for either real-time or debugging modes. This module performs three main tasks which are defined below (in priority order):

1. A 20 μs task in which the control is called.
2. A 100 μs task in which the RPM generator and the Swing Oscillator is called.
3. A low priority task for miscellaneous tasking such as parameter calibration.

C.3.2 RPM Generator

The RPM Generator module generates a signal that simulates an actual engine RPM. This logical signal is user specified and triggers the start of the valve opening or closing sequence. The RPM generator must be executed every 100 μs simply because it functions as a counter without any knowledge of real-time.

C.3.3 Start Oscillation

The Start Oscillation module implements a feedforward control to bring the armature from the center position to the closed position. This module can be executed every 100 μs for the same reasons stated above in Section C.3.2.

C.3.4 Control

The control module uses a state machine to call specific control tasks. During opening and closing, the respective coil currents are controlled to the armature's flight.

Flatness-based voltage end-control is only enabled when the armature's transition is in the closing state.

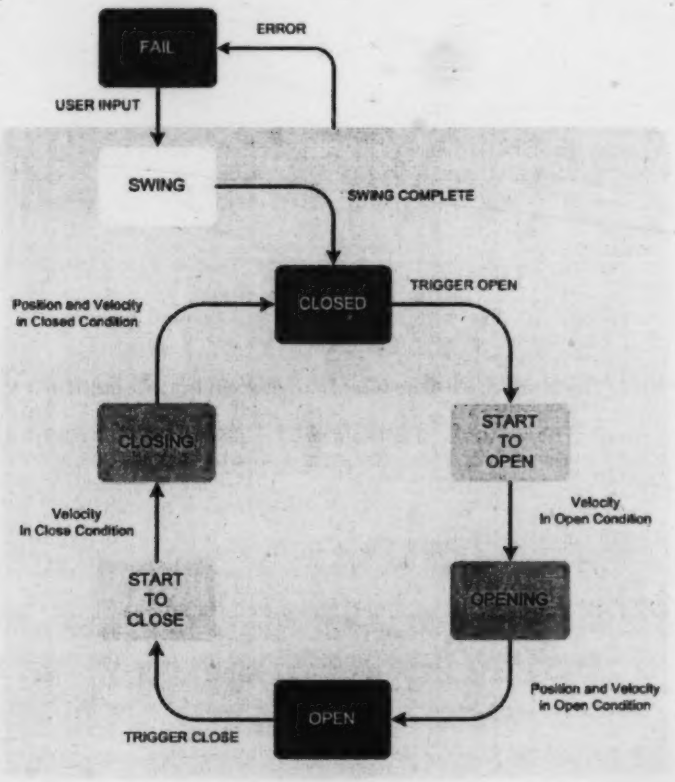

Figure C.2: Control state machine

A complete control process is best illustrated using a state diagram shown in Figure C.2. The system begins in the FAIL state, however in offline simulation mode, the system could easily be started elsewhere. The transition from FAIL to SWING is initiated by the user using an interface program on the desktop PC. When the SWING procedure is complete and successful in closing the valve , the state is automatically set to CLOSED and from this point onwards, normal operation commences. The next appropriate signal from the RPM generator triggers the transition from CLOSED to

START-TO-OPEN. As soon as a certain armature velocity is reached, the system switches to the OPENING state. During motion, a position based open-loop control is implemented. When the armature's landing position and velocity approaches a certain tolerance, the state changes to OPEN. The reverse process from OPEN to CLOSED functions similarly.

C.3.5 Flatness-Based Voltage End-Control

Flatness-based voltage end-control is intended for low armature landings on the closer coil. This control algorithm is switched on during the CLOSING state and supersedes an open-loop current control scheme that delivers the armature to within desirable flight conditions. The user has the option of disabling this controller if it is not required for use.

C.3.6 Open-loop Trajectory Control

Open-loop current control is implemented during the OPENING and CLOSING states. A PI current end-control algorithm is also included as an alternative for the flatness-based end-control scheme.

C.3.7 Filter

This module implements a constant gain extended Kalman filter for armature velocity estimations and an exponentially moving average filter for armature acceleration estimations.

C.3.8 Data Exchange

The Data Exchange module defines global variables that are required in other modules for monitoring or debugging.

C.3.9 Task Control

The Task Control module is only required for real-time execution where the control, filter, RPM generator and hardware interface modules are called, the interrupt service routines are installed in an infinite loop and non-time critical calculations are executed as a background task.

C.3.10 Hardware Interface

The primary function of the hardware interface consist of reading and generating signals over digital I/O, A/D and D/A channels. Additional service routines include PowerPC CPU temperature monitoring and emergency shutoff. This module is only linked for real-time testbed operation.

C.3.11 User Interface

The user interface is a separate stand alone program supplied by dSPACE which runs on the host PC and communicates with the real-time processor. The global variables in the real-time code can be addressed and thus monitored or changed.

C.3.12 Sequence Control

The Sequence Control module is an offline analog of the real-time task control module

C.3.13 Data Interface

The Data Interface is used for non-realtime debugging purposes and consists of two structured files in which input and output are defined. This mode is designed to allow offline debugging of the code.